Chaotic Behaviour of Charged Particles in Electromagnetic Fields

Chinenye Jane ANI (anxchi002@myuct.ac.za)

Supervised by: Associate Professor Haris Skokos

November 2018

Submitted in fulfillment of a master's degree by dissertation in the Department of Mathematics and Applied Mathematics at the University of Cape Town, South Africa

Abstract

In order to understand the motion of charged particles we numerically investigate the chaoticity of magnetic field lines of tokamak fields, as charged particles move along field lines. In particular, the symmetric tokamap was studied to determine the physical quantities that influence the system's chaotic behaviour. We implement several chaos detection techniques: the construction of Poincaré maps, the computation of the maximum Lyapunouv characteristic exponent (mLCE), as well as the Smaller Alignment Index (SALI). The analyses performed showed that the mLCE and SALI methods accurately quantified magnetic field lines' chaotic behaviour and that the relative perturbation strength influences the system's chaoticity. In addition, we illustrate the diffusive properties of magnetic field lines, using statistical measures like the mean square displacement (MSD) and calculating diffusion coefficients. Lastly, we present the construction of explicit near-symplectic mappings of the symmetric tokamap with Lie-generating functions.

Plagiarism Declaration

I know the meaning of plagiarism and declare that all of the work in the dissertation, save for that which is properly acknowledged, is my own.

Signed by candidate

Chinenye Jane Ani

Contents

1. Introduction

The demand for safe, clean energy is one of the greatest challenges the ever-growing human population is facing. The dependence on depleting fossil fuels for energy which are hazardous to man and his environment is a major concern and if not addressed could lead to world energy crisis. As a consequence, the search for a solution to this problem has led to the use of renewable energy sources such as solar, wind and biomass as alternative sources of safe, clean energy supply (Ongena and Oost, 2012; MacKay, 2008). Unfortunately, this eco-friendly energy cannot meet the ever-growing energy demands of the world, as it is not always available for use. Since the availability of these renewable energy sources is beyond man's control, what could help tackle this problem? Nuclear fusion!

Nuclear fusion utilizes the surplus energy released from the fusion of two light nuclei into a heavy nucleus. The goal of nuclear fusion is to harness the process used by the sun to generate its energy, i.e., the fusion of hydrogen nuclei into helium in its core. On earth, the easiest nuclear fusion involving the lowest energy is the fusion of two hydrogen isotopes deuterium and tritium known as the **D-T** reaction (Wesson, 2004)

$$D + T \quad \rightarrow \quad H_e^4(3.5MeV) + 14.1MeV.$$

Deuterium is easily obtained as it occurs naturally in sea water while tritium, an unstable, radioactive isotope of hydrogen with a half-life of 12 years is obtained from the bombardment of lithium isotopes with neutrons. The fusion of these isotopes involves colliding ions under high temperature, for the attractive, short range nuclear force to overcome the repulsive, long range Coulomb force in plasma[1].

In order to ignite and keep a **D-T** plasma burning the following so-called Lawson criterion introduced by Lawson (1957) must be satisfied:

$$nT\tau_E > 3 \times 10^{21} keVs/m^3,$$

where n is the ion density, T the ion temperature and τ_E the energy confinement time. This simply means that the laboratory heating of plasma requires the following: a very high temperature to initiate high-energy collision; sufficient plasma particle density to increase the likelihood of collision occurrence; and sufficient confinement time to hold the plasma. As a result, heating and confining plasma at a sufficiently high temperature over a sufficient long time has been the focus of fusion research for the past 60 years. Scientists are faced with engineering and scientific challenges of constructing a device that satisfies the Lawson criterion. Consequently, the *magnetic confinement fusion* (MCF) concept based on the confinement of plasma by strong magnetic fields and the *inertial confinement fusion* (ICF) where multiple lasers or particle beams are used to obtain plasma by symmetrically irradiating a fuel-containing target were introduced. However, the MCF concept is the more widely used, with stellarators and tokamaks as types of MCF devices (see Figure 1.1). The most popular MCF device is the tokamak an abbreviation of the Russian phrase 'TOrodal naya KAmera MAgnitnoi Katushki' which means 'Toroidal Chamber with Magnetic Coils.' Since nuclear fusion has been identified to provide a boundless supply of safe, clean energy many countries have collaborated in fusion research which has led to the development of the Joint European Torus (JET), the largest tokamak and the only operational fusion device capable of producing fusion energy. Moreover, another significant achievement is the agreement of 35 countries to build the International Thermonuclear Experimental Reactor (ITER) tokamak in Southern France. ITER will be the first fusion device to produce net energy and maintain fusion for a long time. It is

[1] Plasma is an ionized state of matter similar to gas having almost an equal number of positively charged ions and negatively charged electrons that exhibit a collective behaviour. Fusion plasmas provide the environment in which light nuclei can fuse and produce energy.

designed to produce 10 times the energy produced by JET and will bridge the gap between today's experimental fusion devices and future power plants.

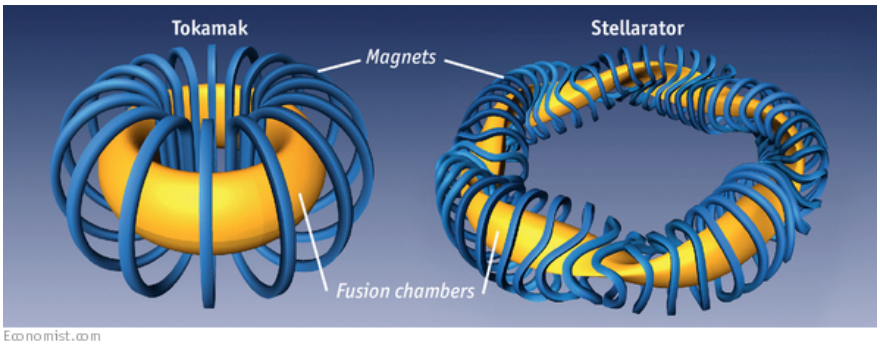

Figure 1.1: Tokamak and stellarator (Image taken from The Economist).

Despite these significant developments, the goal of economic nuclear fusion power is still not within reach as many years of research have revealed sophisticated means by which a burning plasma will attempt to avoid confinement. One of such means is chaos. Chaos is simply the sensitive dependence of a dynamical system on initial conditions, also refered sometimes as disorder or turbulence. Chaos impedes plasma confinement as it increases particle and energy transport in tokamak fields, as well as magnetic field lines transport. Research has shown that chaos is quite a common feature in space and laboratory plasmas and an understanding of the onset of chaos is crucial in determining the collective plasma particle motion. Although much progress has been made in understanding the onset of chaos in plasma, the fully developed chaotic plasma state is still an unsolved problem.

Over the years, in attempting to have a better systematic understanding of plasma turbulence researchers have separated the self consistent description of chaotic plasma processes into distinct steps. One characterises the statistics of the chaotic electromagnetic fields and the other considers the particle motion in these fields. In this study, we concentrate on the former, by using chaotic dynamics to analyse the behaviour of chaotic electromagnetic fields. Our major concern is on a realistic model of tokamak fields, the so-called *symmetric tokamap*. We attempt to investigate the chaotic behaviour of the symmetric tokamap by qualitatively analysing its phase space dynamics, quantifying the chaotic fraction of the system's phase space, and determining the physical quantities that control the chaoticity of the system. Moreover, we analyse the diffussive properties of this system's magnetic field lines using statistical measures to calculate diffusion coefficients. Finally, an explicit near-symplectic map of the system is constructed and its dynamics is studied. All numerical computations are carried out using Fortran programming language, while for the explicit near-symplectic map computations are done in Octave programming language.

The thesis is organised as follows: in Chapter 2 the chaotic dynamics of toy models, namely, the Henon-Heiles system, the 2D standard map and the Froeschlé's 4D symplectic map are presented; in Chapter 3 the magnetic field representation, the magnetic surface destruction, the chaotic dynamics of the symmetric tokamap and its diffusive properties are studied in detail; in Chapter 4 the construction of explicit near-symplectic mappings of the symmetric tokamap with Lie-generating functions is described; finally, the main conclusions of our work are summarised in Chapter 5.

2. Chaos

Since our main goal is to study the chaotic dynamics of tokamak fields, it is imperative to provide a detailed discussion about chaos. First, we will adopt the definition given by Devaney (1989).

2.0.1 Definition. Let S be a metric space and $\mathbf{f} : V \longrightarrow V$ a continuous map on this set. We say that $\mathbf{f}$ is *chaotic* on S if

1. $\mathbf{f}$ has a sensitive dependence on initial conditions,
2. $\mathbf{f}$ is topologically transitive,
3. periodic points are dense in S.

We proceed by giving a detailed explanation of Definition 2.0.1.

2.0.2 Definition. $\mathbf{f} : V \longrightarrow V$ has a *sensitive dependence on initial conditions* if there exists $\delta > 0$ such that, for any $\mathbf{x} \in V$ and any neighbourhood Δ of $\mathbf{x}$, there exists $\mathbf{y} \in \Delta$ and $n \geq 0$ such that $|\mathbf{f}^n(\mathbf{x}) - \mathbf{f}^n(\mathbf{y})| > \delta$, where $\mathbf{f}^n$ denotes n successive applications of $\mathbf{f}$.

Realistically, this definition suggests the existence of at least a point arbitrarily close to $\mathbf{x}$ that becomes δ distance away from $\mathbf{x}$ under iterations of $\mathbf{f}$.

2.0.3 Definition. $\mathbf{f} : V \longrightarrow V$ is said to be *topologically transitive* if for any pair of open sets $U, W \subset V$ there exists a non-negative integer n such that $\mathbf{f}^n(U) \cap W \neq \emptyset$.

This definition suggests the existence of points which finally move from one arbitrary small neighbourhood to another under iterations of $\mathbf{f}$. As a result, it is impossible to separate the dynamical system into disjoint invariant open sets. Finally, the third condition suggests the existence of some kind of regularity in $\mathbf{f}$ as it has many periodic orbits.

2.1 Equations of Motion and Variational Equations

Now, let us consider an N degree of freedom continuous, autonomous Hamiltonian system having a Hamiltonian function

$$H(\mathbf{q}, \mathbf{p}) = h = \text{constant}, \tag{2.1.1}$$

where $\mathbf{q} = (q_1, q_2, ..., q_N)$ and $\mathbf{p} = (p_1, p_2, ..., p_N)$. q_i and p_i, $i = 1, 2, ..., N$, are the generalised coordinates and conjugate momenta, respectively. An orbit in the $n = 2N-$dimensional phase space Z of the Hamiltonian system is defined as the vector

$$\mathbf{x}(t) = (\mathbf{q}(t), \mathbf{p}(t)),$$

where $x_i = q_i$, $x_{i+N} = p_i$, $i = 1, 2, ..., N$. The time evolution of this orbit is governed by

$$\dot{\mathbf{x}} = \mathbf{f}(\mathbf{x}) = \begin{bmatrix} \frac{\partial H}{\partial \mathbf{p}} & -\frac{\partial H}{\partial \mathbf{q}} \end{bmatrix}^T = \mathbf{J}_{2N} \cdot \mathbf{DH}, \tag{2.1.2}$$

which are called the Hamilton's equations of motion. We note that $(^T)$ denotes the transpose of a matrix.

The matrix $\mathbf{J}_{2N}$ is of the form

$$\mathbf{J}_{2N} = \begin{bmatrix} \mathbf{0}_N & \mathbf{I}_N \\ -\mathbf{I}_N & \mathbf{0}_N \end{bmatrix},$$

and

$$\mathbf{DH} = \begin{bmatrix} \frac{\partial H}{\partial q_1} & \frac{\partial H}{\partial q_2} & \cdots & \frac{\partial H}{\partial q_N} & \frac{\partial H}{\partial p_1} & \frac{\partial H}{\partial p_2} & \cdots & \frac{\partial H}{\partial p_N} \end{bmatrix}^T,$$

with $\mathbf{I}_N$ and $\mathbf{0}_N$ being the $N \times N$ identity matrix and zero matrix, respectively. Suppose we follow the evolution of the separation of two close initial conditions say $\mathbf{x}(0)$ and $\mathbf{x}(0) + \delta\mathbf{x}(0)$ to $\mathbf{x}(t)$ and $\mathbf{x}(t) + \delta\mathbf{x}(t)$. The vector $\mathbf{w}(t) = \delta\mathbf{x}(t)$ is the deviation vector from the reference orbit $\mathbf{x}(t)$ at time t. It follows that the time evolution of an initial deviation vector $\mathbf{w}(0) = (\delta\mathbf{q}(0), \delta\mathbf{p}(0))$ of the system (2.1.1) is governed by the variational equations given by

$$\dot{\mathbf{w}} = [\mathbf{J}_{2N} \cdot \mathbf{D}^2\mathbf{H}(\mathbf{x}(t))] \cdot \mathbf{w}, \tag{2.1.3}$$

where

$$\mathbf{D}^2\mathbf{H}(\mathbf{x}(t))_{i,j} = \left[\frac{\partial^2 H}{\partial x_i \partial x_j}\right]_{x(t)}, \quad i, j = 1, 2, ..., 2N. \tag{2.1.4}$$

Let us now consider a $2N$ dimensional symplectic map, which preserves the phase space volume and is of the form

$$\mathbf{x}_{n+1} = \mathbf{f}(\mathbf{x}_n). \tag{2.1.5}$$

The evolution of a deviation vector $\mathbf{w}_n$ at discrete time $t = n \in \mathbb{N}$ with respect to a reference orbit $\mathbf{x}_n$ is governed by the tangent map

$$\mathbf{w}_{n+1} = \mathbf{M}_n \cdot \mathbf{w}_n, \tag{2.1.6}$$

with

$$\mathbf{M} = \begin{bmatrix} \frac{\partial f_1}{\partial x_1} & \frac{\partial f_1}{\partial x_2} & \cdots & \frac{\partial f_1}{\partial x_{2N}} \\ \frac{\partial f_2}{\partial x_1} & \frac{\partial f_2}{\partial x_2} & \cdots & \frac{\partial f_2}{\partial x_{2N}} \\ \vdots & \vdots & & \vdots \\ \frac{\partial f_{2N}}{\partial x_1} & \frac{\partial f_{2N}}{\partial x_2} & \cdots & \frac{\partial f_{2N}}{\partial x_{2N}} \end{bmatrix}.$$

We can see from these formulations that the generalised coordinates and momenta appear explicitly in (2.1.3) and (2.1.6). This consequently leads to the simultaneous integration of the equations of motion and the variational equations for the evolution of a deviation vector in a continuous Hamiltonian system. In the same vein, for symplectic maps we simultaneously iterate the map (2.1.5) and the tangent map (2.1.6) for the evolution of a deviation vector.

2.2 Chaos Indicators

2.2.1 The Poincaré Map. Since the computation of Poincaré maps or Poincaré surfaces of sections (PSSs) was introduced by Henon and Heiles (1964), it has been widely used to analyse weakly perturbed Hamiltonian systems of two-degrees of freedom. A Poincaré map is a discrete dynamical system that

represents the continuous periodic flow of another system. The PSS can be used as a qualitative chaos indicator, since it allows us to visualize the dynamics of Hamiltonian systems.

The numerical computation of the PSS described in (Henon, 1982) involves successive intersections of an orbit in an N-dimensional phase space with an (N-1)-dimensional surface of section S. Given an N-dimensional, autonomous dynamical system

$$\begin{aligned} \frac{dx_1}{dt} &= f_1(x_1, ..., x_{2N}) \\ \frac{dx_2}{dt} &= f_2(x_1, ..., x_{2N}) \\ &\vdots \\ \frac{dx_{2N}}{dt} &= f_N(x_1, ..., x_{2N}), \end{aligned} \tag{2.2.1}$$

the surface of section S is defined by

$$S(x_1, ..., x_{2N}) = 0, \tag{2.2.2}$$

and the dynamical system (2.2.1) defines a Poincaré map of S on itself. We begin by numerically integrating (2.2.1) and evaluating S given by (2.2.2) at each point until there is a crossing of the surface in a particular direction. This is illustrated in Figure 2.1. We then proceed to find the point of intersection using an appropriate integration scheme. For simplicity, let us assume $S = x_1 - a$ where a is a constant. To find the point of intersection with the surface, we let x_1 be the independent variable. This is achieved by dividing the last $2N - 1$ equations in (2.2.1) by the first equation and inverting the first equation as shown below:

$$\begin{aligned} \frac{dt}{dx_1} &= \frac{1}{f_1} \\ \frac{dx_2}{dx_1} &= \frac{f_2}{f_1} \\ &\vdots \\ \frac{dx_{2N}}{dx_1} &= \frac{f_{2N}}{f_1}. \end{aligned} \tag{2.2.3}$$

In practice, we integrate (2.2.1) until there is an intersection with S and then integrate (2.2.3) with x_1 as its independent variable for one step with $a - x_1$ as the integration step. This integration brings us on the surface of section $S = x_1 - a$. Next, we proceed with the integration of (2.2.1) until there is a new crossing and repeat the procedure with (2.2.3). A computer code for creating the PSS is presented in pseudo-code in Algorithm 1.

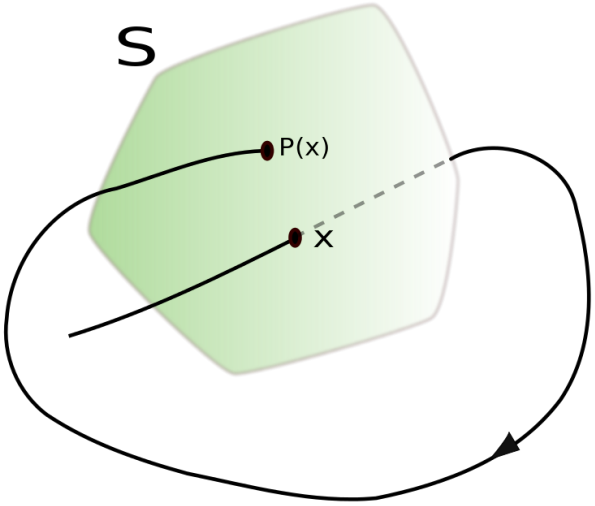

Figure 2.1: The PSS S, where **x** is the initial point and **P(x)** is the point of intersection with the surface **S** (image taken from Wikipedia).

Input Data: equations of motion (2.1.2), initial condition for the orbit $\mathbf{x}(0)$, PSS value x_{pss}, integration time step τ, equations (2.2.3) and maximal integration time T_{max}
Output : intersections with surface of section $x_j = x_{pss}$

set the counter, $k = 1$;
while $k\tau < T_{max}$ **do**
  evolve the orbit from time $t = (k-1)\tau$ to $t = k\tau$ i.e. compute $\mathbf{x}(k\tau)$;
  if $(x_{pss} - x_j(k\tau))(x_{pss} - x_j((k-1)\tau)) < 0$ *and* $x_{j+N}(k\tau) \geq 0$ *for some* $j \in \{1, 2, ..., N\}$ **then**
    set integration step $\lambda = x_{pss} - x_j((k-1)\tau)$;
    set the initial conditions $\mathbf{y}(0) :=$
    $(x_1((k-1)\tau), x_2((k-1)\tau), ..., x_{j-1}((k-1)\tau), x_{j+1}((k-1)\tau), ..., x_{2N}((k-1)\tau), (k-1)\tau)$;
    integrate (2.2.3) with $\mathbf{y}(0)$ for one time step using the $4th$ order Runge-Kutta method;
    store $\mathbf{y}(\lambda)$;
  end
  set the counter, $k = k + 1$;
end

Algorithm 1: Algorithm for the numerical computation of the PSS of a dynamical system. The program numerically integrates the equations of a trajectory up to a given maximal integration time $t = T_{max}$, detects and computes its intersections with a surface of section of the form $x_j - x_{pss} = 0$.

2.2.2 The Maximum Lyapunov Characteristic Exponent (mLCE). The Lyapunov Characteristic Exponents (LCEs) measure the exponential divergence of nearby orbits in a phase space. They were introduced by Lyapunov (1992) in his study of the stability of non-stationary solutions of ordinary differential equations. The LCEs are quantitative measures that capture the sensitive dependence of

dynamical systems on initial conditions.

The computation of the maximum LCE (mLCE) χ has been widely used for the practical determination of the chaotic nature of orbits (Benettin et al., 1980a,b). For a chaotic orbit, $\chi > 0$ while for a regular orbit, $\chi \to 0$ following the power law $\chi \propto \frac{\ln t}{t} \approx \frac{1}{t}$. The mLCE is given by

$$\chi = \lim_{t\to\infty} \frac{1}{t} \ln \frac{\|\mathbf{w}(t)\|}{\|\mathbf{w}(0)\|}, \tag{2.2.4}$$

where $\|.\|$ is the Euclidean norm. It is important to mention that the computation of the mLCE can be done in two ways. The first case involves the evolution of two nearby orbits with phase space distance of about $10^{-7} - 10^{-6}$. The second case involves the evolution of deviation vectors using the variational equations. The latter is an improvement of the former as it allows the use of larger integration time steps, and eliminates the difficulty of choosing suitable initial distance between nearby orbits (Contopoulos et al., 1978).

We will proceed with the illustration of the numerical computation of the mLCE involving the evolution of two nearby orbits or the simultaneous evolution of the initial orbit and an initial deviation vector of norm 1. After every $t = \tau$ time units we compute an estimation of the mLCE as described in (2.2.4) and normalise the evolved deviation vector $\mathbf{w}(l\tau)$ to $\hat{\mathbf{w}}(l\tau)$, $l = 1, 2, \cdots$. An algorithm for estimating χ through (2.2.4) can be found in (Skokos, 2010).

Spectrum of LCEs

Following (Skokos, 2010) the spectrum of LCEs is given by

$$\chi_1(\mathbf{x}) \geq \chi_2(\mathbf{x}) \geq \cdots \geq \chi_N(\mathbf{x}) \geq -\chi_N(\mathbf{x}) \geq \cdots \geq -\chi_2(\mathbf{x}) \geq -\chi_1(\mathbf{x})$$

and the sum of all LCEs in $2N$D symplectic maps and ND autonomous Hamiltonian systems is

$$\sum_{i=1}^{2N} \chi_i(\mathbf{x}) = 0.$$

It is further shown that the spectrum of LCEs comprises pairs of values with opposite signs, i.e.,

$$\chi_i(\mathbf{x}) = \chi_{2N-i+1}(\mathbf{x}), \quad i = 1, 2, \cdots, N. \tag{2.2.5}$$

In particular, in the case of autonomous Hamiltonian systems, due to the fact that a deviation vector grows linearly in time in the direction along the flow at least a pair of the LCEs vanishes, i.e.,

$$\chi_N(\mathbf{x}) = \chi_{N+1}(\mathbf{x}) = 0. \tag{2.2.6}$$

Practically, computing the p largest LCEs with $1 < p \leq 2N$ using the standard method of Benettin et al. (1980a,b) involves the time evolution of p initial orthonormal deviation vectors to $t = \tau$, where the evolved deviation vectors are replaced by a new set of orthonormal deviation vectors obtained by the Gram-Schmidt orthonormalisation method. The computation of the LCEs follows subsequently. An algorithm for computing the whole spectrum of LCEs using the standard method as described above can be found in (Skokos, 2010).

2.2.3 The Smaller Alignment Index (SALI). The need to overcome the slow convergence of LCEs to their limiting value (2.2.4) led to the introduction of the Smaller Alignment Index (SALI) as a fast and efficient chaos indicator (Skokos, 2001; Skokos et al., 2004; Skokos and Manos, 2016). The computation of the SALI involves the evolution of two initial deviation vectors and the identification of the possible alignment of these deviation vectors.

Practically, we evolve the deviation vectors following the system's dynamics normalizing them to unity after a fixed number of evolution steps using the Euclidean norm. Afterwards, we compute the SALI using defined quantities

$$d_- \equiv \|\hat{\mathbf{w}}_1(t) - \hat{\mathbf{w}}_2(t)\|, \quad d_+ \equiv \|\hat{\mathbf{w}}_1(t) + \hat{\mathbf{w}}_2(t)\|, \quad \text{with } \hat{\mathbf{w}}_i(t) = \frac{\mathbf{w}_i(t)}{\|\mathbf{w}_i(t)\|},\ i = 1, 2$$

as the parallel alignment index and antiparallel alignment index, respectively. Then

$$\text{SALI} = \min\{d_-, d_+\}. \tag{2.2.7}$$

Discriminating between ordered and chaotic motion using the SALI is easily achieved since the regular motion occurs on a torus on which initial deviation vectors eventually become tangent after a short period of time. This implies that two distinct initial vectors become tangent to, in general, different directions on the torus, hence different sequences of vectors are produced. As a result, none of the alignment indexes tend to zero, but they rather tend to a constant value. On the other hand, for chaotic motion, any two distinct initial deviation vectors eventually coincide in the direction of the most unstable manifold or they have same magnitude but opposite direction. Consequently, one of the alignment indexes tend to zero. Thus, the SALI tends to zero for chaotic orbits and tends to a positive value for regular orbits. An analysis of the behaviour of the SALI for chaotic orbits carried out in (Skokos et al., 2004) yields

$$\text{SALI} \propto e^{-(\chi_1 - \chi_2)t}, \tag{2.2.8}$$

with χ_1 and χ_2 being the two largest LCEs.

It is important to note that for 2D-maps, ordered motion occurs on a 1D torus. So, any two distinct initial deviation vectors become tangent to the torus after a short period of time tending to either coincide or become equal with opposite direction. In that case the SALI behaviour of regular orbits is

$$\text{SALI} \propto \frac{1}{n^2}, \tag{2.2.9}$$

with n denoting the map's iterations. Hence, both regular and chaotic orbits tend to zero but, they do so at different time rates.

An algorithm for the computation of SALI as presented in (2.2.7) can be found in (Skokos and Manos, 2016).

2.2.4 The Generalized Alignment Index (GALI). The use of two deviation vectors for the computation of the SALI results in the dependence of the SALI for chaotic orbits on the two largest LCEs. Thus in the rare but not impossible case of a chaotic orbit with $\chi_1 \approx \chi_2$ the SALI will converge to zero slowly resulting in a delay in the accurate determination of the orbit's nature. This problem can be overcome by the extension of the index's dependence on more than two LCEs, and has led to the introduction of the GALI of order k (GALI_k) (Skokos et al., 2007; Skokos and Manos, 2016) defined as

$$\text{GALI}_k = \|\hat{\mathbf{w}}_1(t) \wedge \hat{\mathbf{w}}_2(t) \wedge \ldots \wedge \hat{\mathbf{w}}_k(t)\|^{[1]}.$$

[1] $\mathbf{x} \wedge \mathbf{y}$ is the wedge product of $\mathbf{x}$ and $\mathbf{y}$.

It is important to note that the number k of deviation vectors should not exceed the dimension of the phase space of the system, in order to avoid the linear dependence of the k vectors and the corresponding phase volume having a zero value. It follows that GALI_k and SALI have same discriminating ability as $\text{GALI}_k = 0$ (SALI=0) implies linear dependence while $\text{GALI}_k > 0$ (SALI >0) implies linear independence. This connection has been shown in (Skokos et al., 2007) as

$$\text{GALI}_2 = \text{SALI} \cdot \frac{\max\{\|\hat{\mathbf{w}}_1(t) + \hat{\mathbf{w}}_2(t)\|, \|\hat{\mathbf{w}}_1(t) - \hat{\mathbf{w}}_2(t)\|\}}{2}. \tag{2.2.10}$$

Thus, the conclusion that

$$\text{GALI}_2 \propto \text{SALI}$$

is as a result of $\max\{\|\hat{\mathbf{w}}_1(t)+\hat{\mathbf{w}}_2(t)\|$ being a number in the interval $[\sqrt{2}, 2]$. This equivalence establishes the fact that the GALI is an extension of the SALI.

For the evaluation of the GALI we consider the $k \times 2N$ matrix $\mathbf{P}(t)$ having the coordinates of the k unit deviation vectors $\hat{\mathbf{w}}_i(t)$ as rows i.e.,

$$\mathbf{P}(t) = \begin{bmatrix} w_{11}(t) & w_{12}(t) & \dots & w_{12N}(t) \\ w_{21}(t) & w_{22}(t) & \dots & w_{22N}(t) \\ \vdots & \vdots & & \vdots \\ w_{k1}(t) & w_{k2}(t) & \dots & w_{k2N}(t) \end{bmatrix}. \tag{2.2.11}$$

According to Skokos et al. (2008) the index is the product of the singular values v_i, $i = 1, 2, ..., k$ of the matrix $\mathbf{P}^T$ (^{T} is transpose), i.e.,

$$\text{GALI}_k = \prod_{i=1}^{k} v_i. \tag{2.2.12}$$

The singular values are obtained by carrying out the Singular Value Decomposition (SVD) procedure on $\mathbf{P}^T$ (Golub and Reinsch, 1970).

In practice, the computation of the GALI of order k i.e., GALI_k involves the evolution of k distinct, random, orthonormal initial vectors. After every time $t = \tau$ units we normalize the evolved deviation vectors $\mathbf{w}_i(l\tau)$, $i = 1, ..., k$, $l = 1, 2, ...$ to the unit vectors $\hat{\mathbf{w}}_i(l\tau)$ and set them as rows of $\mathbf{P}(t)$ as described in (2.2.11). Afterwards, we compute GALI_k as the product of the singular values of $\mathbf{P}(t)$ following (2.2.12). An algorithm for the computation of GALI can be found in (Skokos and Manos, 2016).

Furthermore, as shown by Skokos et al. (2007), the behaviour of GALI_k of regular orbits is given by

$$\text{GALI}_k(t) \propto \begin{cases} \text{constant} & \text{if } 2 \le k \le N \\ \frac{1}{t^{2(k-N)}} & \text{if } N < k \le 2N. \end{cases} \tag{2.2.13}$$

In the case of chaotic orbits, GALI_k tends to zero exponentially fast following the law

$$\text{GALI}_k(t) \propto \exp\{-[(\chi_1 - \chi_2) + (\chi_1 - \chi_3) + \dots + (\chi_1 - \chi_k)]t\}, \tag{2.2.14}$$

which depends on the values of the k largest LCEs.

2.3 Models

In order to illustrate the use of the methods described in Section 2.2 we implement them for the study of some simple dynamical systems.

2.3.1 The Hénon-Heiles Hamiltonian. As a simple Hamiltonian model we consider the well-known $2D$ Hénon-Heiles system (Henon and Heiles, 1964) described by the Hamiltonian function

$$H_2 = \frac{1}{2}(p_x^2 + p_y^2) + \frac{1}{2}(x^2 + y^2) + x^2 y - \frac{1}{3}y^3. \tag{2.3.1}$$

This model is a continuous, conservative, autonomous system and describes the motion of stars in a galactic centre, with the motion restricted to a plane. In this section, we formulate the system's equations of motion and the variational equations and numerically analyse its dynamics.

Equations of motion and Variational Equations

We formulate the equations of motion from (2.1.2) with

$$\mathbf{J}_4 = \begin{bmatrix} 0 & 0 & 1 & 0 \\ 0 & 0 & 0 & 1 \\ -1 & 0 & 0 & 0 \\ 0 & -1 & 0 & 0 \end{bmatrix} \quad \text{and} \quad \mathbf{DH}_2 = \begin{bmatrix} p_x \\ p_y \\ -x - 2xy \\ -y - x^2 + y^2 \end{bmatrix}$$

to get

$$\dot{\mathbf{x}} = \begin{bmatrix} \dot{x} \\ \dot{y} \\ \dot{p_x} \\ \dot{p_y} \end{bmatrix} = \begin{bmatrix} p_x \\ p_y \\ -x - 2xy \\ -y - x^2 + y^2 \end{bmatrix}. \tag{2.3.2}$$

Therefore, the equations of motion are

$$\begin{cases} \dot{x} = p_x \\ \dot{y} = p_y \\ \dot{p_x} = -x - 2xy \\ \dot{p_y} = -y - x^2 + y^2 \end{cases}. \tag{2.3.3}$$

From (2.1.3), the variational equations are given by

$$\dot{\mathbf{w}} = \begin{bmatrix} \dot{\delta x} & \dot{\delta y} & \dot{\delta p_x} & \dot{\delta p_y} \end{bmatrix}^T = \mathbf{J}_4 \cdot \mathbf{D}^2\mathbf{H} \cdot \mathbf{w},$$

with

$$\mathbf{D}^2\mathbf{H} = \begin{bmatrix} \frac{\partial^2 H}{\partial x \partial x} & \frac{\partial^2 H}{\partial x \partial y} & \frac{\partial^2 H}{\partial x \partial p_x} & \frac{\partial^2 H}{\partial x \partial p_y} \\ \frac{\partial^2 H}{\partial y \partial x} & \frac{\partial^2 H}{\partial y \partial y} & \frac{\partial^2 H}{\partial y \partial p_x} & \frac{\partial^2 H}{\partial y \partial p_y} \\ \frac{\partial^2 H}{\partial p_x \partial x} & \frac{\partial^2 H}{\partial p_x \partial y} & \frac{\partial^2 H}{\partial p_x \partial p_x} & \frac{\partial^2 H}{\partial p_x \partial p_y} \\ \frac{\partial^2 H}{\partial p_y \partial x} & \frac{\partial^2 H}{\partial p_y \partial y} & \frac{\partial^2 H}{\partial p_y \partial p_x} & \frac{\partial^2 H}{\partial p_y \partial p_y} \end{bmatrix} = \begin{bmatrix} 1 + 2y & 2x & 0 & 0 \\ 2x & 1 - 2y & 0 & 0 \\ 0 & 0 & 1 & 0 \\ 0 & 0 & 0 & 1 \end{bmatrix}.$$

We get

$$\dot{\mathbf{w}} = \begin{bmatrix} \dot{\delta x} \\ \dot{\delta y} \\ \dot{\delta p_x} \\ \dot{\delta p_y} \end{bmatrix} = \begin{bmatrix} \delta p_x \\ \delta p_y \\ \delta x(-1-2y) - 2x\delta y \\ -2x\delta x + (-1+2y)\delta y \end{bmatrix}.$$

Therefore, the variational equations are

$$\begin{cases} \dot{\delta x} = \delta p_x \\ \dot{\delta y} = \delta p_y \\ \dot{\delta p_x} = \delta x(-1-2y) - 2x\delta y \\ \dot{\delta p_y} = -2x\delta x + (-1+2y)\delta y. \end{cases} \tag{2.3.4}$$

Numerical Investigations

Figure 2.2(a) shows the PSS of the Hénon-Heiles system at $x = 0$ with initial energy $H_0 = 0.125$. As can be seen in the figure the 4 dimensional system is represented by a 2 dimensional system with $x = 0$ and $p_x \geq 0$. This enables us to visualise the dynamics of the system, as regular orbits create smooth curves while chaotic orbits generate scattered dots. Numerically, orbits were evolved and intersections with the surface $x = 0$ were computed using the fourth order Runge-Kutta method.

Contrary to Figure 2.2(a), Figures 2.2(b), 2.3(a), and 2.3(b) depict a quantitative analysis of the chaotic and regular nature of orbits of the system, using the computation of the mLCE. Initial conditions were obtained from (Benettin et al., 1980a). In this analysis, two methods were employed for the computation of the mLCE χ, namely: the time evolution of nearby orbits denoted by 2p in Figure 2.2(b) and the time evolution of the deviation vector using the variational equations denoted by tm in Figure 2.2(b). For the 2p method, 2 nearby orbits with distance 10^{-7} were evolved for the computation of χ. A comparison of the aforementioned methods shows equivalence of the methods, as seen in 2.2(b). Furthermore, as predicted theoretically, chaotic orbits have a positive mLCE i.e., $\chi > 0$ while for regular orbits χ tends to zero.

Moreover, Figures 2.4(a) and 2.4(b) show that $\chi_1 = -\chi_3$ and $\chi_2 = -\chi_4$. It is also shown that $\chi_2 = -\chi_4 = 0$, i.e., they vanish due to the autonomous nature of the Hamiltonian. Thus, these results correspond to the theoretical prediction of (2.2.5) and (2.2.6). The equivalence of the time evolution of nearby orbits and the variational equations in the computation of the spectrum of LCEs is also established.

In the same vein, the quantification of the chaoticity of orbits of the system is further presented by the computation of the SALI. This can be seen in Figures 2.5(a) and 2.6. Here we notice a contrast with respect to the mLCE, as chaotic orbits quickly tend to a zero SALI value while regular orbits tend to a constant, positive SALI value. It can be seen in Figure 2.6(b) that the exponential decay of the SALI for chaotic orbit is in accordance with (2.2.8) with $\chi_1 = 0.05$ and $\chi_2 = 0$. The dashed line in Figure 2.6(b) corresponds to a function proportional to $e^{-\chi_1 t}$. The value of χ_1 was estimated by computing the mean value of the mLCE of the chaotic orbit, with initial conditions $x = 0, p_x > 0, y = 0.2, p_y = 0.14, H = 0.125$. Also, we compute SALI using the time evolution of nearby orbits and its comparison with the variational equations method is shown in Figure 2.6(a). Hence, the equivalence of both methods is shown. This behaviour corresponds to the theoretical prediction of the SALI and clearly discriminates chaotic and regular orbits.

We also quantify chaos by the GALI method. This involves the investigation of the $GALI_2$, the $GALI_3$, and the $GALI_4$, which is simply the evolution of 2, 3, and 4 deviation vectors, respectively. Similar to the SALI, Figures 2.5(b), 2.7(a), and 2.7(b) show that the $GALI_3$ and $GALI_4$ for regular orbits, tend to zero following the power law t^{-2} and t^{-4}, respectively, while for $GALI_2$ it tends to a constant, positive value. On the other hand, the $GALI_2$, $GALI_3$ and $GALI_4$ for chaotic orbits tend to zero with slopes corresponding to functions proportional to $e^{-\chi_1 t}$, $e^{-2\chi_1 t}$ and $e^{-4\chi_1 t}$, respectively. In particular, 2.5(b) shows the equivalence of the $GALI_2$ and the SALI, which is in agreement with the theoretical claim that

$$GALI_2 \propto SALI.$$

Also, we can see that $GALI_4$ has the fastest rate of convergence while $GALI_2$ has the slowest rate of convergence. This is because for $GALI_4$ the chaotic behaviour depends on 4 LCEs while for $GALI_2$ it depends on the 2 largest LCEs, as 4 and 2 deviation vectors are evolved, for $GALI_4$ and $GALI_2$. Thus, an increase in the number of deviation vectors increases the efficiency of the method. Furthermore, the exponential decay of GALIs for chaotic orbits according to (2.2.14) is shown in Figures 2.8(b), 2.9(b), and 2.10(b). Finally, the behaviour of GALIs for regular orbits corresponding to the theoretical prediction (2.2.13), as well as the equivalence of the time evolution of nearby orbits and the variational equations method, are shown in Figures 2.8(a), 2.9(a), and 2.10(a), respectively.

We conclude that all methods correctly capture the nature of the studied orbits with the GALIs being the most efficient and the mLCE the least efficient, as more time is needed to accurately discriminate chaotic and regulars orbits using the mLCE. This is shown in Figure 2.7(b) where the exponential decay of chaotic orbits occur at time $t \approx 10^{2.3}$ using the $GALI_4$ method, while in Figure 2.3(b) the convergence of chaotic orbits occur at time $t \approx 10^4$. Furthermore, we have been able to establish the equivalence of the evolution of nearby orbits and the variational equations method for the accurate computation of these quantitative chaos indicators. Thus, these numerical tools analysed above are sufficient for the qualitative and quantitative investigation of chaotic dynamics of the Hénon-Heiles system.

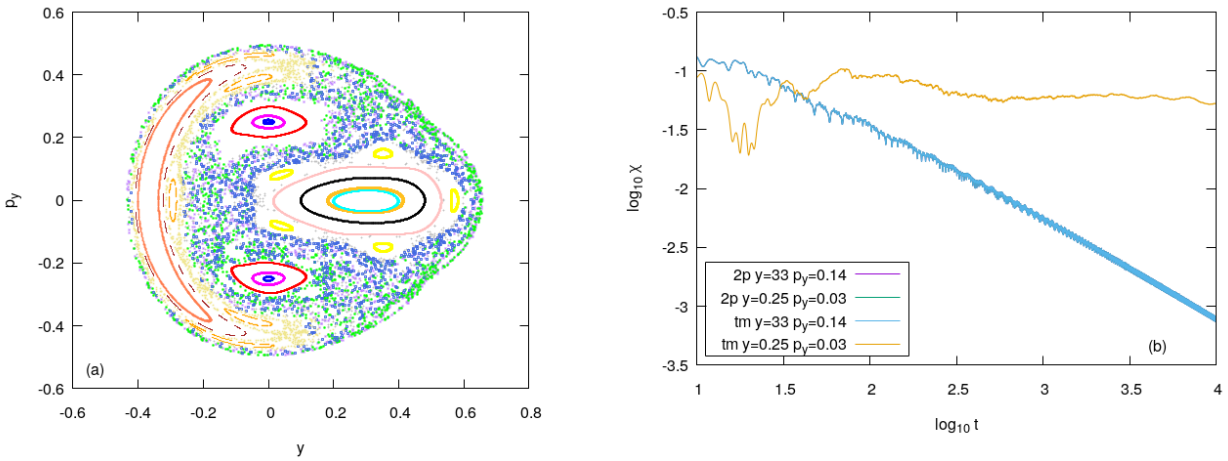

Figure 2.2: (a)The PSS of the Hénon-Heiles system, defined by $x = 0, p_x > 0, H = 0.125$. (b) Plots of the comparison of the time evolution of the mLCE against time, with initial conditions on the PSS of $x = 0$ (a), for $y = 0.25$, $p_y = 0.03$ (chaotic orbit) and $y = 0.33$, $p_y = 0.14$ (regular orbit). The computation was done using the variational equations (curves denoted by tm) and by the time evolution of nearby orbits (curves denoted by 2p). The curves of the two methods practically overlap. The axes are in logarithmic scale.

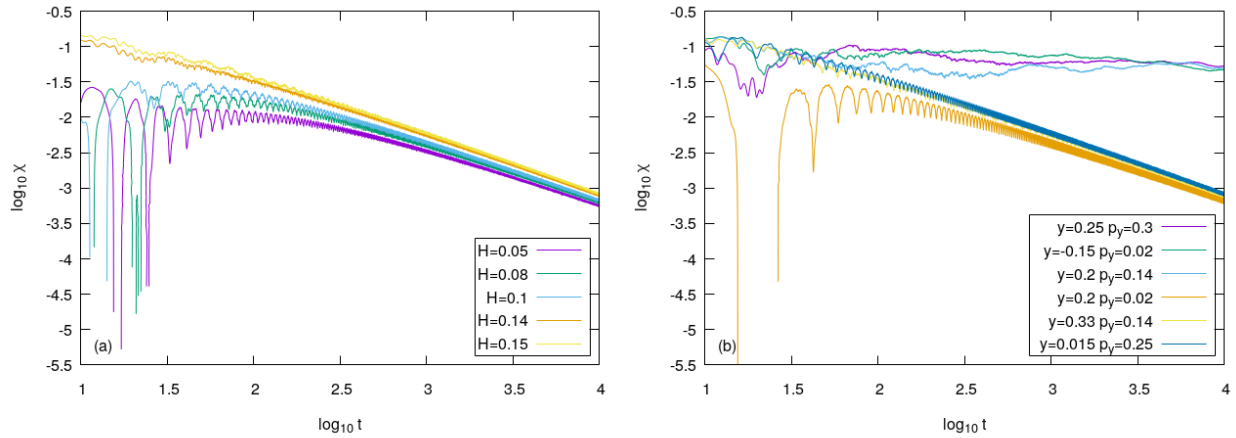

Figure 2.3: Plots of the time evolution of the mLCE χ against time for different orbits of the Hénon-Heiles system. (a) Regular orbits with initial conditions $x = 0, y = 0.20, p_x > 0, p_y = 0.05$; (b) chaotic and regular orbits with initial conditions $x = 0, p_x > 0, H = 0.125$. The axes are in logarithmic scale.

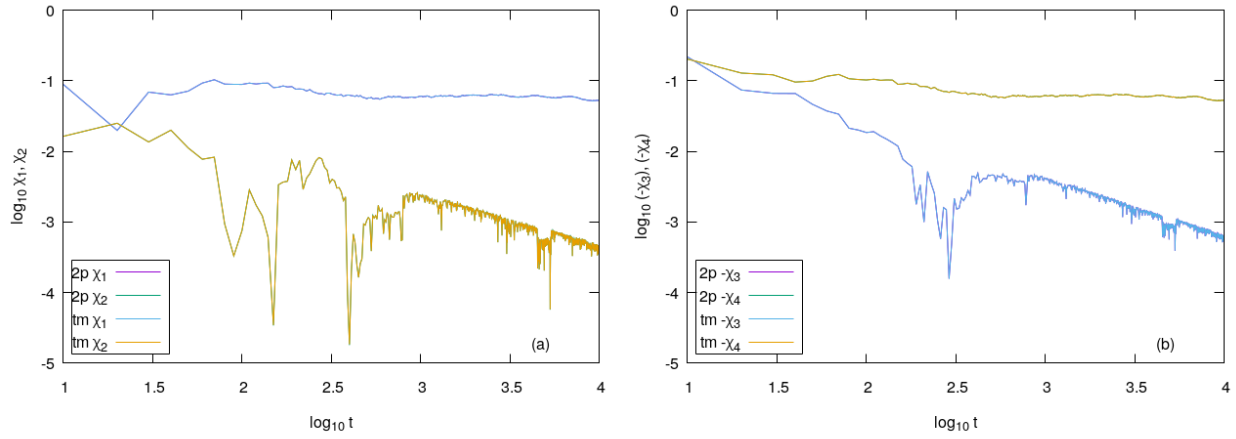

Figure 2.4: Plots of the comparison of time evolution of the LCEs against time for the chaotic orbit of the Hénon-Heiles system, with initial conditions $x = 0, y = 0.25, p_y = 0.3, H = 0.125$, using the integration of the variational equations method (curves denoted by tm) and the time evolution of nearby orbits method (curves denoted by 2p). The curves of the two methods practically overlap. The axes are in logarithmic scale.

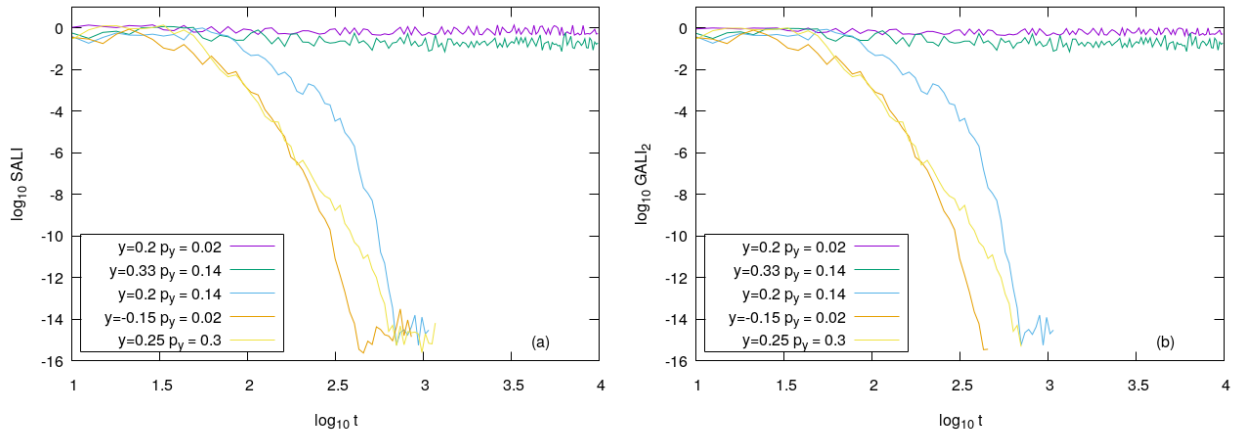

Figure 2.5: Plots of the time evolution of (a) the SALI and (b) the $GALI_2$ against time for different orbits of the Hénon-Heiles system, with $x = 0, p_x > 0, H = 0.125$. The axes are in logarithmic scale.

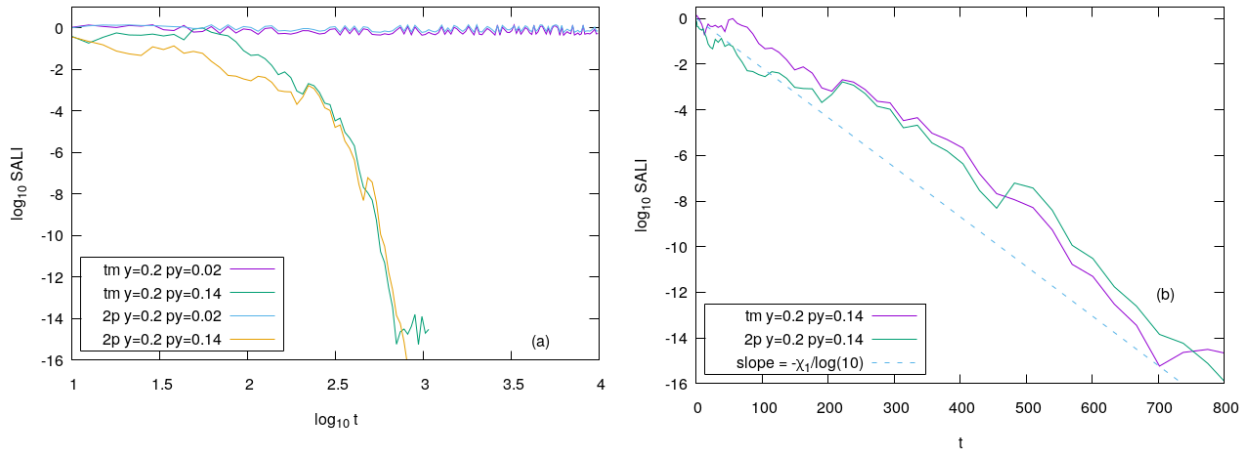

Figure 2.6: Plots of the comparison of the time evolution of the SALI against time for different orbits of the Hénon-Heiles system, using the integration of the variational equations method (curves denoted by tm) and the time evolution of nearby orbits method (curves denoted by 2p), for $x = 0, p_x > 0, H = 0.125$. Both axes are in logarithmic scale in (a), while time is linear in (b). The slope of the dashed line in (b) for the chaotic orbit is proportional to $e^{-\chi_1 t}$ and is calculated using the mLCE $\chi_1 = 0.05$.

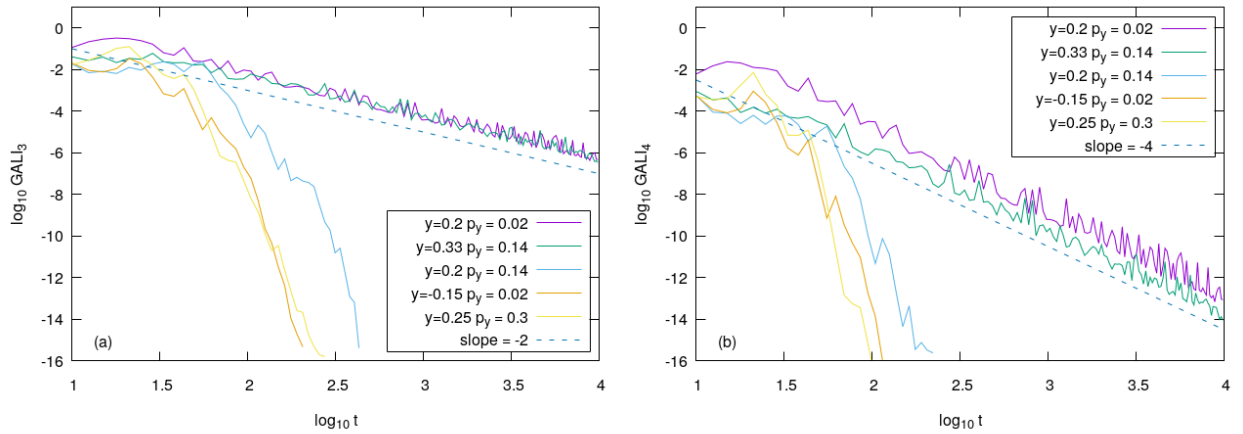

Figure 2.7: Plots of the time evolution of (a) the GALI_3 and (b) the GALI_4 against time for different orbits of the Hénon-Heiles system, with $x = 0, p_x > 0, H = 0.125$. The axes are in logarithmic scale.

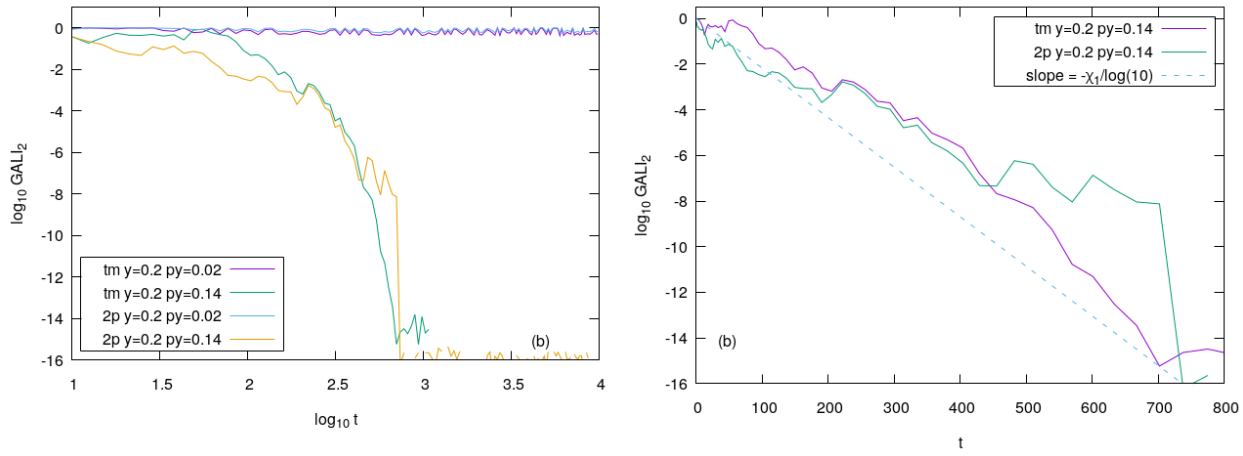

Figure 2.8: Same as Figure 2.6, but for the GALI_2.

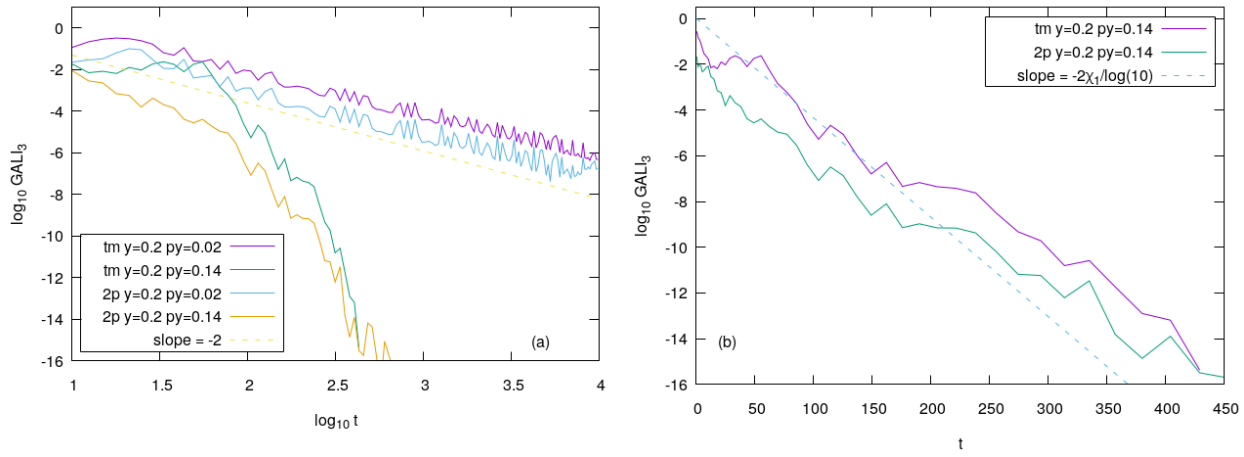

Figure 2.9: Same as Figure 2.6, but for the $GALI_3$ and the slope of the dashed line in (b) for the chaotic orbit is proportional to $e^{-2\chi_1 t}$.

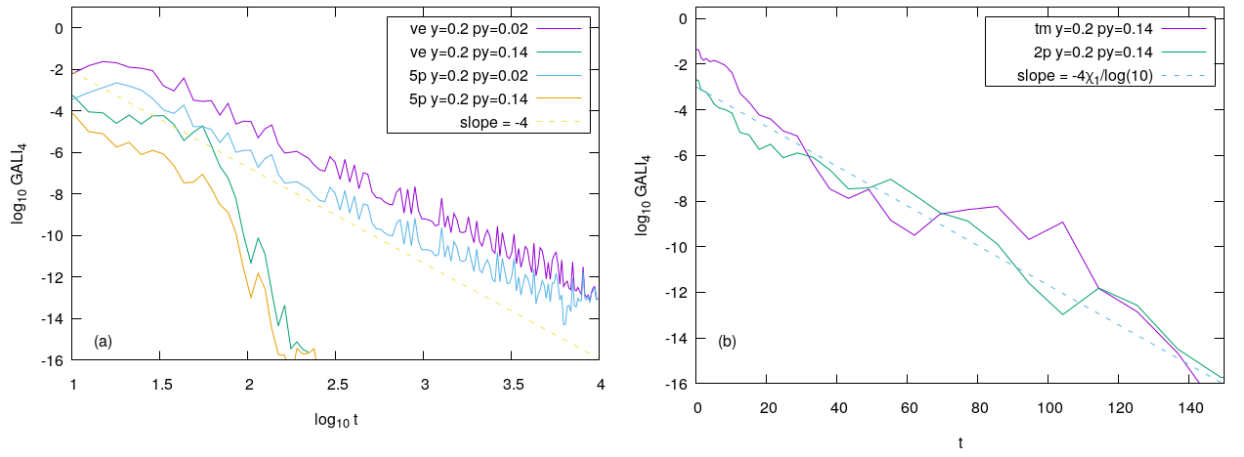

Figure 2.10: Same as Figure 2.6, but for the $GALI_4$ and the slope of the dashed line in (b) for the chaotic orbit is proportional to $e^{-4\chi_1 t}$

2.3.2 2D Symplectic Map. In the previous section, we dealt with continuous, autonomous Hamiltonian systems. Now, we extend our analysis to the area-preserving 2D standard map (Chirikov, 1979)

$$\begin{aligned} x_{1,n+1} &= x_{1,n} + x_{2,n} \\ x_{2,n+1} &= x_{2,n} - \nu \sin(x_{1,n} + x_{2,n}) \qquad (mod\ 2\pi), \end{aligned} \tag{2.3.5}$$

which describes the general dynamics of area-preserving maps with divided phase space where chaotic and regular orbits coexist.

The tangent map of (2.3.5) is obtained from (2.1.6) as

$$\begin{aligned} \delta x_{1,n+1} &= \delta x_{1,n} + \delta x_{2,n} \\ \delta x_{2,n+1} &= -\nu \cos(x_{1,n} + x_{2,n}) \delta x_{1,n} - (1 - \nu \cos(x_{1,n} + x_{2,n})) \delta x_{2,n}. \end{aligned} \tag{2.3.6}$$

Numerical Investigation

Similar to the Hénon-Heiles system (2.3.1), we quantify the chaoticity of orbits of the 2D standard map by using the mLCE, the SALI and the GALI methods. As can be seen in Figures 2.11(a) and 2.11(b), the mLCE χ tends to zero for the regular orbit, with initial conditions $x_1 = 0.5, x_2 = 0$ (green curve), while it tends to a positive number for the chaotic orbit having initial conditions $x_1 = 3, x_2 = 0$ (purple curve). These behaviours are in agreement with the theoretical predictions. Moreover, Figure 2.11(b) shows the equivalence of the evolution of nearby orbits and the tangent map method for the computation of χ. This can be seen in the figure as the blue and purple curves corresponding to the mLCE of the regular orbit computed by using the tangent map and the evolution of nearby orbits are equivalent. Same behaviour is shown for green and yellow curves of the chaotic orbits in Figure 2.12(b).

Figure 2.12 correctly shows the properties of the spectrum of LCEs as $\chi_1 = -\chi_2$, where χ_1 and χ_2 correspond to the purple and green curves, respectively, for both regular and chaotic orbits. Thus, the results obtained are in good agreement with the theoretical prediction (2.2.5). As obtained in previous analyses, the equivalence of the evolution of nearby orbits and the tangent map method for the computation of the spectrum of LCEs is also shown in Figure 2.12 as the lines corresponding to the LCEs computed by using both methods practically coincide.

The results of Figure 2.13 are in agreement with the theoretical prediction of the behaviour of SALI and $GALI_2$ of regular and chaotic orbits of the 2D standard map. In particular, the equivalence for SALI and $GALI_2$ is shown, as in both cases the chaotic orbit (green curve) becomes $\approx 10^{-8}$ at $N \approx 200$ iterations, while the regular orbit (purple curve) tends to zero with slope $= -2$. One feature of the 2D standard map is the behaviour of the SALI/$GALI_2$ of regular orbits, as it decays at a slower rate than the SALI/$GALI_2$ of chaotic orbits according to the power law N^{-2}. This is because the deviation vectors eventually coincide or become opposite to each other, as a result of the regular motion lying on a one-dimensional torus. Furthermore, Figures 2.14(b) and 2.15(b) show that the SALI/$GALI_2$ of chaotic orbits decay exponentially with slope proportional to $e^{-2\chi_1 N}$, as theoretically predicted. Also, it is evident in Figures 2.14 and 2.15 that the evolution of nearby orbits and the tangent map methods are equivalent for the computation of SALI/$GALI_2$, as the chaotic orbit corresponding to the green and yellow curves decay exponentially, while the purple and blue curves corresponding to the regular orbit decay with slope $= -2$.

We conclude that all chaos indicators correctly describe the behaviour of studied orbits with the $GALI_2$/SALI methods being more efficient than the mLCE, as more time is needed to accurately discriminate chaotic and regular orbits by using the mLCE. This is evident in Figure 2.11 where the mLCE of the chaotic orbit converges to a constant value at $N \approx 31600$ iterations, while the $GALI_2$/SALI of the chaotic orbit decays to very small values at $N \approx 200$ iterations in Figure 2.13. Moreover, we have been able to establish the equivalence of the evolution of nearby orbits and the tangent map method for the accurate computation of these chaos indicators. Thus, these numerical tools analysed above are sufficient for the quantitative investigation of chaotic dynamics of the 2D standard map.

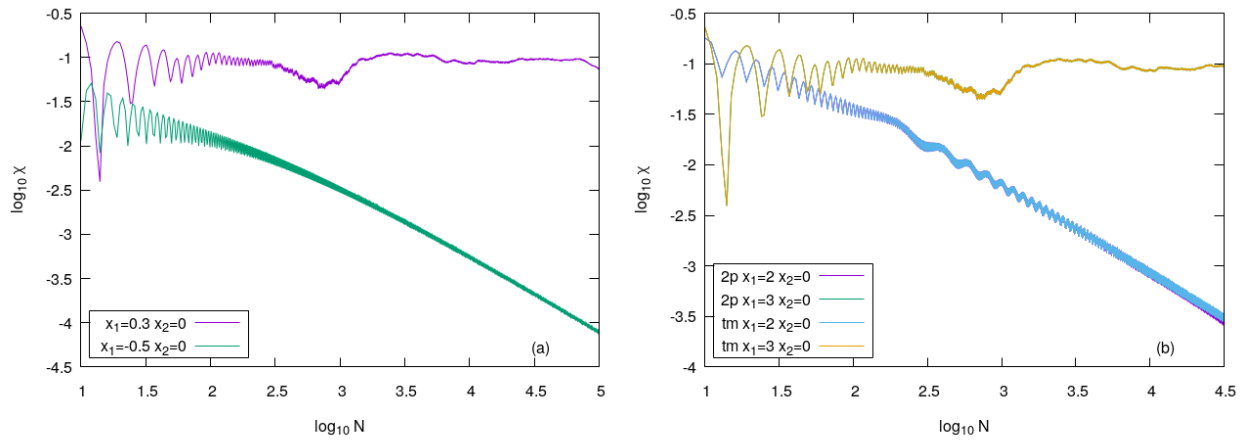

Figure 2.11: (a) Plots of the time evolution of the mLCE χ against time for different orbits of the 2D standard map (2.3.5) with $\nu = 0.5$. (b) Comparison of the time evolution of χ for regular and chaotic orbits of the 2D standard map, with $\nu = 0.5$, using the tangent map method (curves denoted by tm) and the evolution of nearby orbits method (curves denoted by 2p). In both panels axes are in logarithmic scale.

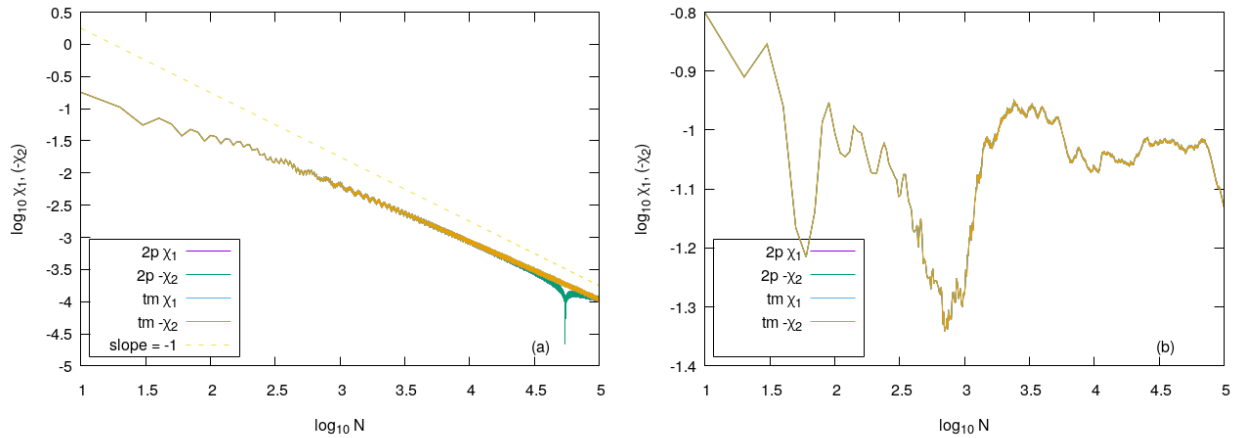

Figure 2.12: Plots of the time evolution of the LCEs χ_1, χ_2 against time for different orbits of the 2D standard map, with $\nu = 0.5$. (a) Regular orbit with initial condition $x_1 = 2$, $x_2 = 0$; (b) chaotic orbit with initial condition $x_1 = 3, x_2 = 0$. The computations were done by using the tangent map method (curves denoted by tm) and the evolution of nearby orbits method (curves denoted by 2p). The two methods practically overlap. The axes in both panels are in logarithmic scale.

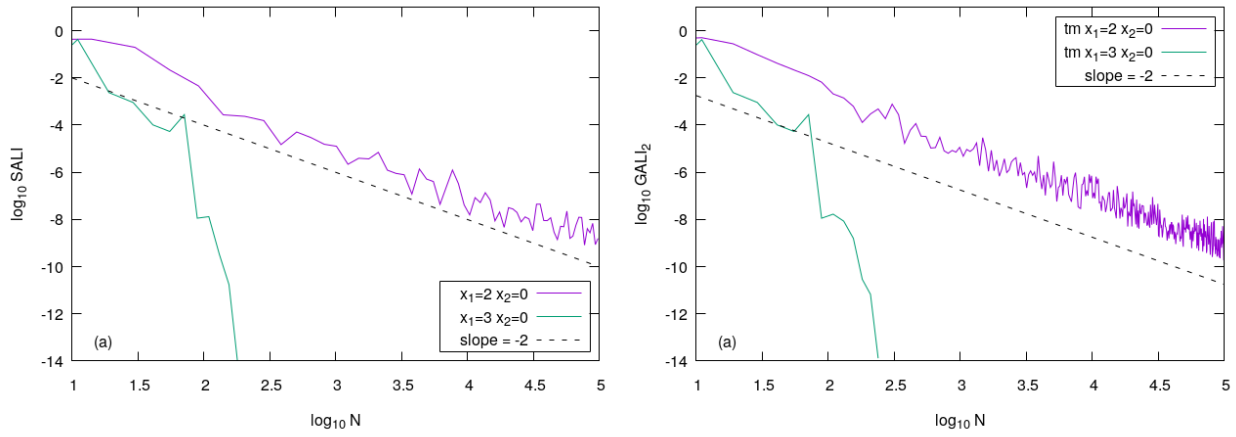

Figure 2.13: Plots of the time evolution of the SALI (a) and the $GALI_2$ (b) against time for different orbits of the 2D standard map, with the same initial conditions same as in Figure 2.12. Green and purple curves correspond to chaotic and regular orbits respectively; the dashed curve corresponds to the slope =-2. The axes in both panels are in logarithmic scale.

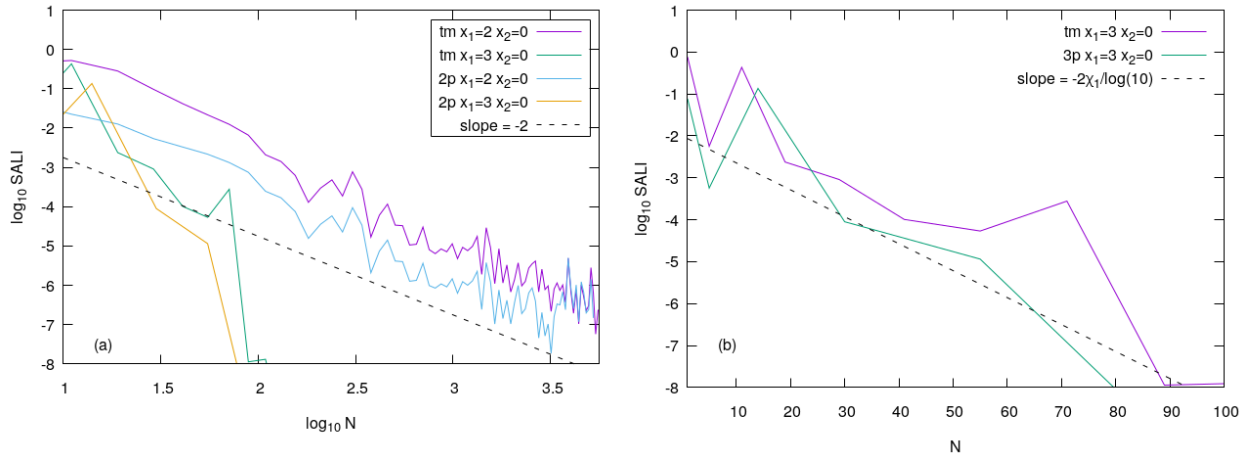

Figure 2.14: Comparison of the time evolution of the SALI against time for different orbits of the 2D standard map with the same initial conditions as in Figure 2.12, using the tangent map method (curves denoted by tm) and the evolution of nearby orbits method (curves denoted by 2p). Both axes are in logarithmic scale in (a), while the dashed curve corresponds to the slope =-2; the time axis is linear in (b) and the dashed curve related to the chaotic orbit corresponds to a function proportional to $e^{-2\chi_1 N}$, computed with $\chi_1 = -\chi_2 = 0.074$.

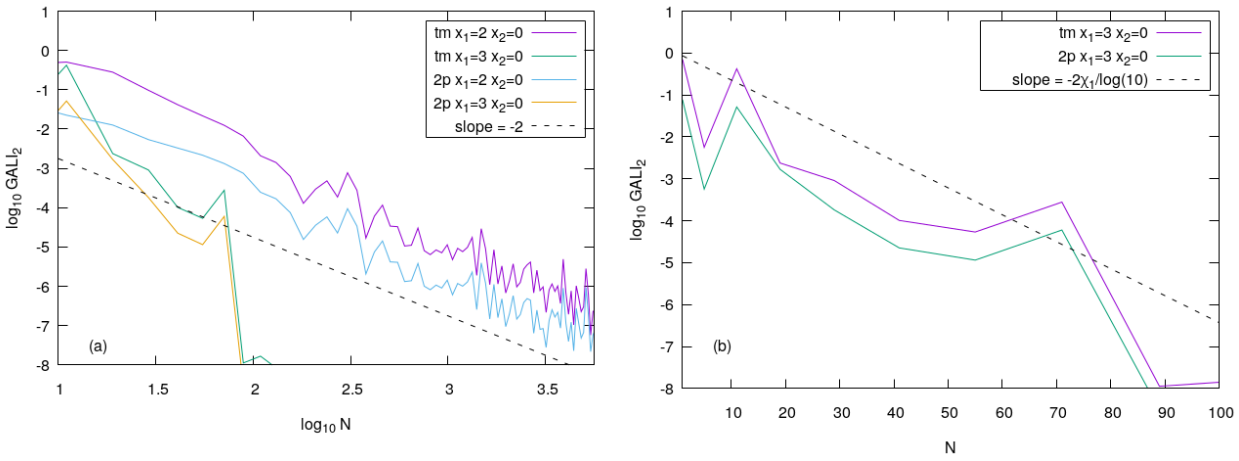

Figure 2.15: Same as Figure 2.14, but for $GALI_2$.

2.3.3 4D Symplectic Map. We also consider the 4D symplectic map Froeschlé (1972)

$$\begin{aligned} x_{1,n+1} &= x_{1,n} + x_{2,n} \\ x_{2,n+1} &= x_{2,n} - \nu \sin(x_{1,n} + x_{2,n}) - \mu[1 - \cos(x_{1,n} + x_{2,n} + x_{3,n} + x_{4,n})] \\ x_{3,n+1} &= x_{3,n} + x_{4,n} \\ x_{4,n+1} &= x_{4,n} - \kappa \sin(x_{3,n} + x_{4,n}) - \mu[1 - \cos(x_{1,n} + x_{2,n} + x_{3,n} + x_{4,n})] \end{aligned} \quad (mod\ 2\pi) \qquad (2.3.7)$$

The tangent map of (2.3.7) is obtained from (2.1.6) as

$$\begin{aligned} \delta x_{1,n+1} &= \delta x_{1,n} + \delta x_{2,n} \\ \delta x_{2,n+1} &= a_n \delta x_{1,n} + (1 + a_n)\delta x_{2,n} + b_n(\delta x_{3,n} + \delta x_{4,n}) \\ \delta x_{3,n+1} &= \delta x_{3,n} + \delta x_{4,n} \\ \delta x_{4,n+1} &= b_n(\delta x_{1,n} + \delta x_{2,n}) + c_n \delta x_{3,n} + (1 + c_n)\delta x_{4,n} \end{aligned} \qquad (2.3.8)$$

with

$$\begin{aligned} a_n &= -\nu \cos(x_1 + x_2) - \mu \sin(x_1 + x_2 + x_3 + x_4) \\ b_n &= -\mu \sin(x_1 + x_2 + x_3 + x_4) \\ c_n &= -\kappa \cos(x_3 + x_4) - \mu \sin(x_1 + x_2 + x_3 + x_4) \end{aligned} .$$

Numerical Investigation

As obtained in previous studied models, Figures 2.16(a), 2.17(b), and 2.18(b) correctly depict the behaviour of the mLCE and the spectrum of LCEs. First, in Figure 2.16(a) the mLCE for regular orbits (green and purple curves) tend to zero, while that of chaotic orbits (gold and light blue curves) tend to a constant positive value. Second, in Figure 2.17 it is shown that $\chi_1 = -\chi_4$ and $\chi_2 = -\chi_3$, with χ_1 and $-\chi_4$ corresponding to light blue and black curves, respectively, while χ_2 and $-\chi_3$ correspond to gold and red curves, respectively. It is evident that $\chi_2 = -\chi_3 = 0$ for chaotic orbits i.e., they vanish

while $\chi_1 = -\chi_4$ tend to a constant positive number. Final, the equivalence of the evolution of nearby orbits and the tangent map method is shown in Figure 2.17 as the curves corresponding to the LCEs using both methods are equivalent.

Moreover, the behaviour of the SALI for regular and chaotic orbits of Section 2.2.3 is depicted in Figures 2.16(b) and is in agreement with the theoretical prediction. In Figure 2.16(b) we can see that the mLCE of regular orbits (green and purple curves) decays exponentially, while it tends to a constant positive value for chaotic orbits (blue and gold curves). The SALI of the chaotic orbit, with initial conditions $x_1 = 3, x_2 = 0, x_3 = 0.5, x_4 = 0$ decays exponentially according to a function proportional to the exponent $e^{(\chi_1-\chi_2)N}$ (Figure 2.18(b)). Furthermore, in Figure 2.18 the equivalence of the evolution of nearby orbits and the tangent map methods for the computation of the SALI is evident, as the purple and light blue curves corresponding to the tangent map and evolution of nearby orbits methods, respectively are equivalent. Same equivalence is shown by the green and gold curves which correspond to the tangent map and the evolution of nearby orbits methods, respectively, but for the regular orbit.

In the same vein, Figures 2.19(b), 2.20(b), and 2.21(b) show the behaviour of the $GALI_2$, the $GALI_3$ and the $GALI_4$ of chaotic orbits, respectively in agreement to the theoretical prediction (2.2.14). This is evident as the $GALI_2$, the $GALI_3$ and the $GALI_4$ of the chaotic orbit with initial conditions $x_1 = 3, x_2 = 0, x_3 = 0.5, x_4 = 0$ decay exponentially according to functions proportional to $e^{(\chi_1-\chi_2)N}$, $e^{-2\chi_1 N}$ and $e^{-4\chi_1 N}$, respectively. On the other hand, Figures 2.19(a), 2.20(a), and 2.21(a) show the behaviour of the $GALI_2$, the $GALI_3$ and the $GALI_4$ of regular orbits. In particular, the $GALI_2$ tends to a constant positive value, while the $GALI_3$ and the $GALI_4$ decay following the power law N^{-2} and N^{-4}, respectively. Similar to previous numerical methods, the equivalence of the tangent map and the evolution of nearby orbits methods is shown in these results, as the purple and green curves corresponding to the tangent map method are equivalent to the gold and light blue curves which correspond to the evolution of nearby orbits method.

We conclude that the equivalence of the evolution of nearby orbits method and the tangent map method for the accurate computation of these quantitative chaos indicators has been established. These analyses are in good agreement with the theoretical predictions for the mLCE, the SALI and the GALI chaos indicators. Hence, are sufficient for the numerical investigation of chaos in continuous and discrete dynamical systems.

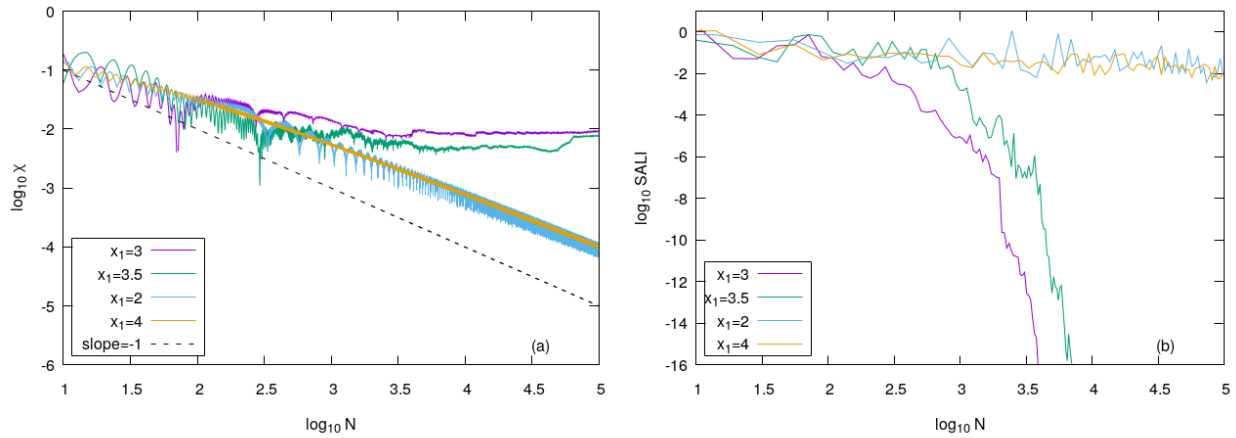

Figure 2.16: Plots of the time evolution of (a) χ and (b) the SALI against time for chaotic (purple and green curves) and regular (light blue and gold curves) orbits of the 4D symplectic map (2.3.7), with initial conditions $x_2 = 0, x_3 = 0.5, x_4 = 0$, $\nu = 0.1, \kappa = 0.1$, and $\mu = 0.001$. In both panels axes are in logarithmic scale.

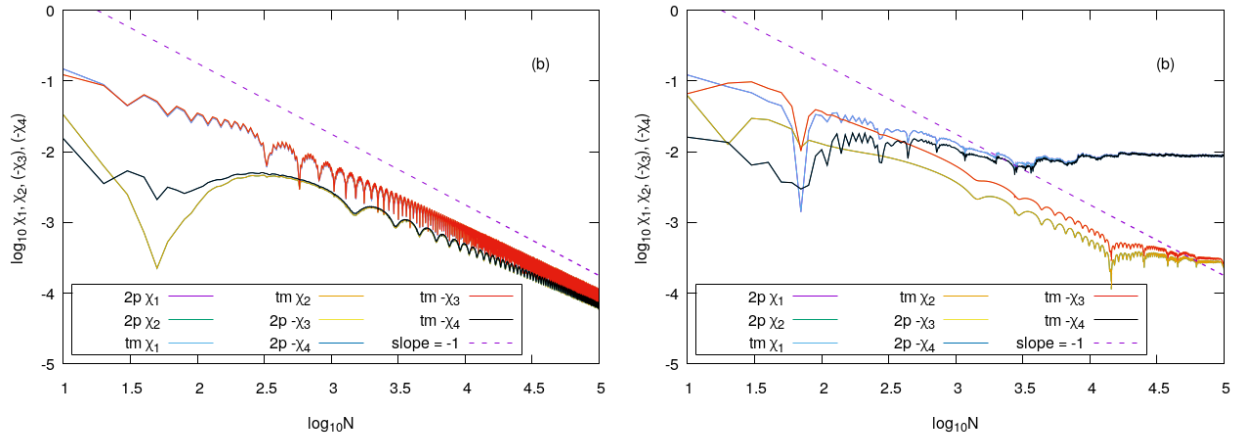

Figure 2.17: Comparison of the time evolution of the LCEs against time for (a) a regular orbit with initial conditions $x_1 = 2, x_2 = 0, x_3 = 0.5, x_4 = 0$, and (b) chaotic orbit with initial conditions $x_1 = 3, x_2 = 0, x_3 = 0.5, x_4 = 0$ of the 4D symplectic map, using the tangent map method (curves denoted by tm) and the evolution of nearby orbits method (curves denoted by 2p). In both panels axes are in logarithmic scale. For all orbits $\nu = 0.1, \kappa = 0.1$, and $\mu = 0.001$.

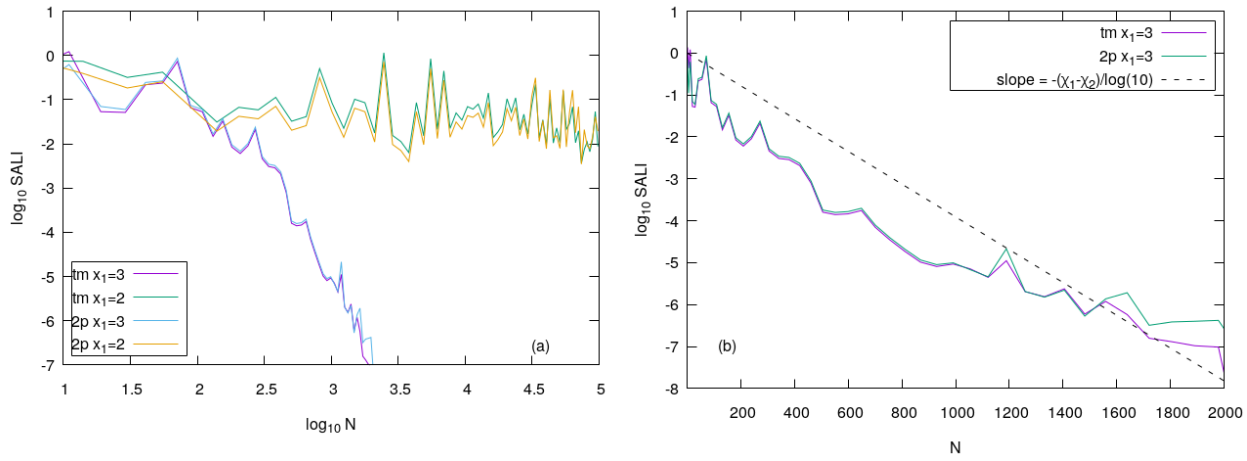

Figure 2.18: Comparison of the time evolution of the SALI against time for different orbits of the 4D symplectic map (2.3.7) having the same initial conditions as in Figure 2.16, using the tangent map method (curves denoted by tm) and the evolution of nearby orbits method (curves denoted by 2p). Both axes are in logarithmic scale in (a) and the time axis is linear in (b). In (b) is the dashed curve corresponds to a function proportional to $e^{-(\chi_1-\chi_2)N}$ with $\chi_1 = 0.0089, \chi_2 = 0.0002$.

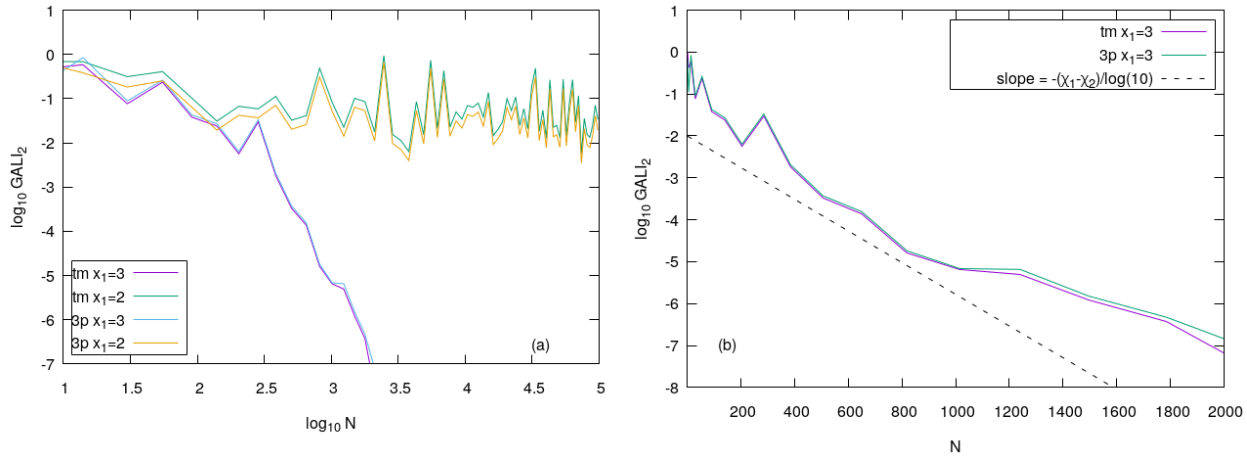

Figure 2.19: Same as Figure 2.18, but for $GALI_2$.

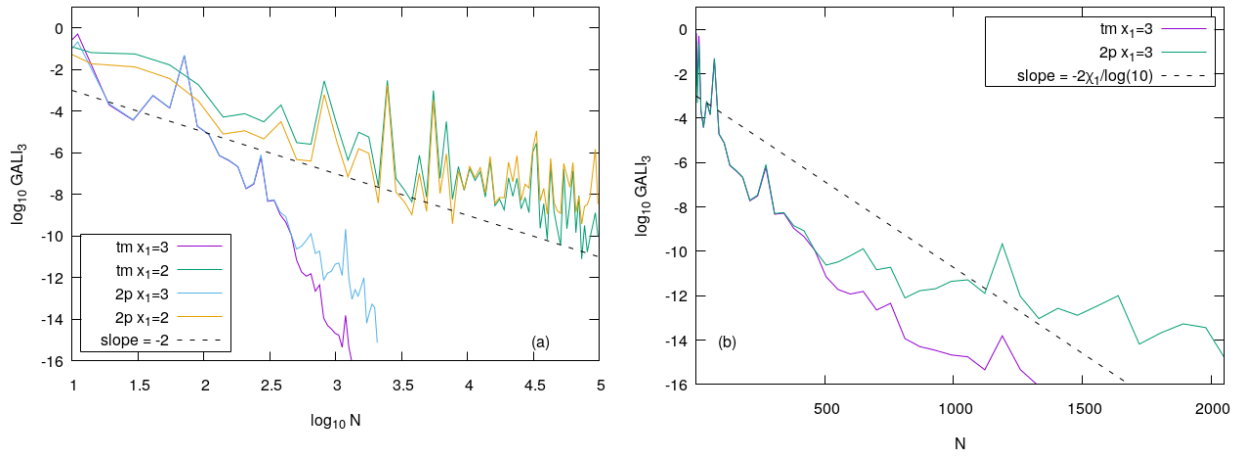

Figure 2.20: Same as Figure 2.18, but for GALI_3. The dashed curve in (a) is slope$= -2$, while the dashed curve in (b) corresponds to a function proportional to $e^{-2\chi_1 N}$.

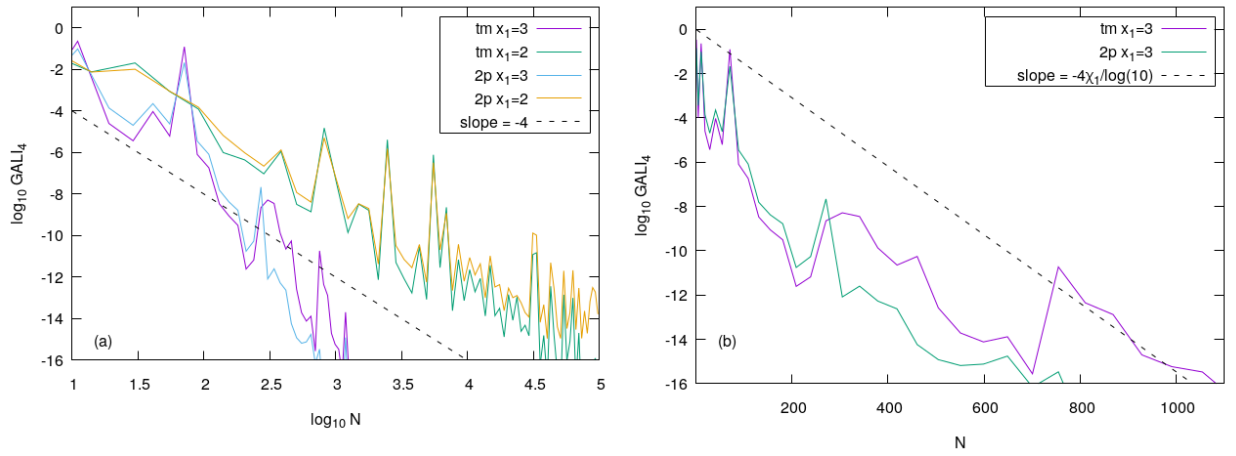

Figure 2.21: Same as Figure 2.18, but for GALI_4. The dashed curve in (a) is slope$= -4$, while the dashed curve in (b) corresponds to a function proportional to $e^{-4\chi_1 N}$.

3. Chaotic Dynamics of Magnetic Field Lines

In order to study the chaotic dynamics of turbulent plasmas in fusion devices, it is crucial to understand the behaviour of chaotic magnetic fields. This cannot be achieved without an understanding of the topological configuration of fusion devices. Although fusion devices possess toroidal configuration in order to prevent end losses of extremely hot plasma particles and energy, magnetic coils wound round these devices provide magnetic fields which are used to confine plasma in a bounded area. However, since particles predominantly follow magnetic field lines, an understanding of field line structures are important for plasma confinement.

3.1 Magnetic Field Representation

Coordinates defined by the magnetic field are used to describe toroidal magnetic configuration of fusion devices because they simplify the field description and provide a general theory for the study of all toroidal fusion devices. Due to the essential toroidal configuration of the magnetic field, these coordinates are taken to be in toroidal form (Figure 3.1). Surfaces of constant ψ are taken to topologically consist of nested tori with axis given by $\psi = 0$. Also, surfaces of constant θ define a poloidal surface and surfaces of constant ζ defines a toroidal surface (Figure 3.2) (White, 2013).

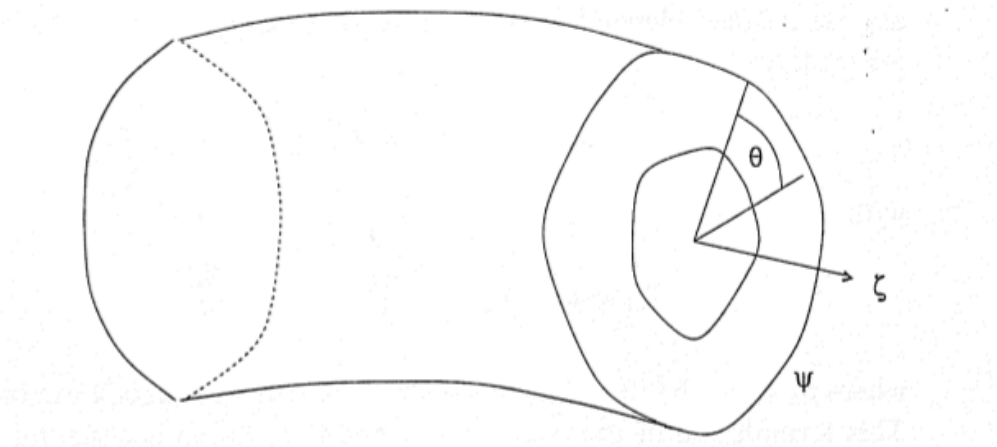

Figure 3.1: General toroidal coordinates: ψ, θ and ζ are the magnetic surface, the poloidal angle and the toroidal direction, respectively. Image taken from (White, 2013).

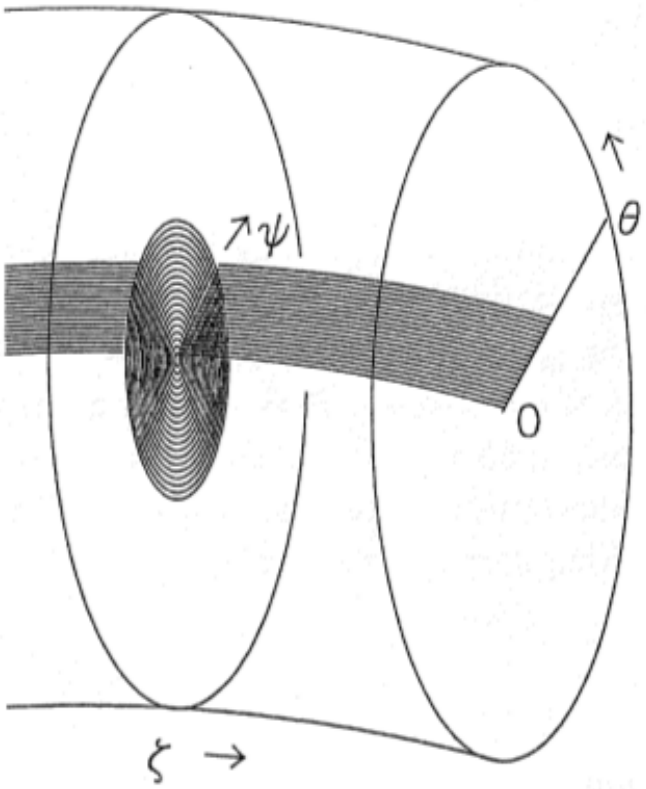

Figure 3.2: Poloidal surface (fixed θ) and toroidal surface (fixed ζ). Image taken from (White, 2013).

Following (White, 2013) we proceed to show that magnetic field line trajectories are Hamiltonian in nature.

Firstly, let $\vec{B}$ be the magnetic field. Since $\nabla \cdot \vec{B} = 0$ (Poincaré, 1892), we write $\vec{B} = \nabla \times \vec{A}$ with the position vector $\vec{r}(\rho, \theta, \zeta)$. The vector potential $\vec{A}$ can be written as a linear combination of the contravariant basis[1] in the form

$$\vec{A} = A_\rho \nabla\rho + A_\theta \nabla\theta + A_\zeta \nabla\zeta. \tag{3.1.1}$$

We consider a function G such that $\partial_\rho G = A_\rho$, since $\nabla G = \partial_\rho G \nabla\rho + \partial_\theta G \nabla\theta + \partial_\zeta G \nabla\zeta$. Then we obtain

$$\vec{A} = \nabla G + A_\theta \nabla\theta + A_\zeta \nabla\theta - \partial_\theta G \nabla\theta - \partial_\zeta G \nabla\zeta = \nabla G + (A_\theta - \partial_\theta G)\nabla\theta + (A_\zeta - \partial_\zeta G)\nabla\zeta.$$

Let

$$\psi = A_\theta - \partial_\theta G, \quad \psi_p = -A_\zeta + \partial_\zeta G,$$

[1] Given the general coordinates $\vec{r}(\psi, \theta, \zeta)$ we define a covariant basis

$$\vec{e}_\psi = \partial_\psi \vec{r}, \quad \vec{e}_\theta = \partial_\theta \vec{r}, \quad \vec{e}_\zeta = \partial_\zeta \vec{r}.$$

Also, we define a contravariant basis

$$\vec{e}^{\psi} = \nabla\psi, \quad \vec{e}^{\theta} = \nabla\theta, \quad \vec{e}^{\zeta} = \nabla\zeta.$$

so

$$\vec{A} \equiv \nabla G + \psi \nabla\theta - \psi_p \nabla\zeta. \tag{3.1.2}$$

It follows that

$$\begin{aligned}
\vec{B} &= \nabla \times (\nabla G + \psi\nabla\theta - \psi_p\nabla\zeta) \\
&= \nabla \times (\nabla G) + \nabla \times (\psi\nabla\theta) - \nabla \times (\psi_p \nabla G) \\
&= \nabla\psi \times \nabla\theta + \psi(\nabla \times \nabla\theta) - \psi_p(\nabla \times \nabla\zeta) - \nabla\psi_p \times \nabla\zeta \\
&= \nabla\psi \times \nabla\theta - \nabla\psi_p \times \nabla\zeta.
\end{aligned}$$

Thus

$$\vec{B} = \nabla\psi \times \nabla\theta - \nabla\psi_p \times \nabla\zeta. \tag{3.1.3}$$

Subsequently, magnetic field lines are defined by

$$\frac{d\psi}{d\zeta} = \frac{\vec{B}\cdot\nabla\psi}{\vec{B}\cdot\nabla\zeta}, \quad \frac{d\theta}{d\zeta} = \frac{\vec{B}\cdot\nabla\theta}{\vec{B}\cdot\nabla\zeta}, \tag{3.1.4}$$

which can be written as

$$\frac{d\psi}{d\zeta} = -\frac{\nabla\psi\cdot(\nabla\psi_p\times\nabla\zeta)}{(\nabla\psi\times\nabla\theta)\cdot\nabla\zeta}, \quad \frac{d\theta}{d\zeta} = -\frac{\nabla\theta\cdot(\nabla\psi_p\times\nabla\zeta)}{(\nabla\psi\times\nabla\theta)\cdot\nabla\zeta}.$$

But, given that

$$\nabla\psi_p = \partial_\psi\psi_p\nabla\psi + \partial_\theta\psi_p\nabla\theta + \partial_\zeta\psi_p\nabla\zeta,$$

it follows that

$$\begin{aligned}
\frac{d\psi}{d\zeta} &= -\frac{\nabla\psi\cdot((\partial_\psi\psi_p\nabla\psi)\times\nabla\zeta + (\partial_\theta\psi_p\nabla\theta)\times\nabla\zeta)}{(\nabla\psi\times\nabla\theta)\cdot\nabla\zeta} \\
&= -\frac{\nabla\psi\cdot((\partial_\theta\psi_p\nabla\theta)\times\nabla\zeta)}{(\nabla\psi\times\nabla\theta)\cdot\nabla\zeta} \\
&= -\partial_\theta\psi_p
\end{aligned}$$

and

$$\begin{aligned}
\frac{d\theta}{d\zeta} &= -\frac{\nabla\theta\cdot((\partial_\psi\psi_p\nabla\psi)\times\nabla\zeta + (\partial_\theta\psi_p\nabla\theta)\times\nabla\zeta)}{(\nabla\psi\times\nabla\theta)\cdot\nabla\zeta} \\
&= -\frac{\nabla\theta\cdot((\partial_\psi\psi_p\nabla\psi)\times\nabla\zeta)}{(\nabla\psi\times\nabla\theta)\cdot\nabla\zeta} \\
&= \frac{\nabla\theta\cdot(\nabla\zeta\times(\partial_\psi\psi_p\nabla\psi))}{(\nabla\psi\times\nabla\theta)\cdot\nabla\zeta} \\
&= \partial_\psi\psi_p.
\end{aligned}$$

Thus,

$$\frac{d\psi}{d\zeta} = -\partial_\theta\psi_p, \quad \frac{\partial\theta}{\partial\zeta} = \partial_\psi\psi_p \tag{3.1.5}$$

are the field line equations of the one-and-half dimensional time-dependent, continuous dynamical system of the Hamiltonian $\psi_p(\psi,\theta,\zeta)$, with ψ as momentum, θ as general coordinate and ζ as time. The Hamiltonian is 2π periodic in space and time.

3.2 Magnetic Surface Destruction

Let $g(\vec{r}) = constant$ be a two-dimensional surface. The surface g is said to be a magnetic surface if at any point on g the magnetic field lines lie within g, i.e., $\vec{B} \cdot \nabla g = 0$. The existence of magnetic surfaces in magnetic confinement devices is an essential requirement for the long-term confinement of plasma. These surfaces have been shown to exist only when there exists symmetry or approximate symmetry in the configuration (Morozov and Solov'Ev, 1966). According to Kolmogorov (1954), a small perturbation of a symmetric configuration leaves well defined magnetic surfaces everywhere, except for a small volume proportional to the square root of the perturbation where magnetic islands exist. An increase in the perturbation increases island width, thus enhancing the destruction of magnetic surfaces, and the surviving toroidal magnetic surface is a Kolmogorov, Arnold and Moser (KAM) surface. On this note, it is not surprising that the existence of KAM surfaces is extremely important for plasma confinement because field lines do not move across them due to the divergent-free nature of the magnetic field, thus they prevent the magnetic field from wandering in ψ.

Using the representation of $\vec{B}$ in (3.1.3) to form

$$\vec{B} \cdot \nabla \psi_p = (\nabla \psi \times \nabla \theta) \cdot \nabla \psi_p, \tag{3.2.1}$$

$$\vec{B} \cdot \nabla \psi = (\nabla \zeta \times \nabla \psi_p) \cdot \nabla \psi \tag{3.2.2}$$

we can see that ψ_p is a magnetic surface if ψ_p is independent of ζ, and ψ is a magnetic surface if ψ_p is independent of θ. We can deduce that, if ψ_p is independent of both θ and ζ i.e., $\psi_p = \psi_p(\psi)$, then ψ_p and ψ are magnetic surfaces. The easiest way to guarantee the existence of the required approximated magnetic surfaces in the system where $\psi_p = \psi_p(\psi)$ is to simply take a small perturbation of the system to be the confinement device.

As mentioned earlier, the presence of perturbations leads to the destruction of toroidal magnetic surfaces. Although the Hamiltonian formulation described earlier has been used extensively to study the destruction of magnetic surfaces in tokamaks and stellarators due to magnetic perturbations (Kerst, 1962; Freis et al., 1973; Matsuda and Yoshikawa, 1975; Abdullaev et al., 1998; Wingen et al., 2005; Abdullaev et al., 2008; Abdullaev, 2009, 2014), we shall attempt to illustrate it. To describe how nested toroidal magnetic surfaces are destroyed we consider a magnetic field in a toroidal system in the presence of nonaxisymmetric (i.e. dependence on the toroidal direction ζ) magnetic perturbations. For the efficient and accurate analysis of the evolution of magnetic field lines we employ the use of the PSS. Further, we will quantify the chaoticity of chaotic field lines using the mLCE and the SALI methods.

Since the Hamiltonian $\psi_p(\psi, \theta, \zeta)$ discussed in Sect 3.1 is time-dependent (i.e., ζ dependent), we create the PSS in a stroboscopic way. This involves creating a poloidal cross-section $\zeta = 0$ and integrating field line equations until a specific value of ζ which corresponds to one toroidal turn. This indicates an intercession of the magnetic field line with the section in a particular direction. We then proceed to find the point of intersection. A computer code for creating the Poincaré map is presented in pseudo-code in Algorithm 2.

In our study we will consider two simple models of the tokamak which describe the topology of magnetic

field lines in tokamak fields in the presence of nonaxisymmetric perturbations.

Input Data: initial condition for the magnetic field line $\mathbf{x}(0 = \mathbf{x}(\theta(0), \psi(0))$, PSS value ζ_{pss}, strobe period sp, integration time step τ, equations (3.1.5) and maximal integration time T_{max}
Output : intersections with surface of section

set the counter, $k = 1$;
set $tcross = sp$;
while $k\tau < T_{max}$ **do**
  evolve the field line from time $t = (k-1)\tau$ to $t = k\tau$ i.e. compute $\mathbf{x}(k\tau)$ using an appropriate numerical scheme;
  if $k\tau > tcross$ **then**
    set integration time step $\lambda = k\tau - tcross$;
    set the initial conditions $\mathbf{y}(0) := \mathbf{x}(k\tau)$;
    integrate (3.1.5) with $\mathbf{y}(0)$ for one time step using an appropriate numerical scheme;
    store $\mathbf{y}(\lambda)$
  end
  set $tcross = tcross + sp$;
  set the counter, $k = k + 1$;
end

Algorithm 2: Algorithm for the numerical computation of Poincaré maps of magnetic field lines. The program numerically integrates the equations of magnetic field lines up to a given maximal integration time $t = T_{max}$, detects and computes its intersections with a surface of section of the form $\zeta_{pss} = 0$.

3.3 Model 1: A toy model

We illustrate the destruction of nested toroidal magnetic surfaces due to nonaxisymmetric perturbations, using the poloidal flux function defined by White (2013) as

$$\psi_p = \int \frac{d\psi}{q(\psi)} + V\cos(n\zeta - m\theta), \tag{3.3.1}$$

where $\int \frac{d\psi}{q}$ is the unpertubed Hamiltonian and $V\cos(n\zeta - m\theta)$ is the nonaxisymmetric perturbation, with V denoting the relative strength of the perturbation. The function $q(\psi)$ is the so-called safety factor and is the ratio of the number of toroidal turns to one poloidal turn. From (3.1.5), field line equations are

$$\frac{d\psi}{d\zeta} = -V\sin(n\zeta - m\theta), \quad \frac{d\theta}{d\zeta} = \frac{1}{q(\psi)}. \tag{3.3.2}$$

We introduce the variable $Q = n\zeta - m\theta$ and expand $q(\psi)$ about ψ_0, with $q(\psi_0) = \frac{m}{n}$, where $q' = dq/d\psi$ evaluated at ψ_0. This expansion gives

$$q(\psi) \simeq q(\psi_0) + q'(\psi_0)(\psi - \psi_0), \tag{3.3.3}$$

we then find

$$\frac{dQ}{d\zeta} = \frac{mq'(\psi_0)(\psi - \psi_0)}{q^2}, \quad \frac{d\psi}{d\zeta} = -mV\sin(Q). \tag{3.3.4}$$

3.3.1 Numerical Investigation. We choose $q(\psi) = \frac{2}{2-\psi}$, $V = 0.01$, $n = 2$, $m = 3$, $\psi_0 = 0$ and an integration time step $\tau = 0.01$.

As can be seen in Figure 3.3, due to the integrability of (3.3.4), the PSS consists of smooth curves of nested toroidal magnetic surfaces R and island chains O. The figure depicts broken flux surfaces due to island chains, as not all field lines are toroidal. Moreover, the topologically toroidal surfaces are separated from the island chain by an exactly defined separatrix (denoted by X). In other words, the separatrix separates oscillating trajectories (denoted by O) from rotating trajectories (denoted by R). Although these curves are regular orbits, these island chains are detrimental to plasma confinement as they lead to increased transport of particles and energy to the walls of the fusion device. This is because in a magnetic island, particles can easily and quickly move through the full island width by following field lines. For instance, a particle at $\psi = -0.25, Q = 6$ can easily move along field lines to $\psi = 0.25, Q = 6$. Nevertheless, it is difficult for particles in well-defined toroidal surfaces to move to the plasma edge as they need to collide with many particles and jump from one surface to another in a random walk-like diffusion process.

In Figure 3.4, the quantitative behaviour of the orbits are presented using the mLCE. It is important to note that orbits in Figure 3.4 correspond to the first island chain located at the interval $\psi \in [-0.35, 0.35]$ in Figure 3.3, with corresponding colours. We can see that the orbits are regular as χ tends to zero for all orbits and are in good agreement with the qualitative behaviour of orbits in Figure 3.3.

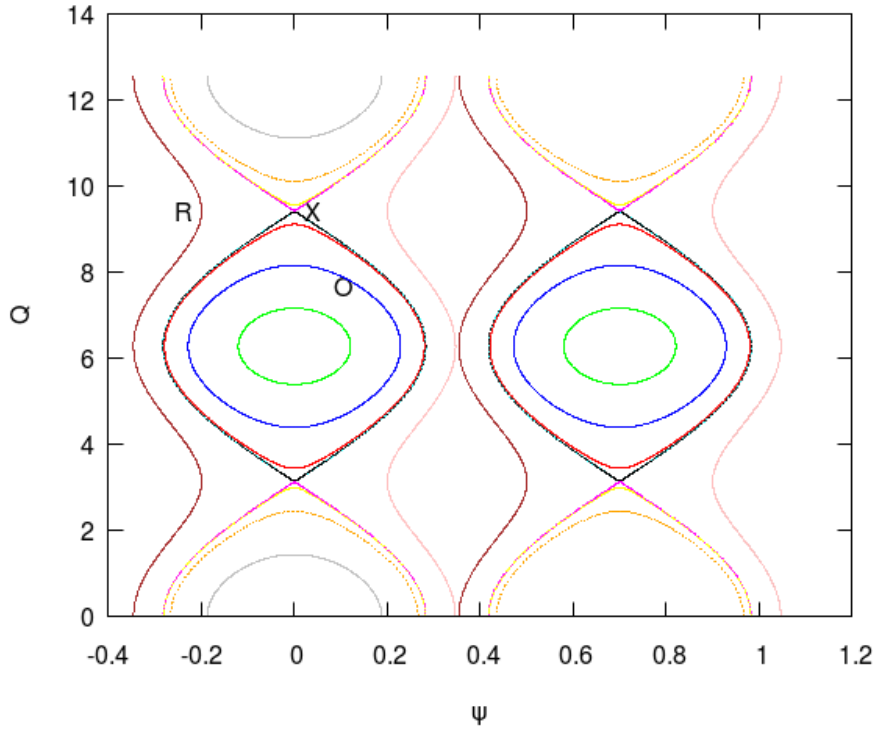

Figure 3.3: The PSS of system (3.3.1) at $\zeta = 0$, with $V = 0.01$. Several initial conditions having a fixed ψ value were considered, with $\psi = 0$ and $\psi = 0.7$, for the first ($\psi \in [-0.35, 0.35]$) and second island chains ($\psi \in [0.35, 1.05]$), respectively. The separatrix is denoted by X, the oscillating trajectory (denoted by O) represents an island, while the rotating trajectory (denoted by R) represents a toroidal field line.

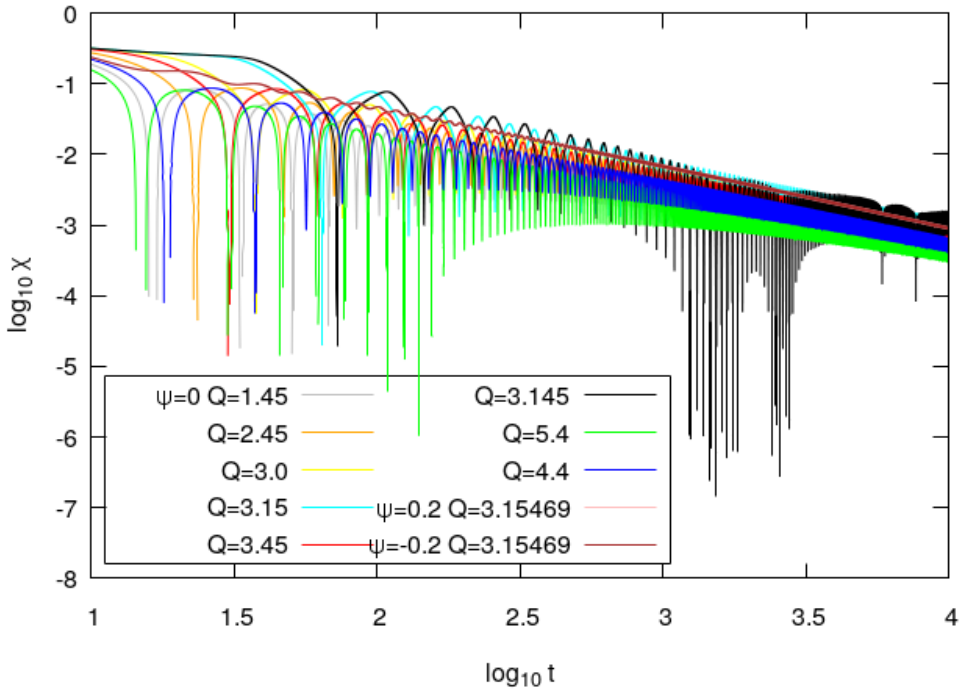

Figure 3.4: Evolution of the mLCE χ against time for orbits of the system (3.3.1), with $V = 0.01$. The curves correspond to orbits of the the first island chain in Figure 3.3 . Both axes are in logarithmic scale.

Now, suppose the Hamiltonian (3.3.1) is additionally perturbed to give

$$\psi_p = \int \frac{d\psi}{q(\psi)} + V\cos Q - \varepsilon\cos(Q - \zeta - \zeta_0), \tag{3.3.5}$$

where ε denotes the relative strength of the additional perturbation and ζ_0 the phase. The magnetic field lines are now defined by

$$\begin{aligned} \frac{\partial\psi}{\partial\zeta} &= -mV\sin Q + m\varepsilon\sin(Q - \zeta - \zeta_0), \\ \frac{\partial Q}{\partial\zeta} &= \frac{mq'(\psi_0)(\psi - \psi_0)}{q^2}. \end{aligned} \tag{3.3.6}$$

We choose $V = 0.01$, $n = 2$, $m = 3$, $\psi_0 = 0.0$, $q = \frac{2}{2-\psi}$, and $\tau = 0.01$.

In Figure 3.5 we present the PSS of system (3.3.5) at $\zeta = 0$, with $\varepsilon = 0.0001$. We can see that with the additional perturbation there is a small region of chaotic trajectories near the separatrix. This chaotic behaviour near the separatrix is expected, as this region is sensitive to initial conditions due to the presence of unstable periodic orbits. As was done for the case of the integrable system, Figure 3.6 depicts the mLCE of orbits corresponding to the first island chain in Figure 3.5. Also, the chaotic nature of orbits (cyan, magenta and black curves) located near the separatrix are depicted in the figure as they have positive LCEs.

A further increase in the perturbation of (3.3.5) to $\varepsilon = 0.001$ yields the result of Figure 3.7. There we see that the increase of ε increases the chaotic region near the separatrix increases, which allows fast transport of particles. In support of the aforementioned result, Figure 3.8 shows an increased number of chaotic orbits as the perturbation strength ε becomes larger. In particular, orbits corresponding to the yellow, orange magenta, cyan, black and red curves are chaotic, while orbits corresponding to the grey, blue, green, pink and brown curves are regular Thus, we conclude that the perturbation strength controls the chaoticity of the system.

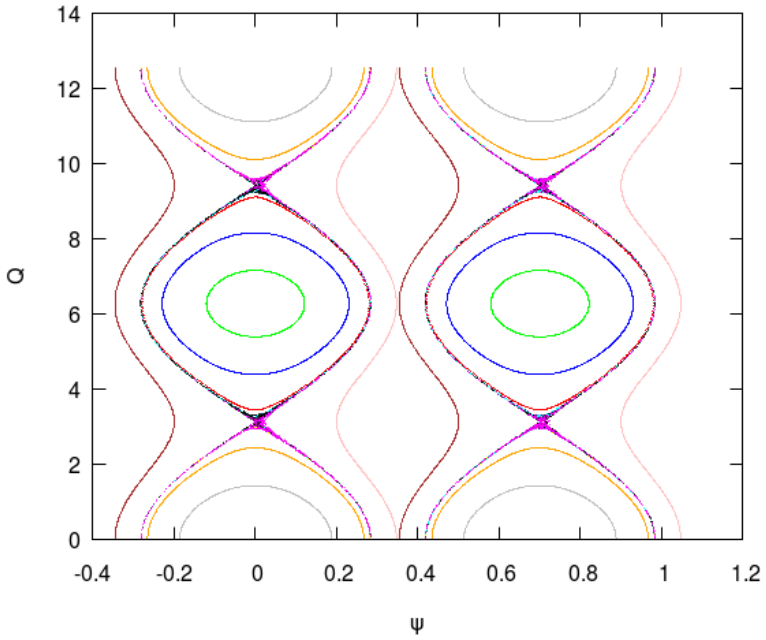

Figure 3.5: Same as Figure 3.3, but for $\varepsilon = 0.0001$.

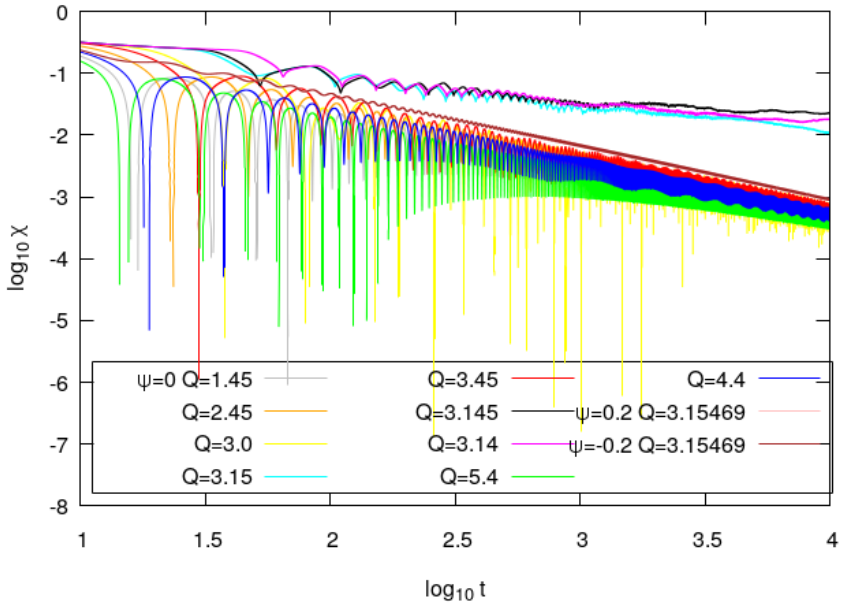

Figure 3.6: Same as Figure 3.4, but for $\varepsilon = 0.0001$.

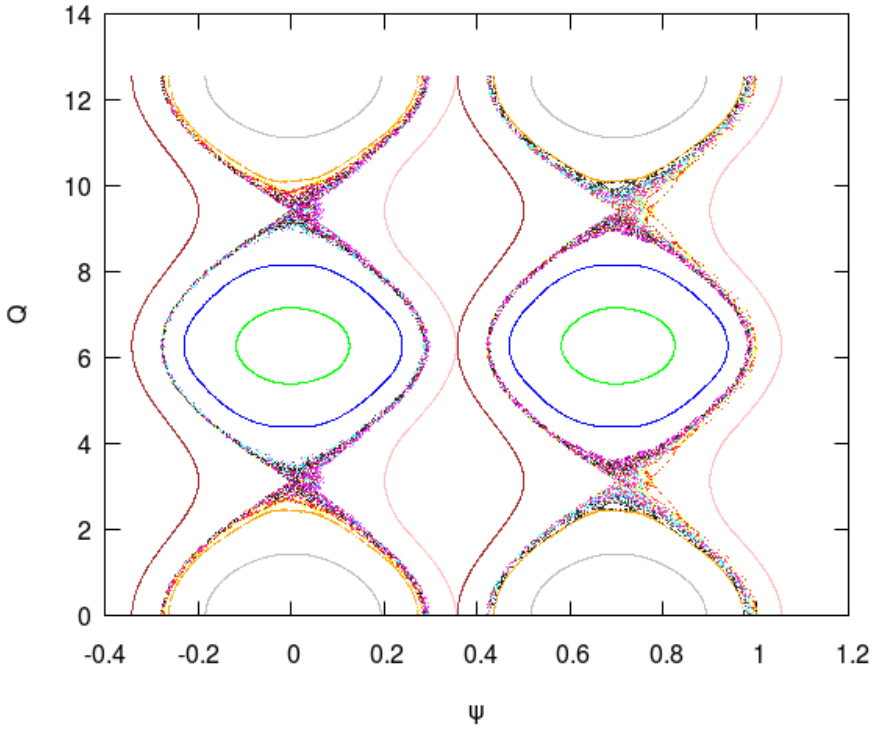

Figure 3.7: Same as Figure 3.3, but for $\varepsilon = 0.001$.

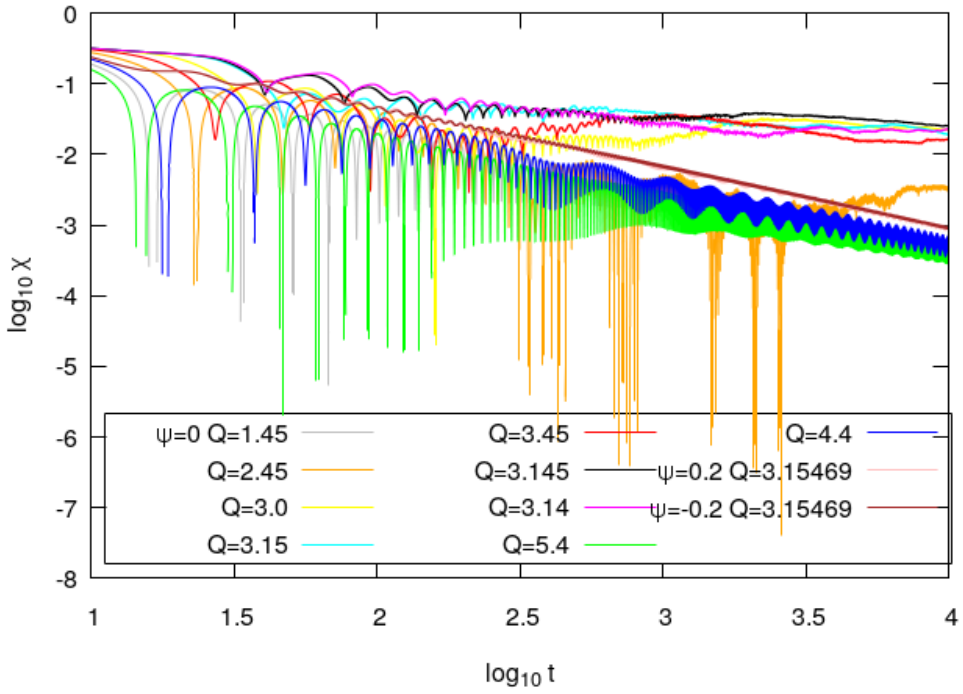

Figure 3.8: Same as Figure 3.4, but for $\varepsilon = 0.001$.

3.4 Model 2: The Symmetric Tokamap

Numerous analytical mapping methods have been proposed for the replacement of a continuous Hamiltonian system by a discrete iterative map for the fast and accurate numerical integration of magnetic field line equations (Abdullaev et al., 1998; Balescu et al., 1998; Ali et al., 2004; Punjabi et al., 1994). These discrete iterative maps are required to be flux-preserving, possess the same fixed points as the Poincaré map, along with the same chaotic and regular regions of the original continuous system, and should be compatible with the toroidal geometry of the continuous system. Here we consider the so-called tokamap model (Balescu et al., 1998; Misguich, 2001; Misguich et al., 2002) used to describe the global behaviour of magnetic field lines in tokamaks. The tokamap was constructed by Balescu et al. (1998) and they claimed that it is a representation of the Poincaré map of a continuous magnetic field line system. Unfortunately, it was later shown that the claim is false, as the tokamap does not possess time-reversal symmetry. Eventually, this led to the introduction of the symmetric tokamap by Abdullaev (2004) which is based on a continuous Hamiltonian system consisting of an integrable part given by the safety factor and a non-integrable perturbation. The symmetric tokamap is time-reversible and is a very good representation of the Poincaré map of the continuous system in contrast to the tokamap.

Consider the Hamiltonian defined by Wingen et al. (2005) as

$$H = \int \frac{d\psi}{q(\psi)} + \varepsilon \frac{\psi}{1+\psi} \cos(\theta) \sum_{s=-M}^{M} \cos(s\zeta). \tag{3.4.1}$$

For efficient and accurate integration, the system's field line equations are transformed into the following

implicit mapping:

$$\bar{\psi}_k = \psi_k - \frac{\varepsilon}{2}\frac{\bar{\psi}_k}{1+\bar{\psi}_k}\sin(\theta_k), \qquad \bar{\theta}_k = \theta_k - \frac{\varepsilon}{2}\frac{1}{(1+\bar{\psi}_k)^2}\cos(\theta_k), \tag{3.4.2}$$

$$\bar{\theta}_{k+1} = \bar{\theta}_k + \frac{2\pi}{q(\bar{\psi}_k)},$$

$$\psi_{k+1} = \bar{\psi}_k - \frac{\varepsilon}{2}\frac{\bar{\psi}_k}{1+\bar{\psi}_k}\sin(\theta_{k+1}), \qquad \theta_{k+1} = \bar{\theta}_{k+1} - \frac{\varepsilon}{2}\frac{1}{(1+\bar{\psi}_k)^2}\cos(\theta_{k+1}).$$

Resolving the implicit equation for $\bar{\psi}_k$ explicitly with respect to $\bar{\psi}_k$ yields

$$\bar{\psi}_k = \frac{1}{2}\left[\sqrt{(P^2(\psi_k,\theta_k)+4\psi_k} - P(\psi_k,\theta_k)\right], \tag{3.4.3}$$

where

$$P(\psi_k,\theta_k) = 1 - \psi_k + \frac{\varepsilon}{2}\sin(\theta_k). \tag{3.4.4}$$

The implicit equation for θ_{k+1} cannot be solved explicitly, but an approximation can be done using numerical methods for solving algebraic equations, such as the Newton method, with $\bar{\theta}_{k+1}$ used as the initial guess for the approximation. We take

$$q(\psi) = \frac{4}{(2-\psi)(2-2\psi+\psi^2)}.$$

In addition, in polar coordinates, i.e., in the X, Z polar plane we have that $X = \psi\cos\theta$ and $Z = \psi\sin\theta$. A computer code for creating a PSS using the symmetric tokamap is presented in pseudo-code in Algorithm 3.

3.4.1 Numerical Investigation. In order to numerically investigate the chaotic dynamics of the symmetric tokamap we employ the PSS method, the mLCE and SALI methods. However, the implicit nature of the symmetric tokamap leads to great difficulty and complexity in obtaining its tangent map. Hence, we use the evolution of nearby orbits for the computation of quantitative chaos indicators, since their equivalence to the tangent map method for the aforementioned purpose has been established in Chapter 2.

The PSS

The creation of the PSS in Figures 3.9 and 3.10 was done by the evolution of 50 orbits with ψ being uniformly distributed in the interval $[0, 1.7]$ and $\theta = 0.5$. However, for the PSS in Figures 3.11 – 3.17 400 orbits were evolved on a grid of 20×20 with ψ and θ being uniformly distributed in the intervals $[0, 1.7]$ and $[0, 2\pi]$, respectively.

Figure 3.9 shows the existence of the essential toroidal flux surfaces for plasma confinement. Here, flux surfaces are not broken. This is due to the insignificant effect of a very small value of the relative perturbation strength $\varepsilon = \frac{0.5}{2\pi}$. But it is not the case in Figure 3.10, as flux surfaces are broken due to the formation of island chains around $\psi \approx 0.45, 0.8, 1.1$ in Figure 3.10(a), as a result of an increase

Input Data: initial condition for the magnetic field line $\mathbf{x}_0 = \mathbf{x}(\theta_0, \psi_0)$, 2-dimensional zero vectors **xin** and **xout**, PSS value ζ_{pss}, maximum number of iterations its, error tolerance ε and maximal steps K_{max}

Output : intersections with surface of section

set the counter, $k = 0$;
while $k \leq K_{max}$ **do**
  set **xin** $=$ $\mathbf{x}_k$;
  evolve the field line from time t_k to t_{k+1} i.e. compute $\mathbf{x}_{k+1}$ using the symmetric tokamap (3.4.2);
  $\bar{\psi}_k$;
  $xout_1 = xin_1$;
  $xout_2 = \frac{1}{2}\left[\sqrt{P^2(xin) + 4xin_2} - P(xin)\right]$;
  set **xin** $=$ **xout**;
  $\bar{\theta}_k$;
  $xout_1 = xin_1 - \frac{\varepsilon}{2}\frac{1}{(1+xin_2)^2}\cos(xin_1)$;
  $xout_2 = xin_2$;
  set **xin** $=$ **xout**;
  $\bar{\theta}_{k+1}$;
  $xout_1 = xin_1 + \frac{2\pi}{q(xin_2)}$;
  $xout_2 = xin_2$;
  set **xin** $=$ **xout**;
  θ_{k+1};
  set $converged = 0$ and $i = 0$;
  set $tin = xin_1 - \frac{\varepsilon}{2}\frac{1}{(1+xin_2)^2}\cos(xin_1)$;
  $f = tin - xin_1 + \frac{\varepsilon}{2}\frac{1}{(1+xin_2)^2}\cos(tin)$;
  $f' = 1 - \frac{\varepsilon}{2}\frac{1}{(1+xin_2)^2}\sin(tin)$;
  while $converged = 0$ *and* $i \leq imax$ **do**
    $tin = tin - \frac{f}{f'}$;
    if $abs(f) \leq \varepsilon$ **then**
      set $converged = 1$;
    end
    $i = i + 1$;
  end
  $xout_1 = tin$;
  $xout_2 = xin_2$;
  set **xin** $=$ **xout**;
  ψ_{k+1};
  $xout_1 = xin_1$;
  $xout_2 = xin_2 - \frac{\varepsilon}{2}\frac{xin_2}{1+xin_2}\sin(xin_1)$;
  set $\mathbf{x}_{k+1}$ $=$ **xout**;
  set the counter, $k = k + 1$;
end

Algorithm 3: Algorithm for the numerical computation of the Poincaré plot of a symmetric tokamap. The program numerically integrates the equations of magnetic field lines for a given maximal step $k = K_{max}$, computes its intersections with a surface of section of the form $\zeta_{pss} = 0$.

in the relative perturbation strength to $\varepsilon = \frac{1.5}{2\pi}$. A subsequent increase in $\varepsilon = \frac{2.55}{2\pi}$ leads to further breakage of flux surfaces, as the formation of more and larger island chains are visible (Figure 3.11).

A further increase of the perturbation strength $\varepsilon = \frac{3.5}{2\pi}$ yields the onset of chaos near the separatrix at $\psi \approx 0.5$ and $\theta \approx 1.5, 4.7$, the formation of several island chains, and the existence of symmetry in θ, as shown in Figure 3.12. An increase in $\varepsilon = \frac{4.5}{2\pi}$ results in the formation of a chaotic sea comprising several new tiny islands of stability, as shown (Figure 3.13), while the plasma core around $\psi \approx 0.1, \theta \approx \pi$ is not destroyed. In the same vein, a further increase to $\varepsilon = \frac{5}{2\pi}$ leads to the growth of the chaotic sea in the phase space of the system and the formation of several new, tiny islands (Figure 3.14).

The onset of the destruction of KAM surfaces at the upper part of the PSS and the growth of the chaotic sea comprising islands of stability, visible in Figure 3.15 is as a result of the increase of the perturbation strength to $\varepsilon = \frac{6}{2\pi}$, although the plasma core still remains intact. Similar results are obtained in Figure 3.16 for $\varepsilon = \frac{6.5}{2\pi}$. Finally, the entire destruction of flux surfaces but for a very small section of the plasma core for $\varepsilon = \frac{9}{2\pi}$ is shown in Figure 3.16. This condition of magnetic field lines is not suitable for plasma confinement as large excursion of plasma particles in flux surfaces can neither be avoided nor controlled.

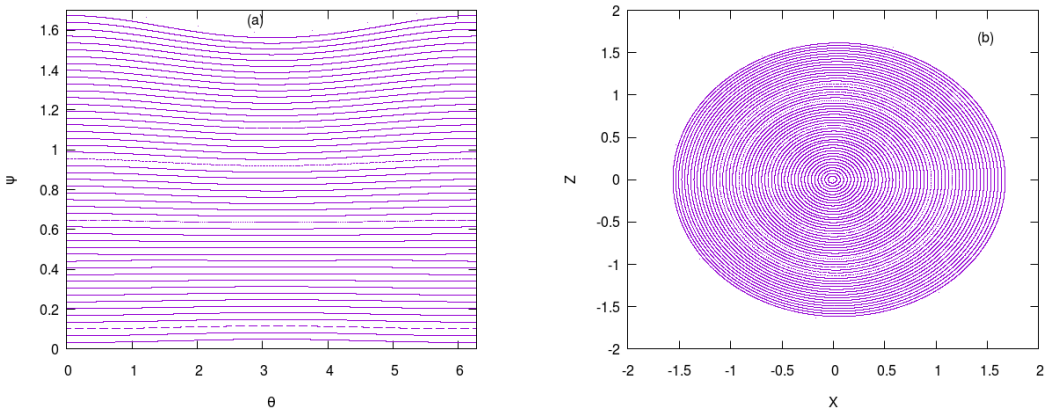

Figure 3.9: The PSS of the symmetric tokamap (3.4.2) for $\zeta = 0$, with $\varepsilon = 0.5/2\pi$ in (a) magnetic coordinates (θ, ψ) and (b) polar coordinates $X = \psi \cos\theta$, $Z = \psi \sin\theta$.

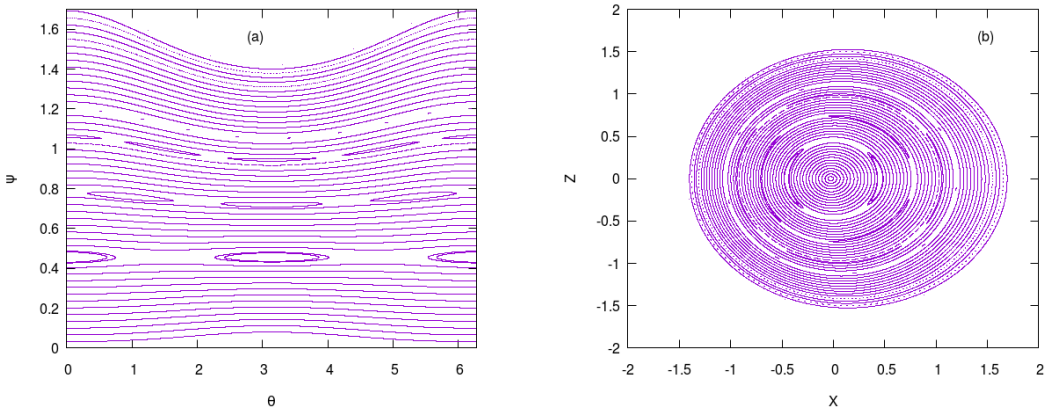

Figure 3.10: Same as Figure 3.9, but for $\varepsilon = 1.5/2\pi$.

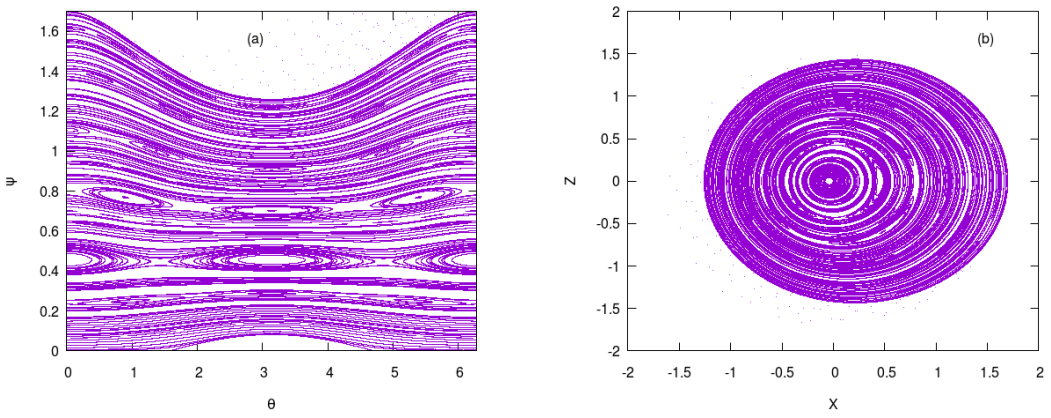

Figure 3.11: Same as Figure 3.9, but for $\varepsilon = 2.55/2\pi$.

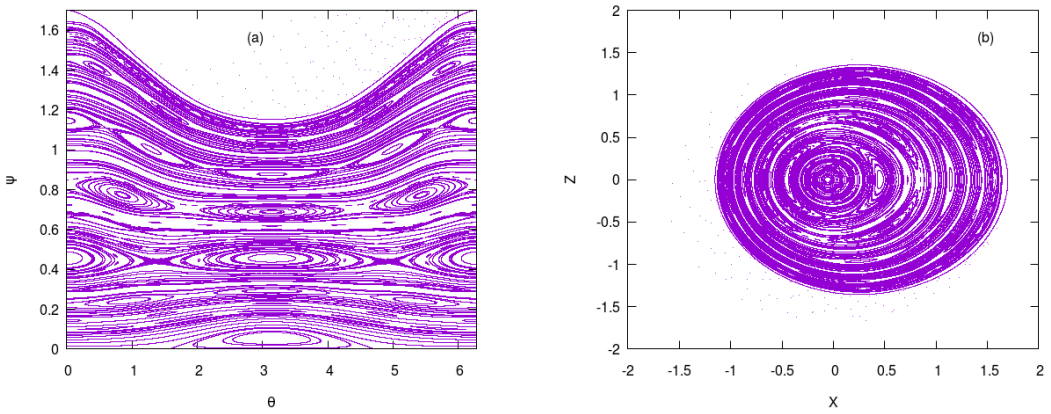

Figure 3.12: Same as Figure 3.9, but for $\varepsilon = 3.5/2\pi$.

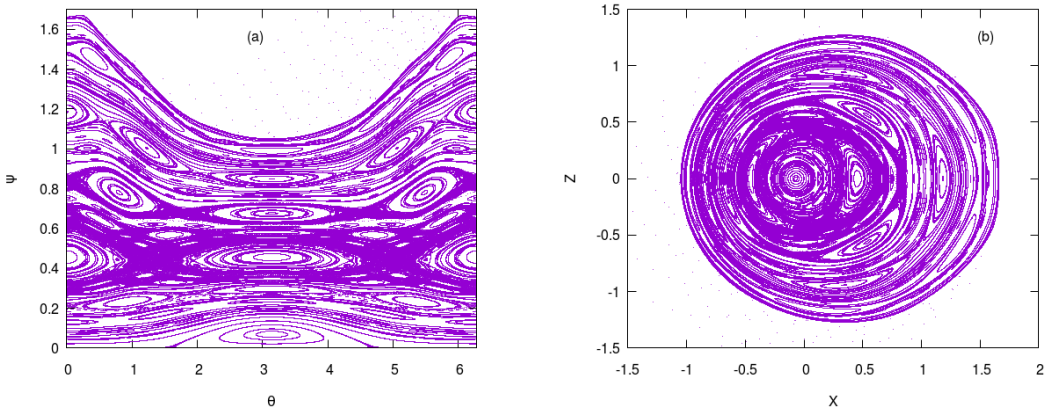

Figure 3.13: Same as Figure 3.9, but for $\varepsilon = 4.5/2\pi$.

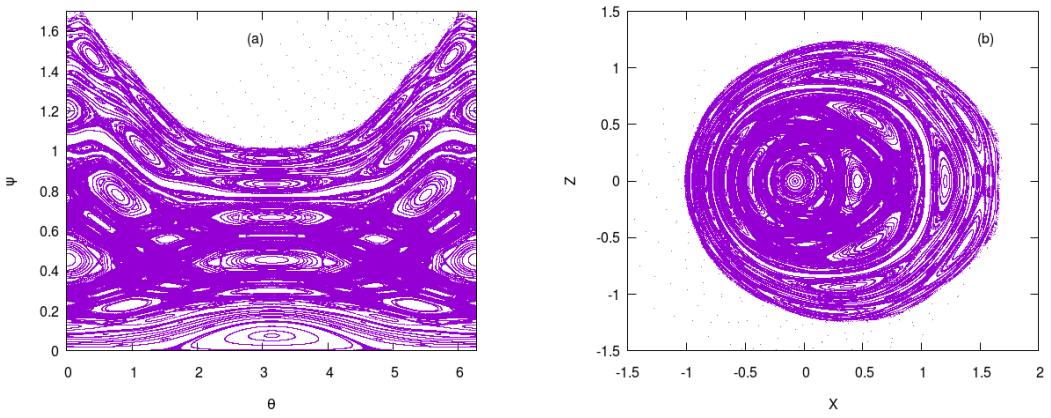

Figure 3.14: Same as Figure 3.9, but for $\varepsilon = 5/2\pi$.

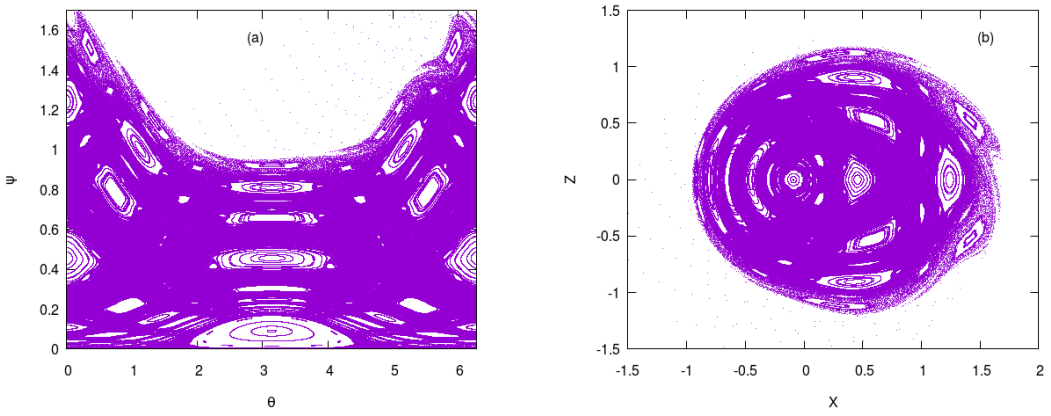

Figure 3.15: Same as Figure 3.9, but for $\varepsilon = 6/2\pi$.

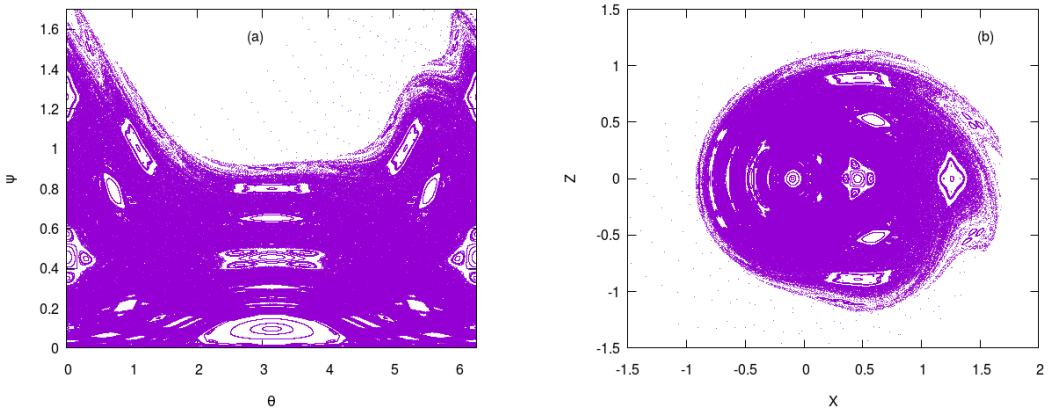

Figure 3.16: Same as Figure 3.9, but for $\varepsilon = 6.5/2\pi$.

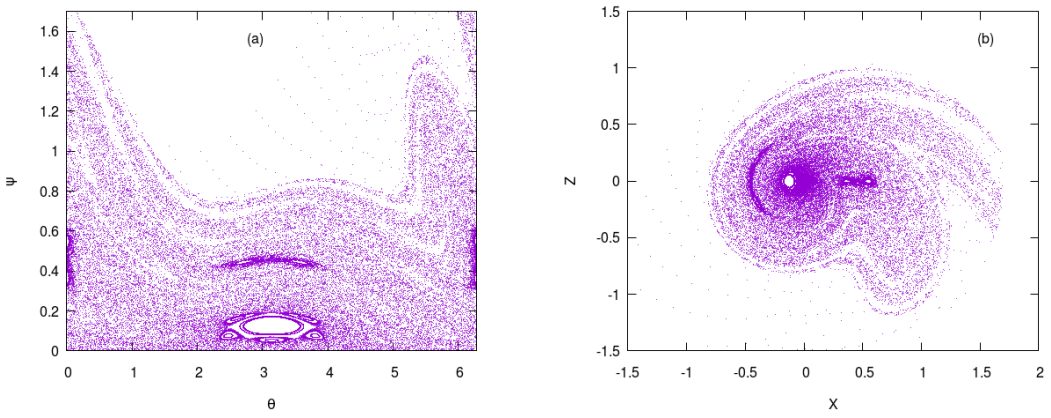

Figure 3.17: Same as Figure 3.9, but for $\varepsilon = 9/2\pi$.

The mLCE of orbits of the symmetric tokamap

In order to quantify the chaoticity of magnetic field lines of the symmetric tokamap we compute the mLCE χ, using the evolution of nearby orbits method. In order to illustrate the behaviour of the mLCE we consider the case of $\varepsilon = 4.5/2\pi$ shown in Figure 3.13. The mLCE of chaotic orbits tends to a constant positive value in Figure 3.18(a) and are represented in the PSSs in Figures 3.18(b) and 3.18(c), with same colours. Further, in Figure 3.19(a) the mLCE of regular orbits tends to zero with slope =-1 and are represented in the PSSs in Figures 3.19(b) and 3.19(c), with same colours. Also, the spectrum of the LCEs shown in Figure 3.20 is in good agreement with theoretical predictions, as $\chi_1 = -\chi_2$ for chaotic (Figure 3.20(a)) and regular (Figure 3.20(b)) orbits, with χ_1 and $-\chi_2$ corresponding to the purple and green curves, respectively.

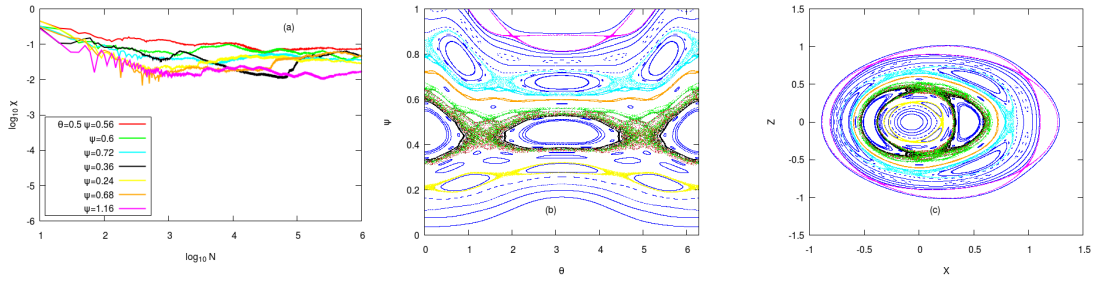

Figure 3.18: The mLCE χ against the number of iterations N of the symmetric tokamap (3.4.2), for chaotic orbits, with $\varepsilon = 4.5/2\pi$ (Both axes are in log scale). The PSS of the symmetric tokamap in (b) magnetic coordinates and (c) polar coordinates, for $\varepsilon = 4.5/2\pi$. Orbits in (a) are shown in corresponding colours in (b) and (c).

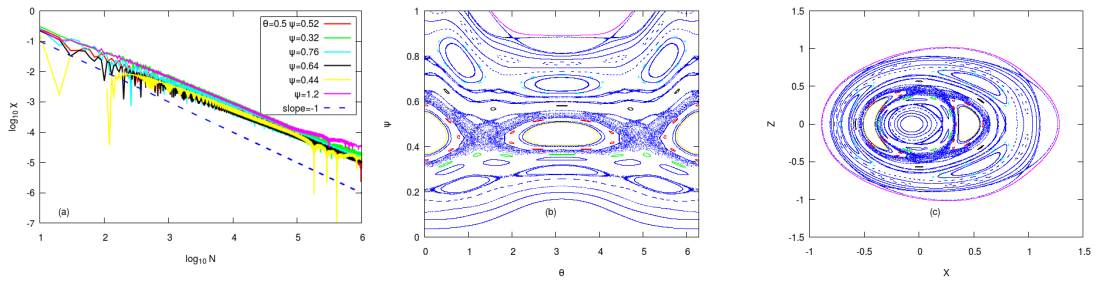

Figure 3.19: The mLCE χ against the number of iterations N of the symmetric tokamap (3.4.2), for regular orbits, with $\varepsilon = 4.5/2\pi$ (Both axes are in log scale). The PSS of the symmetric tokamap in (b) magnetic coordinates and (c) polar coordinates, for $\varepsilon = 4.5/2\pi$. Orbits in (a) are shown in corresponding colours in (b) and (c).

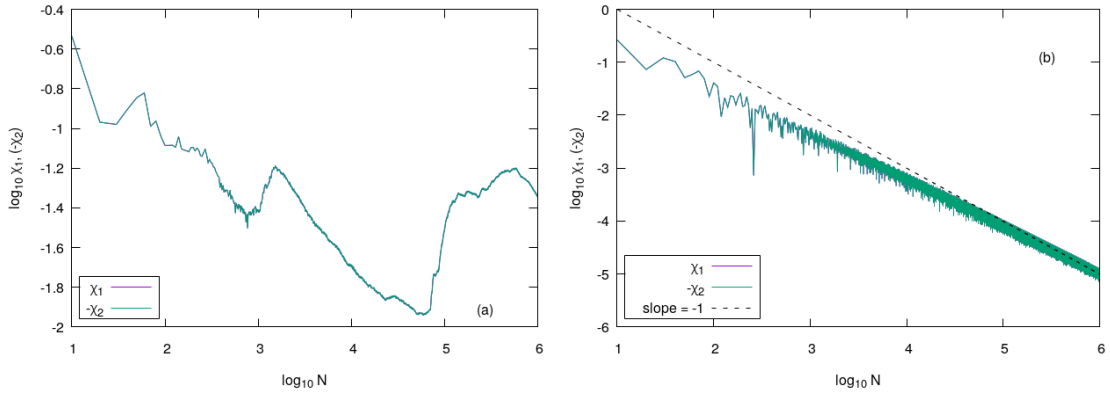

Figure 3.20: Spectrum of the LCEs of (a) chaotic orbit $\theta = 0.5, \psi = 0.36$ and (b) regular orbit $\theta = 0.5, \psi = 0.76$, for $\varepsilon = 4.5/2\pi$.

Scan Map and Percentage of Chaotic Orbits

To qualitatively describe the influence of the perturbation strength on the system's chaoticity we perform extensive studies of the mLCE of several orbits, creating scan maps which are able to depict even tiny regions on the phase space where chaotic or regular motion occurs, something which was not easily done on the PSS. This was achieved by computing the mLCE of several initial conditions on a grid of points, and assigning a different colour to the initial conditions based on the last computed value of the mLCE of each computed initial condition. For the purpose of this analysis we evolve orbits on a grid of 171×171 points, with ψ and θ being uniformly distributed in the intervals $[0, 1.7]$ and $[0, 2\pi]$, respectively for 10^6 iterations. Based on the results obtained in Figures 3.18(a) and 3.19(a) we can confidently take orbits having mLCE values $\chi \geq 10^{-2}$ to be chaotic, while orbits having values of $\chi \leq 10^{-2}$ are considered as regular. In particular, orbits having $\chi \in [10^{-4}, 10^{-2})$ are taken to be sticky orbits, i.e., orbits that are at the borderline of being chaotic.

In Figure 3.21 where the scan map is created for $\varepsilon = \frac{0.5}{2\pi}$, we can see that there are no chaotic orbits as all orbits are regular, corresponding to Figure 3.9, with $\varepsilon = \frac{0.5}{2\pi}$. Similarly, in Figure 3.23 there is

no chaos in the PSS but we can see the emergence of sticky orbits in the region where $\psi = 0.5$ - they surround islands of stability (points are plotted in light blue). This figure corresponds to the PSS of Figure 3.10. As is the case in Figure 3.12, the onset of chaoticity is seen in Figure 3.24 at the separatrix near $\psi = 0.5$ with $\varepsilon = \frac{3.5}{2\pi}$. As expected, subsequent increase of ε to $\frac{4.5}{2\pi}$, and $\frac{5}{2\pi}$ yield chaotic seas in Figures 3.25 and 3.26, similar to Figures 3.13 and 3.14, respectively. In the same vein, increase in ε to $\frac{6}{2\pi}$ and $\frac{6.5}{2\pi}$ results in the destruction of KAM surfaces in the upper part of Figures 3.27 and 3.28. These figures correspond to Figures 3.15 and 3.16, respectively. Finally we can see the total destruction of KAM surfaces, apart from a small region near the plasma core which is coloured in blue in Figure 3.28, with $\varepsilon = \frac{9}{2\pi}$. From these results, we conclude that Scan maps enable us to see tiny regions of stability that are not easily seen on the PSS.

However, knowing the nature of orbits in the phase space is not enough. We would like to quantify the extended chaotic regions of the phase space. Using the mLCE we calculate the percentage of chaotic orbits over the number of studied orbits for several values of the relative perturbation strength. In Figure 3.30(a), we see the result of 10^6 iterations for four different threshold values for the mLCE, which are $10^{-1}, 10^{-2}, 10^{-3}$ and 10^{-4}, with orbits having mLCE value above the threshold classified as chaotic and orbits having mLCE value below the threshold classified as regular. From this figure, we see that when the threshold is 10^{-4} chaos occurs when $\varepsilon = \frac{6.5}{2\pi}$, which does not correspond to our previous analyses. For the case when the threshold is 10^{-1}, chaos appears when $\varepsilon = \frac{2}{2\pi}$, which does not correspond to our previous analyses. However, the threshold values 10^{-2} and 10^{-3} yield quite similar results, with 10^{-2} in good agreement with the results obtained from our previous analyses in Figures 3.21 – 3.29, as chaos occurs when $\varepsilon \gtrsim \frac{3}{2\pi}$. We also observe that for $\varepsilon \gtrsim \frac{10}{2\pi}$ all four cases coincide, as almost all orbits are chaotic. Like wise for $\varepsilon \lesssim \frac{0.75}{2\pi}$, all orbits are regular. In Figure 3.30(b) we present results obtained from the calculation of the percentage of chaotic orbits for the final number of iterations $N = 10^3, 10^4, 10^5, 10^6$ taking orbits with $\chi \gtrsim 10^{-2}$ to be chaotic. We can see that all four distinct number of iterations, yield similar results with 10^6 and 10^5 having no significant difference. Hence, there is not much difference in the percentage of chaotic orbits for different number of iterations.

Moreover, Figure 3.31 shows how orbits characterised as sticky orbits according to the criterion $\chi \in [10^{-4}, 10^{-2}]$ are considered to be chaotic when ε increases. The maximum percentage of sticky orbits is obtained when $\varepsilon = \frac{4.5}{2\pi}$ and $\frac{5}{2\pi}$. Furthermore, there are no sticky orbits when $\varepsilon = \frac{0.5}{2\pi}$ and $\frac{10}{2\pi}$. In particular, when $\varepsilon = \frac{10}{2\pi}$ almost all orbits are highly chaotic. This result shows that the relative perturbation strength controls the chaoticity of the system. It also depicts how the nature of studied orbits change as ε increases. On the other hand, Figure 3.32 depicts the percentage of escaping (i.e., orbits for which $\psi > 1.8$) and non-escaping orbits of the system, for various values of the perturbation strength. We observe that for very low values of $\varepsilon \leq 1.5$ no orbit escapes, and as ε increases more orbits escape. It is important to note that these analyses were carried out for 10^5 iterations, since there is no significant difference in the chaotic fraction of the system between 10^5 and 10^6 iterations.

From the results obtained in Figure 3.30(b) we conclude that the number of iterations does not affect the nature of orbits in the phase space, rather the relative perturbation strength does. Also, in order to accurately quantify chaotic regions it is important to choose an appropriate threshold value for the mLCE, as in our case the threshold $\chi = 10^{-2}$ was chosen from Figure 3.18(a).

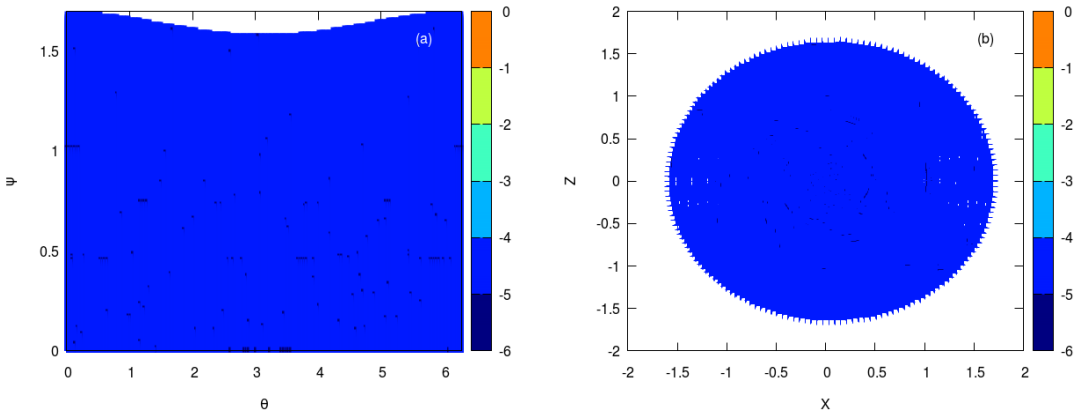

Figure 3.21: Regions of different values of the mLCE on the PSS, $\varepsilon = 0.5/2\pi$ for (a) magnetic coordinates (θ, ψ) and (b) polar coordinates $X = \psi\cos\theta$, $Z = \psi\sin\theta$. The colour bar represents the $\log_{10}$(mLCE) final value of each initial condition. The corresponding PSS is shown in Figure 3.9.

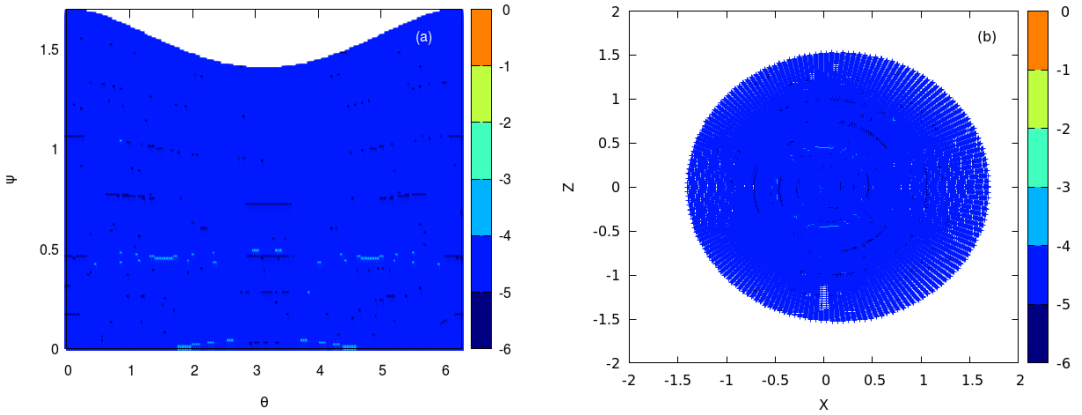

Figure 3.22: Same as Figure 3.21, but for $\varepsilon = 1.5/2\pi$. The corresponding PSS is shown in Figure 3.10.

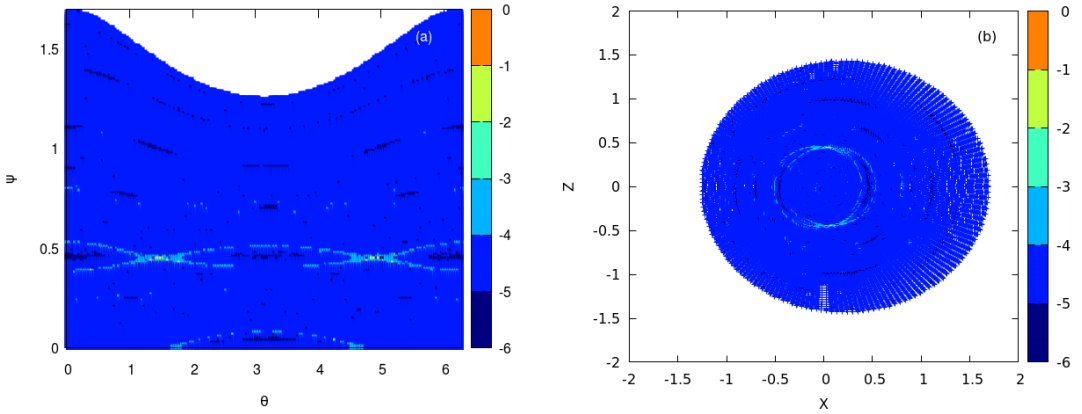

Figure 3.23: Same as Figure 3.21, but for $\varepsilon = 2.55/2\pi$. The corresponding PSS is shown in Figure 3.11.

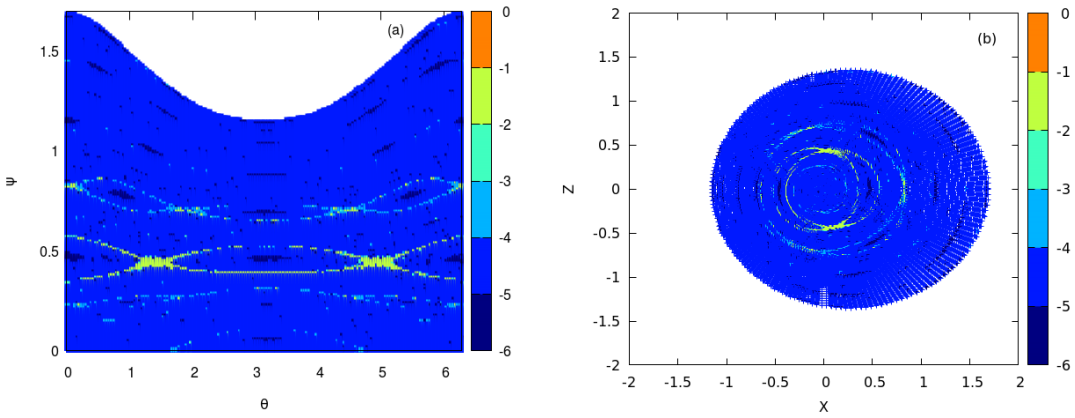

Figure 3.24: Same as Figure 3.21, but for $\varepsilon = 3.5/2\pi$. The corresponding PSS is shown in Figure 3.12.

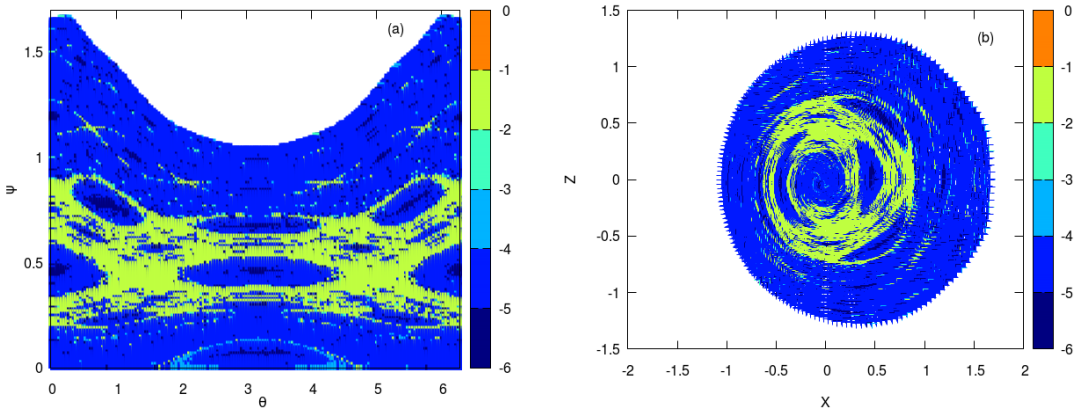

Figure 3.25: Same as Figure 3.21, but for $\varepsilon = 4.5/2\pi$. The corresponding PSS is shown in Figure 3.13.

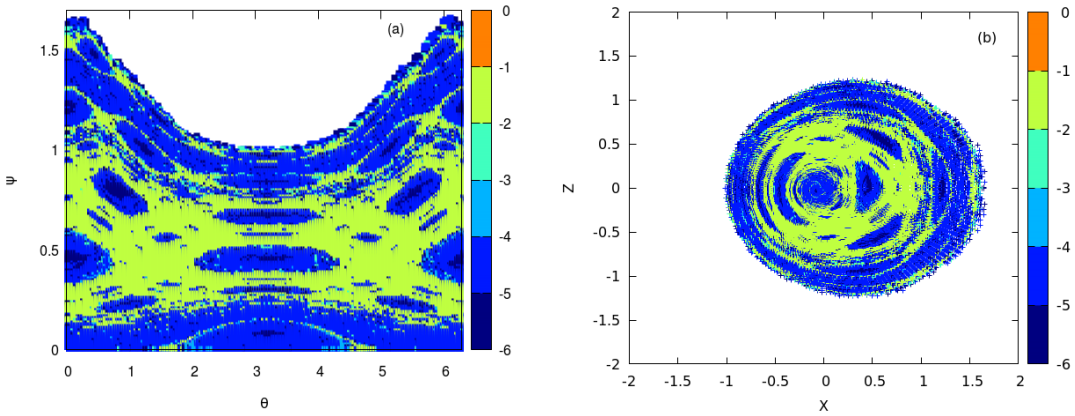

Figure 3.26: Same as Figure 3.21, but for $\varepsilon = 5/2\pi$. The corresponding PSS is shown in Figure 3.14.

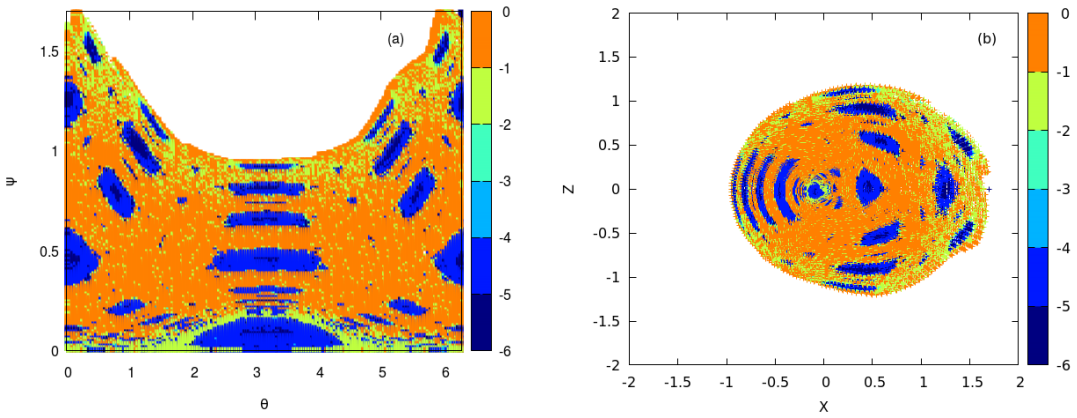

Figure 3.27: Same as Figure 3.21, but for $\varepsilon = 6/2\pi$. The corresponding PSS is shown in Figure 3.15.

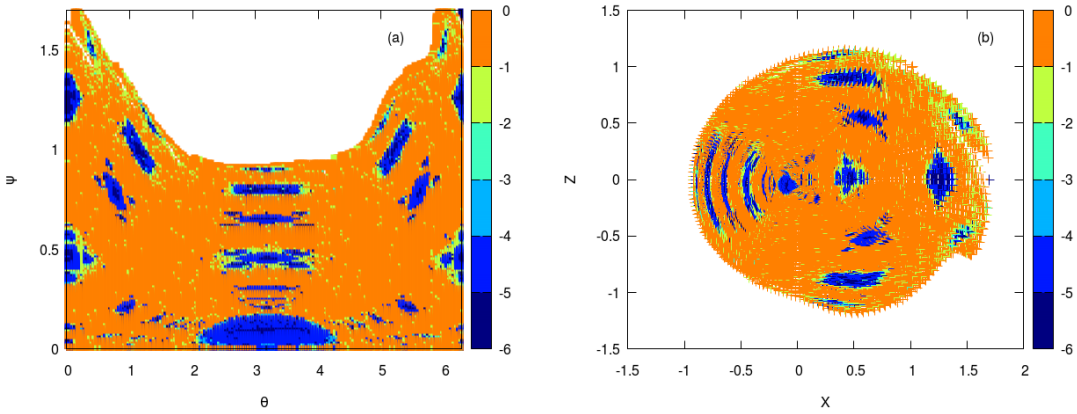

Figure 3.28: Same as Figure 3.21, but for $\varepsilon = 6.5/2\pi$. The corresponding PSS is shown in Figure 3.16.

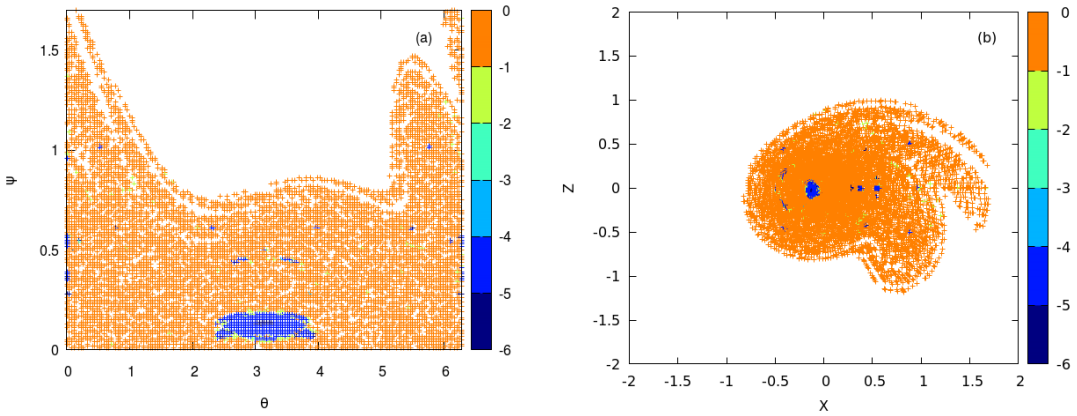

Figure 3.29: Same as Figure 3.21, but for $\varepsilon = 9/2\pi$. The corresponding PSS is shown in Figure 3.17.

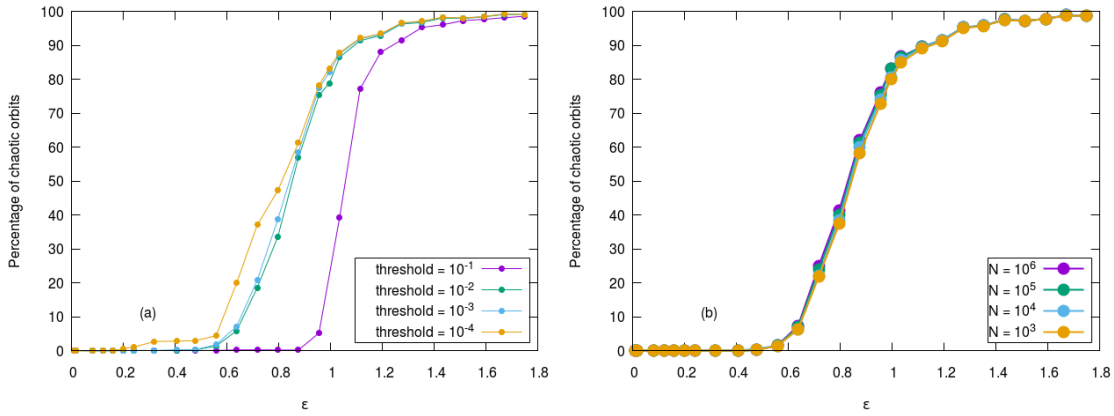

(a) Different threshold values of χ. (b) Different integration time.

Figure 3.30: The percentage of chaotic orbits as a function of the perturbation strength ε, for (a) different threshold values of $\chi = 10^{-1}, 10^{-2}, 10^{-3}, 10^{-4}$, for chaotic orbits; (b) different number of iterations $N = 10^3, 10^4, 10^5, 10^6$, with the threshold value of the mlCE for chaotic orbits $\chi = 10^{-2}$.

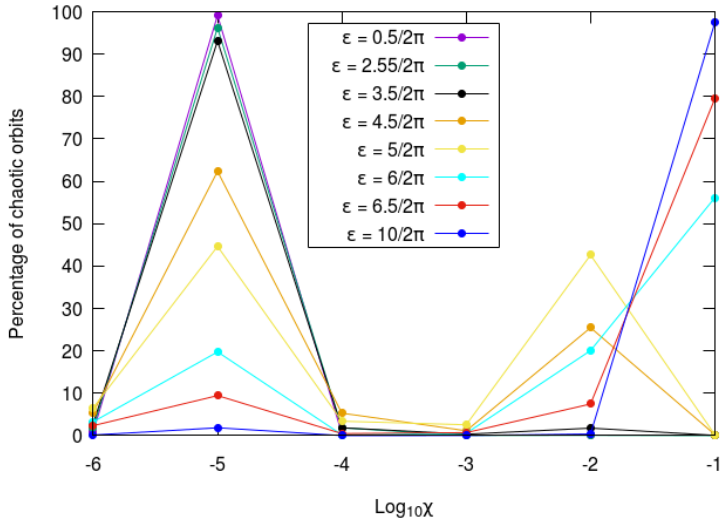

Figure 3.31: The percentage of chaotic orbits (or sticky orbits) against the mLCE χ, for different values of the relative perturbation strength ε. χ is in log scale and the threshold value of the mLCE for chaotic orbits is $\chi = 10^{-2}$.

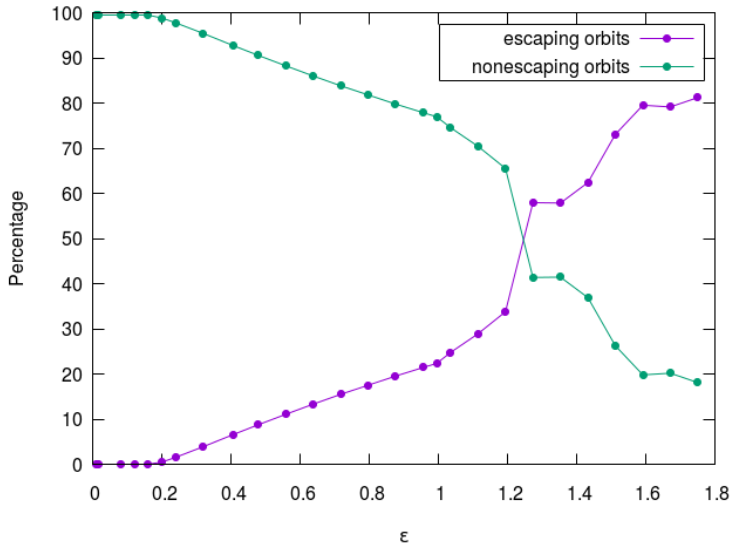

Figure 3.32: The percentage of escaping and nonescaping orbits against the relative perturbation strength, for ε.

The SALI of orbits of the symmetric tokamap

The chaotic behaviour of orbits is also analysed using the computation of the SALI. This was carried out by using the evolution of nearby orbits method. The results obtained are depicted in Figure 3.33(a), where the SALI for regular orbits tends to zero following the power law N^{-2}. As was predicted in Section 2.2.3, in Figure 3.33(b) the SALI for chaotic orbits tends to zero exponentially. It can be seen in Figure 3.34 that the exponential decay of SALI for chaotic orbits is in accordance with (2.2.8), for $\chi_1 = 0.0453$ and $\chi_1 = 0.0367$ (which are good estimations of the mLCE) for $\psi = 0.36$ and $\psi = 0.72$, respectively. This behaviour corresponds to the theoretical prediction of SALI and clearly discriminates chaotic and regular orbits.

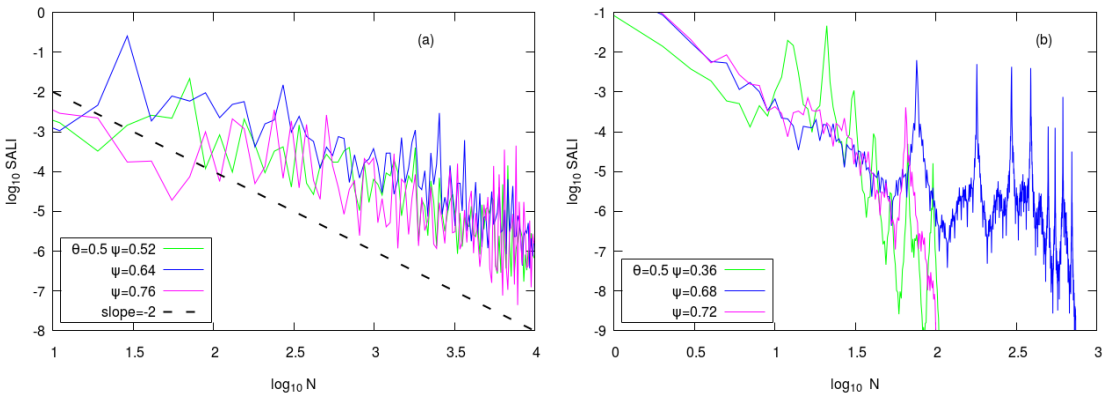

Figure 3.33: Plot of the SALI against the number of iterations, for (a) regular orbits (black dashed line denote slope =-2); (b) chaotic orbits, for $\varepsilon = 4.5/2\pi$. Both axes are in logarithmic scale.

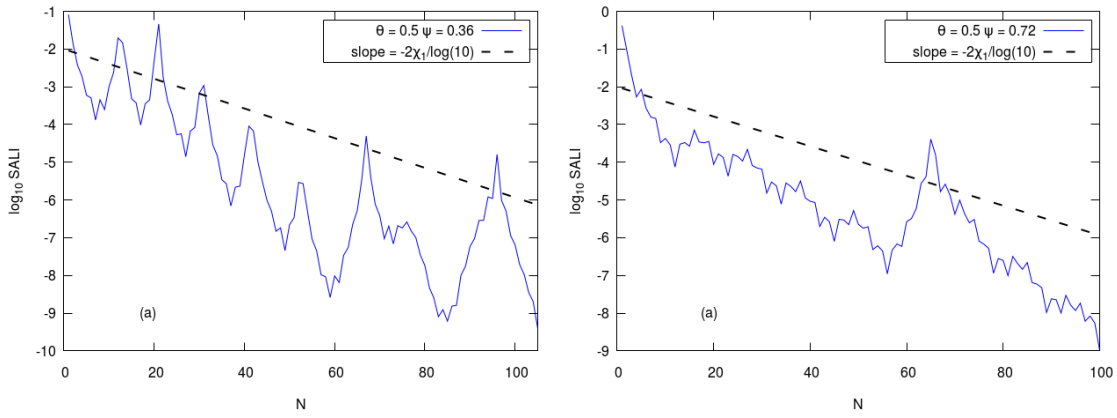

Figure 3.34: Plots of the SALI for chaotic orbits in linear time, for $\varepsilon = 4.5/2\pi$. The dashed black line corresponds to a function proportional to $e^{-2\chi_1 N}$, for $\chi_1 = 0.0453$ and $\chi_1 = 0.0367$ in (a) and (b), respectively.

3.5 Diffusion of Magnetic Field Lines

In order to describe the diffusion of magnetic field lines in a chaotic zone, we evolve a set of 1000 magnetic field lines. Initial conditions are chosen at $\psi = 0.001$ and θ being distributed uniformly in the interval $[0, 2\pi]$, as a bunch of magnetic field lines for several values of the relative perturbation strength ε. It is important to note that although the motion of a field line is discrete, average properties like the mean poloidal flux ψ_m and the mean square displacement of the flux (MSD), averaged over initial conditions can be described by continuous functions of time - the number of toroidal turns. Therefore, the mean poloidal flux is defined as

$$\psi_m(N) \equiv < \psi(N) >, \tag{3.5.1}$$

where $< \cdots >$ denotes the average over initial conditions, while the MSD is defined by

$$\text{MSD}(N) = < (\psi(N) - < \psi(N) >)^2 > . \tag{3.5.2}$$

We also illustrate the diffusion of field lines by determining the running diffusion coefficient

$$D = \frac{1}{2}\frac{\text{MSD}}{N}. \tag{3.5.3}$$

According to Wingen et al. (2005), the critical perturbation ε_c for the destruction of the lower KAM surface, situated just above the plasma core, has the value $\varepsilon_c = 5.719/2\pi$. Furthermore, Wingen et al. (2005) were able to show that the characteristic time

$$T_D \approx (\varepsilon - \varepsilon_c)^{-3}, \tag{3.5.4}$$

i.e., the time when the MSD starts increasing, depends on the difference $\varepsilon - \varepsilon_c$. We also consider the Lyapunov characteristic time scale

$$T_L = \frac{1}{< \chi_1 >}, \tag{3.5.5}$$

which quantifies the time the system becomes chaotic and its comparison with T_D.

In Figures 3.35, 3.36, 3.37, 3.38 and 3.39 we plot: (a) the mean flux against time N; (b) the MSD (3.5.2) of the flux against time N. In these figures we can see that the mean flux and the MSD remain constant throughout the evolution. This shows that for $\varepsilon < \varepsilon_c$, there is no diffusion of magnetic field lines, as the lower KAM surface is not destroyed. However, for perturbations $\varepsilon > \varepsilon_c$ the mean poloidal flux and the MSD are no longer constant, as the lower KAM surface is destroyed. This is evident in Figures 3.40, 3.41 and 3.42. In Figure 3.40, we observe that for $\varepsilon = 6/2\pi$, diffusion starts when $N \approx 1100$ (Figure 3.40(b)) and the escape time, i.e., time at which field lines reach the plasma edge $\psi = 1$ is $T_e \approx 10^5$, this can be seen at the point of intersection of the dashed and solid curve in Figure 3.40(a). In the same vein, for $\varepsilon = 6.5/2\pi$ the diffusion time is $N \approx 500$ (Figure 3.41(b)) and the escape time is $T_e \approx 10^4$ (Figure 3.41(a)). Finally, for $\varepsilon = 9/2\pi$, we can see that the diffusion time is $N \approx 10$ (Figure 3.42(b)), while the escape time is $T_e \approx 10^2$ (Figure 3.42(a)). Moreover, Figure 3.43 validates the claim that diffusion occurs when $\varepsilon > \varepsilon_c$, as we can see that the running diffusion coefficient D_ψ is zero for all values of $\varepsilon < \varepsilon_c$. The comparison of T_D and T_L is shown in Table 3.1 for $\varepsilon > \varepsilon_c$ and we deduce that a high degree of chaoticity is required for the diffusion of magnetic field lines as chaos occurs way before diffusion in the magnetic field.

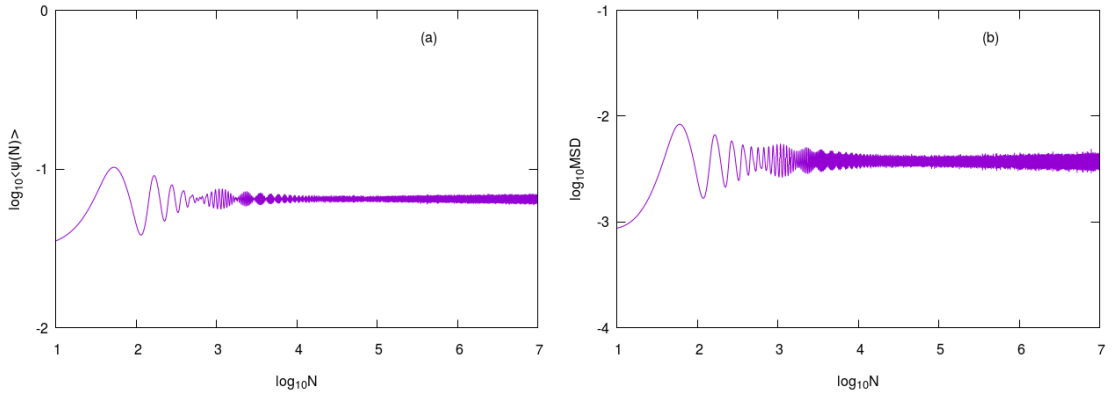

Figure 3.35: Plot of (a) the mean flux (3.5.1) against the number of iterations N and (b) the MSD (3.5.2) of the flux against time N of the symmetric tokamap (3.4.2), for 1000 initial conditions chosen at $\psi = 0.001$ and $\theta \in [0, 2\pi]$, with $\varepsilon = 0.5/2\pi$. Both axes are in log scale.

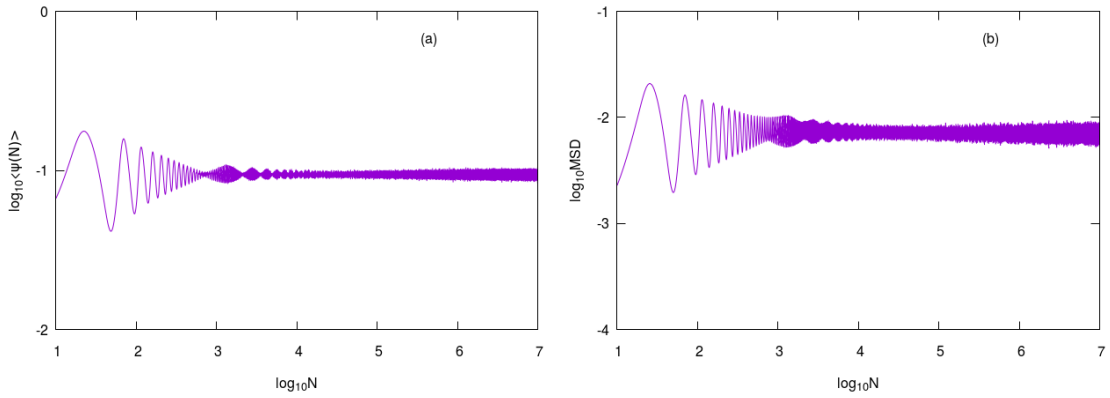

Figure 3.36: Similar to Figure 3.35, but for $\varepsilon = 1.5/2\pi$.

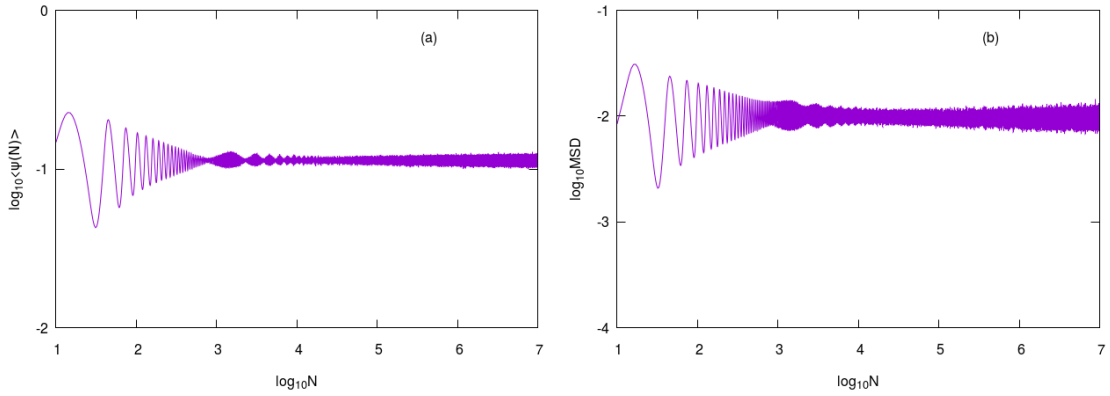

Figure 3.37: Similar to Figure 3.35, but for $\varepsilon = 2.55/2\pi$.

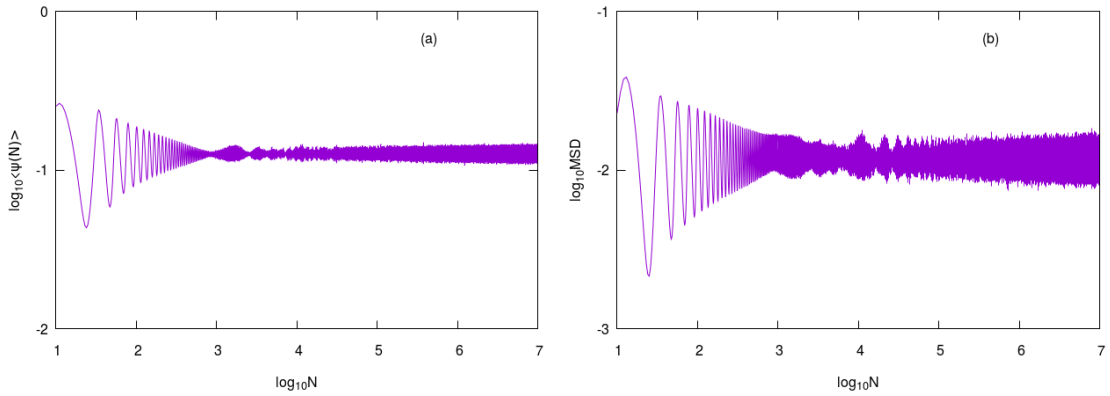

Figure 3.38: Similar to Figure 3.35, but for $\varepsilon = 3.5/2\pi$.

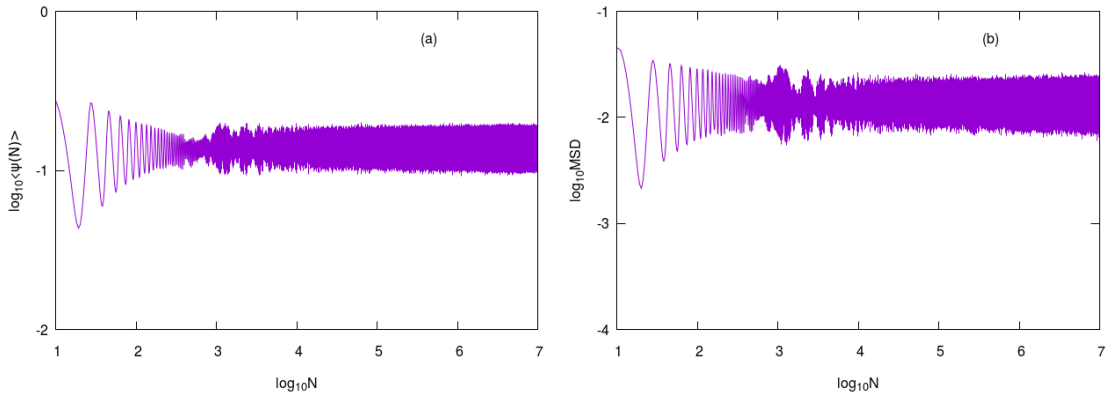

Figure 3.39: Similar to Figure 3.35, but for $\varepsilon = 4.5/2\pi$.

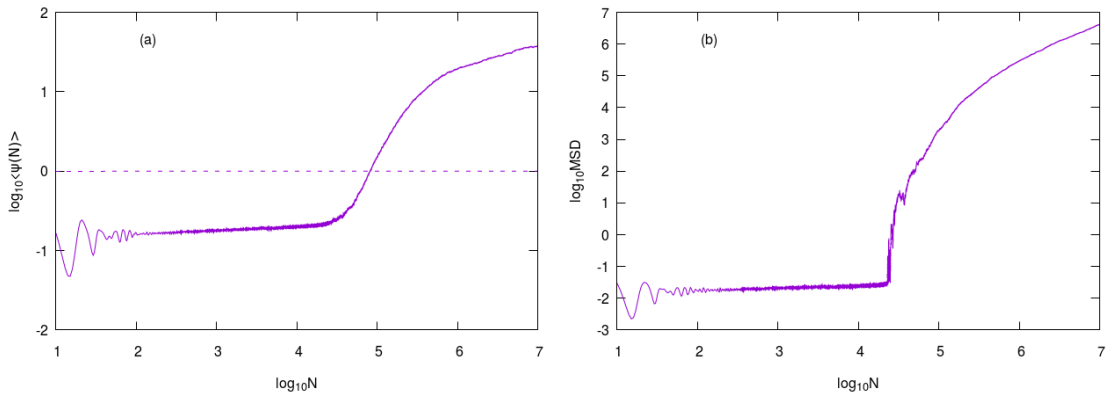

Figure 3.40: Similar to Figure 3.35, but for $\varepsilon = 6/2\pi$. The dashed line corresponds to the plasma edge at $\psi = 1$.

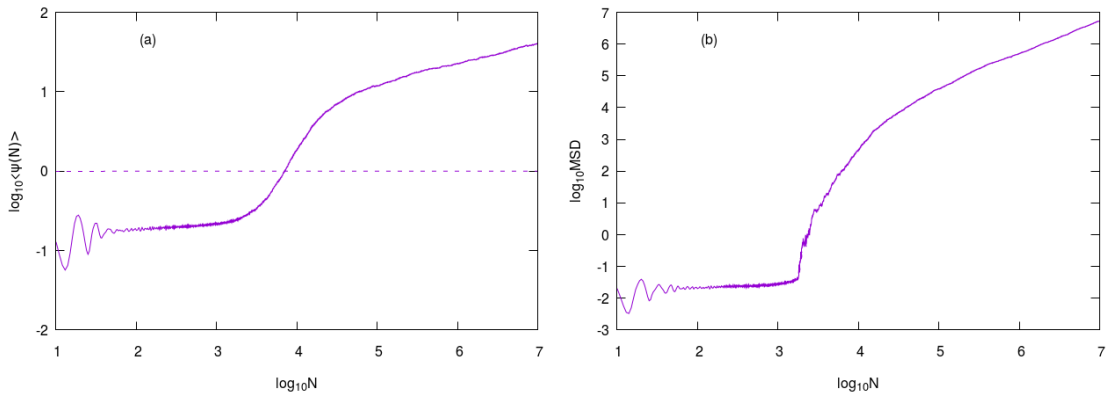

Figure 3.41: Similar to Figure 3.40, but for $\varepsilon = 6.5/2\pi$.

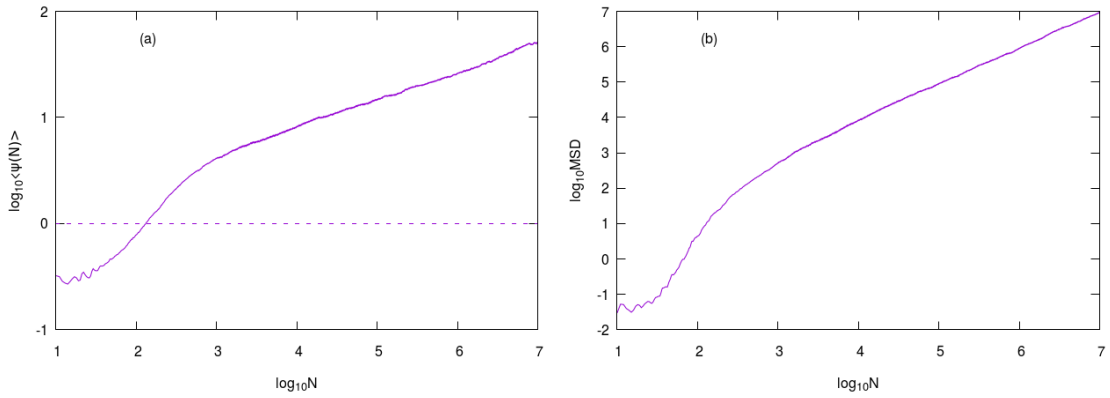

Figure 3.42: Similar to Figure 3.40, but for $\varepsilon = 9/2\pi$.

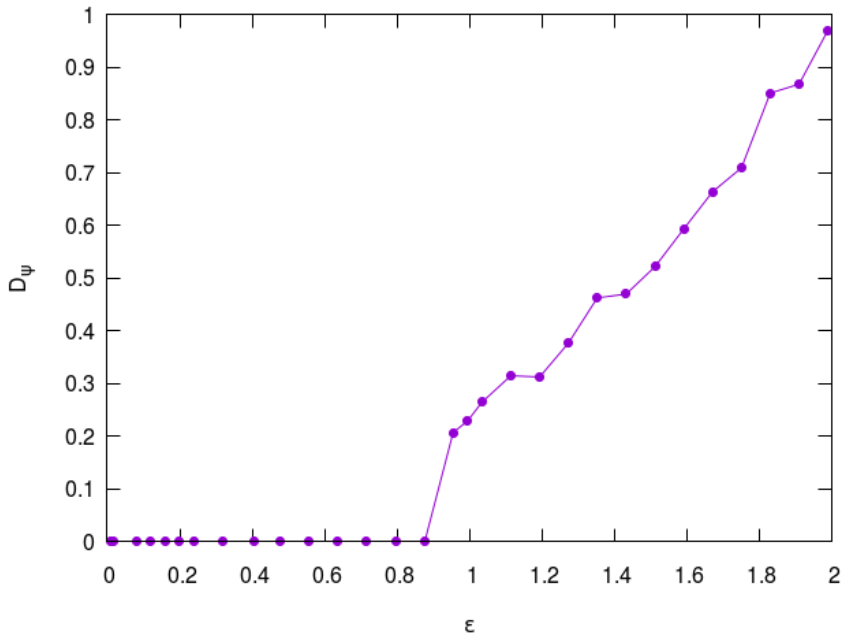

Figure 3.43: Plot of the diffusion coefficient of the symmetric tokamap (3.4.2) against ε.

ε	T_D	T_L
$6/2\pi$	11179.46	13.04
$6.25/2\pi$	1656.75	9.15
$6.5/2\pi$	520.70	7.55
$7/2\pi$	118.00	5.39
$7.5/2\pi$	43.91	4.31
$8/2\pi$	20.90	3.58
$8.5/2\pi$	11.53	3.04
$9/2\pi$	7.02	2.68
$9.5/2\pi$	4.59	2.31
$10/2\pi$	3.16	2.08
$10.5/2\pi$	2.27	1.89
$11/2\pi$	1.68	1.70
$11.5/2\pi$	1.28	1.53
$12/2\pi$	1.00	1.40
$12.5/2\pi$	0.80	1.32

Table 3.1: Numerical results for the characteristic time T_D (3.5.4) for diffusion and the Lyapunov T_L (3.5.5) time.

4. Explicit Near-Symplectic Map of the Symmetric Tokamap with Lie-generating Functions

A characteristic feature of a Hamiltonian system is its ability to conserve certain invariant quantities, this property is known as the symplectic property. Over the years the construction of symplectic mappings has been done using several approaches (Chirikov, 1979; Lichtenberg and Lieberman, 1992). One of such approaches is the rigorous method developed by Abdullaev (2002) using the Hamilton-Jacobi theory and the canonical perturbation theory, which results in implicit mappings representing perturbed magnetic field lines. In particular, the symmetric tokamap is one of these mappings. However, these mappings are not without shortcomings, as their implicit nature results in a significant increase in their computation time as a result of the iterative procedure adopted in the numerical solutions of the corresponding algebraic equations. On the other hand, explicit symplectic integrators (Hairer et al., 1993; Laskar and Robutel, 2001; Hairer et al., 2006) have been developed for Hamiltonian systems of the form

$$H(q,p) = R(q) + S(p),$$

where q represents generalised coordinates and p represents conjugate momenta. But, many studied models do not fall in this category, one of such is the Hamiltonian (3.4.1). In this study, we present a method for constructing an explicit near-symplectic mapping for this Hamiltonian using Lie transforms.

First, following Kominis et al. (2008) we consider a general form of a near-integrable Hamiltonian

$$H(\mathbf{P},\theta,t) = H_0(\mathbf{P}) + \varepsilon \sum_{m\neq 0} H_{\mathbf{m}}(\mathbf{P},t)e^{i\mathbf{m}\theta},$$

with $\mathbf{P} = (P_1, P_2, ..., P_N)$, $\theta = (\theta_1, \theta_2, ..., \theta_N)$, $\mathbf{m} = (m_1, m_2, ..., m_N)$, being the momenta, generalised coordinates and the poloidal modes, respectively. The evolution of $\mathbf{y}(\theta_{t_k}, \mathbf{P}_{t_k})$ to $\mathbf{y}(\theta_{t_{k+1}}, \mathbf{P}_{t_{k+1}})$ is governed by the action of the time-dependent operator $R_H(t_{k+1}, t_k)$ in the form

$$\mathbf{y}(t_{k+1}) = R_H(t_{k+1}, t_k)\mathbf{y}(t_k).$$

Nevertheless, the time-propagation operator cannot be easily obtained. Thus, the utilisation of the transformation

$$\mathbf{y}' = T(y,t)\mathbf{y}$$

leads to a new Hamiltonian system $G(\mathbf{y}', t)$, from which the time-propagation operator is easily obtained. The action of $R_G(t_{k+1}, t_k)$ on the new variables $\mathbf{y}'$ is given by

$$\begin{aligned} \theta'(t_{k+1}) &= \theta'(t_k) + \int_{t_k}^{t_{k+1}} \omega_{\mathbf{G}}(\mathbf{P}', s)ds, \\ \mathbf{P}'(t_{k+1}) &= \mathbf{P}'(t_k), \end{aligned} \tag{4.0.1}$$

where $\omega_{\mathbf{G}} = \frac{\partial G(\mathbf{P}',t)}{\partial \mathbf{P}'}$.

The time propagation of $\mathbf{y}_k$ to $\mathbf{y}_{k+1}$ in first order is given by

$$\mathbf{y}(t_{k+1}) = (T_0^{-1} + T_1^{-1}) R_G(t_{k+1}, t_k)(T_0 + T_1)\mathbf{y}(t_k), \tag{4.0.2}$$

with

$$T_0 = I, \qquad T_1 = -L_1, \qquad T_1^{-1} = L_1, \tag{4.0.3}$$

I being the identity operator and $L_i f = [w_i, f]$, $i = 1, 2, \cdots$, where $[.,.]$ denotes the Poisson bracket[1].

In the same manner, the second order propagation of $\mathbf{y}_k$ to $\mathbf{y}_{k+1}$ is given by

$$\mathbf{y}(t_{k+1}) = (T_0^{-1} + T_1^{-1} + T_2^{-1}) R_G(t_{k+1}, t_k)(T_0 + T_1 + T_2)\mathbf{y}(t_k), \tag{4.0.4}$$

with

$$T_2 = -\frac{1}{2}L_2 + \frac{1}{2}L_1^2, \qquad T_2^{-1} = \frac{1}{2}L_2 + \frac{1}{2}L_1^2. \tag{4.0.5}$$

Using (4.0.3) in (4.0.2) and (4.0.5) in (4.0.4) the first and second order transformations are given as

$$\mathbf{y}(t_{k+1}) = (I + L_1)\, R_G\, (I - L_1)\, \mathbf{y}(t_k), \tag{4.0.6}$$

and

$$\mathbf{y}(t_{k+1}) = \left(I + L_1 + \frac{1}{2}L_2 + \frac{1}{2}L_1^2\right) R_G \left(I - L_1 - \frac{1}{2}L_2 + \frac{1}{2}L_1^2\right) \mathbf{y}(t_k), \tag{4.0.7}$$

respectively.

It follows that the first order-term of the new Hamiltonian and the first order Lie generator w_1 are given as

$$G_1 = 0 \tag{4.0.8}$$

and

$$w_1 = \sum_{m \neq 0} F_{1,\mathbf{m}} e^{i\mathbf{m}\cdot\theta}, \tag{4.0.9}$$

where

$$F_{1,\mathbf{m}} = -A_{\mathbf{m}}(\mathbf{P}) e^{-i\mathbf{m}\cdot\omega_{\mathbf{m}} t} b_{\Omega_{\mathbf{m}}}(t, t_0), \quad b_{\Omega_{\mathbf{m}}}(t, t_0) = \frac{e^{-i\Omega_{\mathbf{m}} t} - e^{-i\Omega_{\mathbf{m}} t_0}}{i\Omega_{\mathbf{m}}}, \tag{4.0.10}$$

with

$$\Omega_{\mathbf{m}} = \omega_{\mathbf{m}} + \mathbf{m} \cdot \omega_0.$$

Similarly, the second order-term of the new Hamiltonian and the second order Lie generator w_2 are given by

$$G_2 = -\frac{i}{2} \sum_{\mathbf{m} \neq 0} \mathbf{m} \cdot \left[\frac{\partial (A_{\mathbf{m}}^2 e^{-i\Omega_{\mathbf{m}} t})}{\partial \mathbf{P}} b_{\Omega_{\mathbf{m}}}(t, t_0) + i \frac{\partial (\mathbf{m} \cdot \omega_0)}{\partial \psi} A_{\mathbf{m}}^2 e^{-i\Omega_{\mathbf{m}} t_0} d_{\Omega_{\mathbf{m}}}(t, t_0) \right] \tag{4.0.11}$$

[1] The Poisson bracket of functions $f(\vec{q}, \vec{p})$ and $g(\vec{q}, \vec{p})$ is defined as $[f, g] = \sum_{i=1}^{N} \left(\frac{\partial f}{\partial q_i} \frac{\partial g}{\partial p_i} - \frac{\partial f}{\partial p_i} \frac{\partial g}{\partial q_i} \right)$.

and

$$w_2 = \sum_{m\neq 0} F_{2,\mathbf{m}} \cdot e^{i\mathbf{m}\cdot\theta}, \tag{4.0.12}$$

where

$$F_{2,\mathbf{m}} = -i \sum_{\mathbf{m}_1+\mathbf{m}_2=\mathbf{m}} e^{-i\mathbf{m}\cdot\omega_0 t}\Bigg[\left(-A_{m_1}\mathbf{m}_1\cdot\frac{\partial A_{\mathbf{m}_2}}{\partial \mathbf{P}} + A_{m_2}\mathbf{m}_2\cdot\frac{\partial A_{\mathbf{m}_1}}{\partial \mathbf{P}}\right)\frac{b_{\Omega_{\mathbf{m}_1}+\Omega_{\mathbf{m}_2}} - e^{-i\Omega_{\mathbf{m}_1}t_0}b_{\Omega_{\mathbf{m}_2}}}{i\Omega_{\mathbf{m}_1}}$$
$$- iA_{\mathbf{m}_1}A_{\mathbf{m}_2}\mathbf{m}_2\cdot\frac{\partial(\mathbf{m}_1\cdot\omega_0)}{\partial\mathbf{P}}\frac{e^{i\Omega_{\mathbf{m}_1}t}(i\Omega_{\mathbf{m}_2})d_{\Omega_{\mathbf{m}_2}} + e^{i\Omega_{\mathbf{m}_2}t_0}(i\Omega_{\mathbf{m}_1})d_{\Omega_{\mathbf{m}_1}} - i(\Omega_{\mathbf{m}_1}+\Omega_{\mathbf{m}_2})d_{\Omega_{\mathbf{m}_1}+\Omega_{\mathbf{m}_2}}}{(i\Omega_{\mathbf{m}_1})(i\Omega_{\mathbf{m}_1})}\Bigg], \tag{4.0.13}$$

$$d_{\Omega_{\mathbf{m}}}(t,t_0) = \frac{(i\Omega_{\mathbf{m}}t-1)e^{i\Omega_{\mathbf{m}}t} - (i\Omega_{\mathbf{m}}t_0-1)e^{i\Omega_{\mathbf{m}}t_0}}{(i\Omega_{\mathbf{m}})^2}. \tag{4.0.14}$$

Now we consider the Hamiltonian (3.4.1)

$$H = \int \frac{d\psi}{q(\psi)} + \varepsilon\frac{\psi}{1+\psi}\cos(\theta)\sum_{s=-M}^{M}\cos(s\zeta), \quad \text{with } q(\psi) = \frac{4}{(2-\psi)(2-2\psi+\psi^2)}. \tag{4.0.15}$$

The expression H^c defined as

$$H^c = H_0 - \sum_{s=-M}^{M} s\psi + \varepsilon\frac{\psi}{\psi+1}\cos(\theta)\sum_{s=-M}^{M}\cos(s\zeta) \tag{4.0.16}$$

is a constant of motion of the Hamiltonian H, since

$$\begin{aligned}\frac{dH^c}{d\zeta} &= \frac{\partial H^c}{\partial\zeta} + [H,H^c]\\ &= -\varepsilon\frac{\psi}{\psi+1}\cos(\theta)\sum_{s=-M}^{M} s\sin(s\zeta) + \frac{\partial H}{\partial\theta}\cdot\frac{\partial H^c}{\partial\psi} - \frac{\partial H}{\partial\psi}\cdot\frac{\partial H^c}{\partial\theta}\\ &= \varepsilon\frac{\psi}{\psi+1}\sin(\theta)\sum_{s=-M}^{M}\cos(s\zeta)\cdot\sum_{s=-M}^{M} s\\ &= 0.\end{aligned}$$

Since H has one constant of motion, H is integrable with

$$H_0(\psi) = -\frac{\psi^4}{16} + \frac{\psi^3}{3} - \frac{3\psi^2}{4} + \psi$$

being the unperturbed Hamiltonian. Then, we get

$$\omega_0(\psi) = G_0 = \frac{\partial H_0}{\partial\psi} = -\frac{\psi^3}{4} + \psi^2 - \frac{3}{2}\psi + 1, \tag{4.0.17}$$

and $\mathbf{m} = 1$.

We set $t \equiv \zeta$, so that

$$\sum_{s=-M}^{M} \cos(st) = Re\left(\sum_{s=-M}^{M} e^{ist}\right),$$

and

$$\gamma(t) = \sum_{s=-M}^{M} \cos(st) \equiv 2\sum_{s=0}^{M} e^{ist} = 2\sum_{s=-M}^{0} e^{ist}.$$

Now we have that

$$H \equiv H_0(\psi) + \varepsilon\frac{\psi}{1+\psi}\cdot e^{i\theta}\cdot\gamma(t) = H_0(\psi) + 2\varepsilon\frac{\psi}{1+\psi}\cdot\sum_{s=0}^{M} e^{i(\theta+st)},$$

with

$$H_1(\psi,t) = A_1(\psi)\sum_{s=0}^{M} e^{i(\theta+st)},$$

where $A_1(\psi) = \frac{\psi}{1+\psi}$.

Consequently, following (4.0.8), (4.0.9) and (4.0.10) the first order generating function is obtained as follows: the first order term of the new Hamiltonian is

$$G_1 = 0, \tag{4.0.18}$$

and the first order Lie-generator is given by

$$w_1 = F_{1,1}\cdot e^{i\theta}, \tag{4.0.19}$$

where

$$F_{1,1} = -A_1\sum_{s=0}^{M} e^{-i\omega_0 t} b_{\Omega_s}(t,t_0), \tag{4.0.20}$$

$$b_{\Omega_s}(t,t_0) = \frac{e^{-i\Omega_s t} - e^{-i\Omega_s t_0}}{i\Omega_s}, \text{ with } \Omega_s = \omega_s + \omega_0 = s + \omega_0,\ t_0 = t_k + dt/2. \tag{4.0.21}$$

Likewise, the second order term of the new Hamiltonian G_2 is obtained as

$$G_2 = -\frac{i}{2}\left[\sum_{s=-M}^{M}\frac{\partial(A_1^2 e^{-i\Omega_s t})}{\partial\psi} b_{\Omega_s}(t,t_0) + i\frac{\partial(\omega_0)}{\partial\psi}A_1^2 e^{-i\Omega_s t_0} d_{\Omega_s}(t,t_0)\right], \tag{4.0.22}$$

with

$$d_{\Omega_s}(t,t_0) = \frac{(i\Omega_s t_0 - 1)e^{i\Omega_s t_0} - (i\Omega_s t - 1)e^{i\Omega_s t}}{\Omega_s^2}. \tag{4.0.23}$$

From (4.0.13), we have that $\mathbf{m_1}$=$\mathbf{m_2}$=1. Since $\mathbf{m_1}$=$\mathbf{m_2}$, then

$$-A_{m_1}\mathbf{m}_1\cdot\frac{\partial A_{\mathbf{m}_2}}{\partial\psi} + A_{m_2}\mathbf{m}_2\cdot\frac{\partial A_{\mathbf{m}_1}}{\partial\psi} = -A_1\cdot\frac{\partial A_1}{\partial\psi} + A_1\cdot\frac{\partial A_1}{\partial\psi} = 0$$

and so,

$$F_{2,2} = -i \sum_{s=-M}^{M} e^{-i2\omega_0 t} \left[A_1^2 \cdot \frac{\partial(\omega_0)}{\partial\psi} \frac{(e^{i\Omega_s t} + e^{i\Omega_s t_0})\Omega_s d_{\Omega_s} - 2\Omega_s d_{2\Omega_s}}{\Omega_s^2} \right]. \tag{4.0.24}$$

Thus, following (4.0.12), we have that

$$w_2 = F_{2,2} \cdot e^{i2\theta}. \tag{4.0.25}$$

The first order transformation (4.0.6),

$$L_1 \mathbf{y} = \left[w_1, \begin{pmatrix} \theta \\ \psi \end{pmatrix} \right],$$

gives

$$[w_1, \theta] = \frac{\partial w_1}{\partial \theta} \cdot \frac{\partial \theta}{\partial \psi} - \frac{\partial w_1}{\partial \psi} \cdot \frac{\partial \theta}{\partial \theta} = -\frac{\partial w_1}{\partial \psi} \tag{4.0.26}$$

and

$$[w_1, \psi] = \frac{\partial w_1}{\partial \theta} \cdot \frac{\partial \psi}{\partial \psi} - \frac{\partial w_1}{\partial \psi} \cdot \frac{\partial \psi}{\partial \theta} = \frac{\partial w_1}{\partial \theta}. \tag{4.0.27}$$

Using (4.0.26) and (4.0.27) the $\mathbf{y}_k(\theta, \psi)$ to $\mathbf{y}'_k(\theta', \psi')$ transformation is given by

$$\begin{aligned} \theta'_{t_k} &= \theta_{t_k} - [w_1, \theta], \\ \psi'_{t_k} &= \psi_{t_k} - [w_1, \psi]. \end{aligned} \tag{4.0.28}$$

The subsequent propagation of $\mathbf{y}'_k$ to $\mathbf{y}'_{k+1}$ given the new Hamiltonian $G = G_0 + G_1$, and $\omega_G = \frac{\partial G}{\partial \psi'}$, is defined by

$$\begin{aligned} \theta'_{t_{k+1}} = \theta'_{t_k} + \int_{t_k}^{t_{k+1}} \omega_{\mathbf{G}} dr = \theta'_{t_k} + (t_{k+1} - t_k) \cdot \omega_0(\psi'_{t_k}), \\ \psi'_{t_{k+1}} = \psi'_{t_k}. \end{aligned} \tag{4.0.29}$$

Similar to the $\mathbf{y}_k \to \mathbf{y}'_k$ transformation, the inverse transformation of $\mathbf{y}'_{k+1}$ to $\mathbf{y}_{k+1}$ is given by

$$\begin{aligned} \theta_{t_{k+1}} &= \theta'_{t_{k+1}} + [w_1, \theta'], \\ \psi_{t_{k+1}} &= \psi'_{t_{k+1}} + [w_1, \psi']. \end{aligned} \tag{4.0.30}$$

Thus, the first order explicit map is given by

$$\begin{aligned} \theta'_{t_k} &= \theta_{t_k} - [w_1, \theta], \\ \psi'_{t_k} &= \psi_{t_k} - [w_1, \psi], \\ \theta'_{t_{k+1}} &= \theta'_{t_k} + (t_{k+1} - t_k) \cdot \omega_0(\psi'), \\ \psi'_{t_{k+1}} &= \psi'_{t_k}, \\ \theta_{t_{k+1}} &= \theta'_{t_{k+1}} + [w_1, \theta'], \\ \psi_{t_{k+1}} &= \psi'_{t_{k+1}} + [w_1, \psi']. \end{aligned} \tag{4.0.31}$$

Using the second order transformation (4.0.7),

$$L_1^2\mathbf{y} = \left[w_1, \left[w_1, \begin{pmatrix}\theta\\ \psi\end{pmatrix}\right]\right]$$

gives

$$[w_1,[w_1,\theta]] = \frac{\partial w_1}{\partial\theta}\cdot\frac{\partial}{\partial\psi}\left(-\frac{\partial w_1}{\partial\psi}\right) - \frac{\partial w_1}{\partial\psi}\cdot\frac{\partial}{\partial\theta}\left(-\frac{\partial w_1}{\partial\psi}\right) \tag{4.0.32}$$

and

$$[w_1,[w_1,\psi]] = \frac{\partial w_1}{\partial\theta}\cdot\frac{\partial}{\partial\psi}\left(\frac{\partial w_1}{\partial\theta}\right) - \frac{\partial w_1}{\partial\psi}\cdot\frac{\partial}{\partial\theta}\left(\frac{\partial w_1}{\partial\theta}\right). \tag{4.0.33}$$

Similarly, from (4.0.7) we have that

$$L_2\mathbf{y} = \left[w_2, \begin{pmatrix}\theta\\ \psi\end{pmatrix}\right]$$

yields

$$[w_2,\theta] = \frac{\partial w_2}{\partial\theta}\cdot\frac{\partial\theta}{\partial\psi} - \frac{\partial w_2}{\partial\psi}\cdot\frac{\partial\theta}{\partial\theta} = -\frac{\partial w_2}{\partial\psi} \tag{4.0.34}$$

and

$$[w_2,\psi] = \frac{\partial w_2}{\partial\psi}\cdot\frac{\partial\psi}{\partial\psi} - \frac{\partial w_2}{\partial\psi}\cdot\frac{\partial\psi}{\partial\theta} = \frac{\partial w_2}{\partial\theta}. \tag{4.0.35}$$

Consequently, using (4.0.32), (4.0.33), (4.0.34) and (4.0.35), with $G = G_0 + G_1 + G_2$, the second order explicit map is given by

$$\begin{aligned}
\theta'_{t_k} &= \theta_{t_k} - [w_1,\theta] - \frac{1}{2}[w_2,\theta] + \frac{1}{2}[w_1,[w_1,\theta]],\\
\psi'_{t_k} &= \psi_{t_k} - [w_1,\psi] - \frac{1}{2}[w_2,\psi] + \frac{1}{2}[w_1,[w_1,\psi]],\\
\theta'_{t_{k+1}} &= \theta'_{t_k} + (t_{k+1}-t_k)\cdot\omega_0(\psi') + \int_{t_k}^{t_{k+1}}\omega_{G_2}(\psi'),\\
\psi'_{t_{k+1}} &= \psi'_{t_k},\\
\theta_{t_{k+1}} &= \theta'_{t_{k+1}} + [w_1,\theta'] + \frac{1}{2}[w_2,\theta'] + \frac{1}{2}[w_1,[w_1,\theta']],\\
\psi_{t_{k+1}} &= \psi'_{t_{k+1}} + [w_1,\psi'] + \frac{1}{2}[w_2,\psi'] + \frac{1}{2}[w_1,[w_1,\psi']].
\end{aligned} \tag{4.0.36}$$

It is important to note that the first and second order explicit mappings obtained in (4.0.31) and (4.0.36) are not exactly symplectic (see (Kominis et al., 2008)), but as $\varepsilon \to 0$ they are taken to be near-symplectic. Also, keeping the time interval τ small ensures the rapid decrease of the effective perturbation strength $\varepsilon' \sim \varepsilon(t-t_0)^a c(\mathbf{P})$, where a depends on the form of the perturbation term and $c(\mathbf{P})$ is a function dependent on the momenta, which is localised around resonant surfaces. As a consequence, increasing the accuracy of the maps.

4.1 Numerical Investigations

The stroboscopic construction of the Poincaré surface of section using the first and second order explicit maps involves taking one step of the computation to correspond to a period of the driving force τ. In Figures 4.1 through 4.3 we plot the PSS of the first order explicit map (4.0.31), the second order explicit map (4.0.36) and the first order implicit map (symmetric tokamap) (3.4.2), for $\zeta = 0$, with initial conditions $\theta = 0, \psi = 0.5$. These figures show that for a single time harmonic s, a small value of the perturbation strength $\varepsilon = 0.01$ and a very small time step $\tau = 2\pi/100$, the first (green curve) and second (light blue curve) order explicit maps are equivalent, as they create regular magnetic field lines just like the implicit symmetric tokamap (purple curve). Furthermore, Figures 4.4(a) and 4.5(a) show that for multiple time harmonics the first and second order explicit maps create regular trajectories. Moreover, in Figure 4.6 we plot the PSS for a single time harmonic $s = 1$ and $\varepsilon = 0.01$, using the first order explicit map (since its equivalence to the second order explicit maps has been shown), for 30 initial conditions, with $\theta = 0$ and ψ being uniformly distributed in the interval [0,1]. Similarly, Figure 4.7 shows the PSS for 30 initial conditions chosen as the former, but for multiple time harmonics $s = 0, 1, 2$. These results are in accordance with the phase space dynamics of the symmetric tokamap for $\varepsilon = 0.01$, as shown in Figure 4.8, using the same initial conditions as in Figure 4.6. Thus, for small values of the perturbation strength, just like for the symmetric tokamap, flux surfaces are not broken, as regular curves are created and no island chain exists

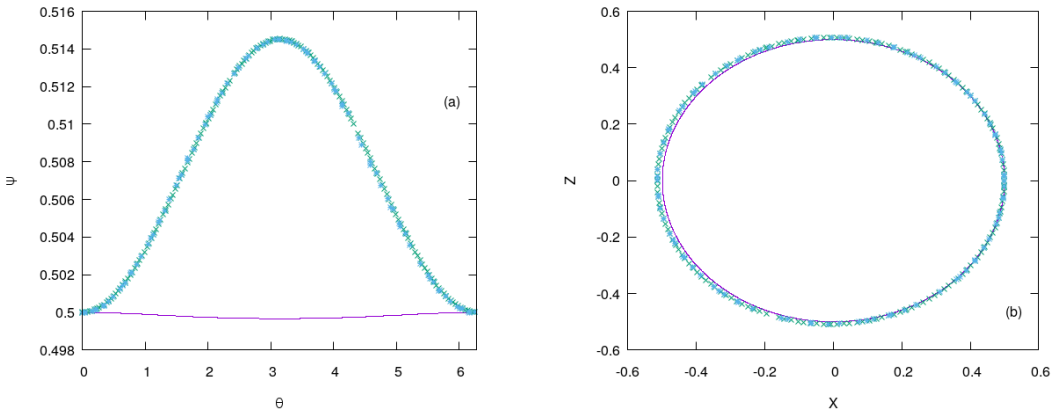

Figure 4.1: The PSS, in (a) is the magnetic coordinates and in (b) is the polar coordinates of the first order explicit map (green curve), the second order explicit map (light blue curve) and the symmetric tokamap (purple curve), for $\zeta = 0$ having initial conditions (θ, ψ)=(0,0.5), with $\varepsilon = 0.01$, for a single time harmonic: $s = 0$, $\tau = 2\pi/100$ and total time 200π.

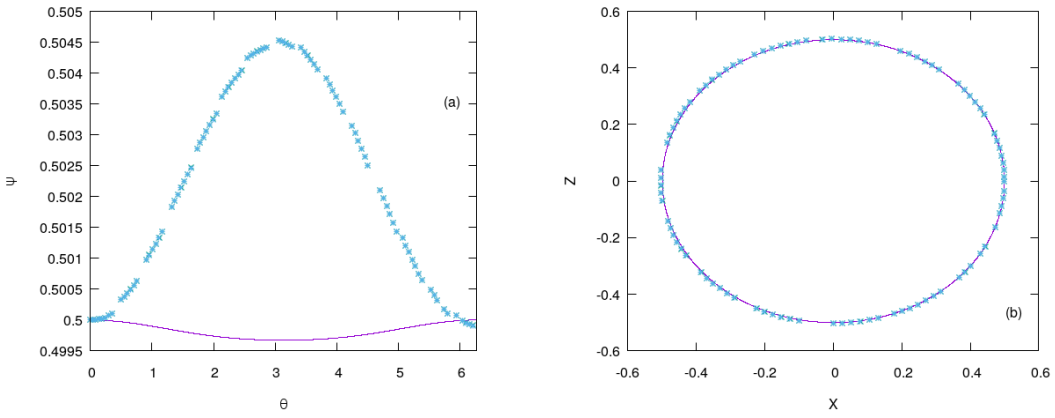

Figure 4.2: Same as 4.1, but for $s = 1$.

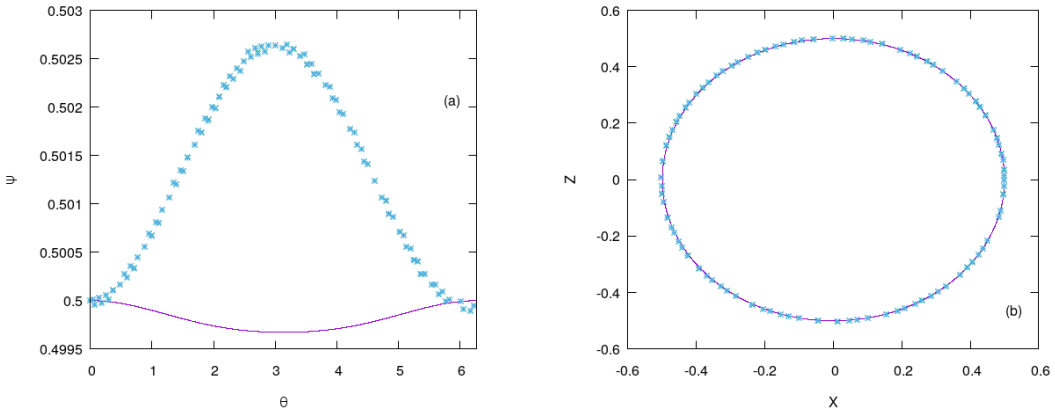

Figure 4.3: Same as 4.1, but for $s = 2$.

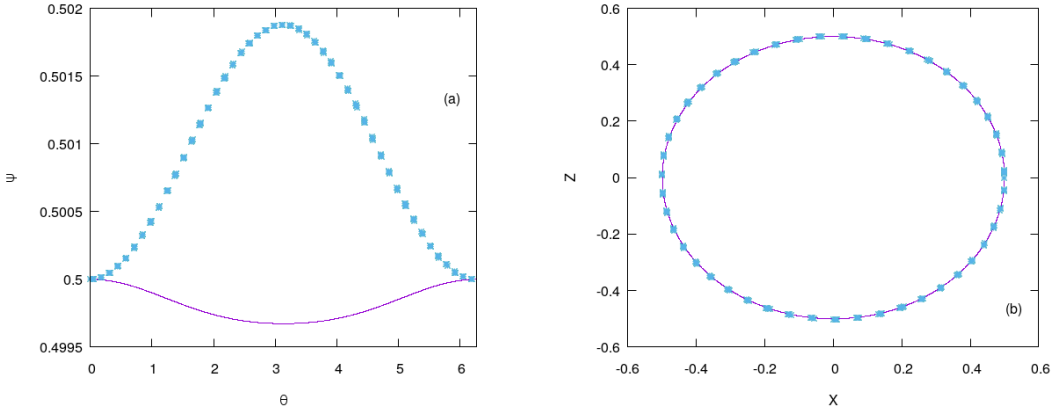

Figure 4.4: Same as 4.1, but for $\varepsilon = 0.001$ and multiple time harmonics $s = 0, 1$.

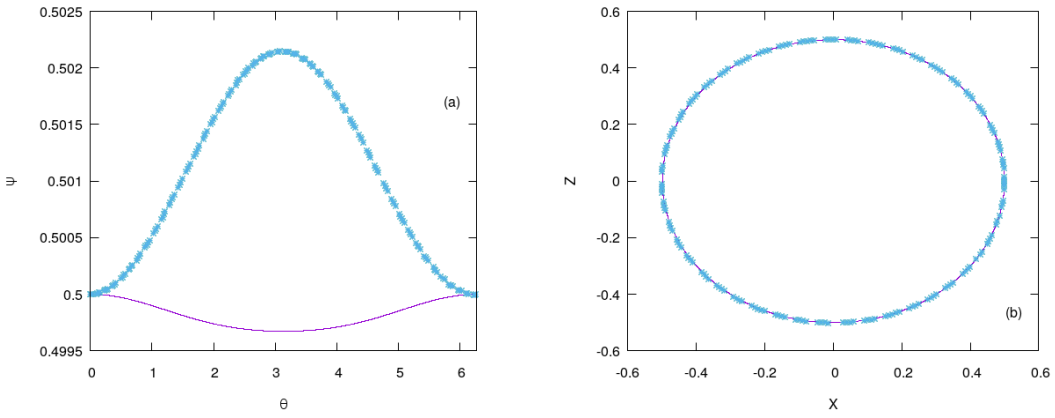

Figure 4.5: Same as 4.1, but for multiple time harmonics $s = 0, 1, 2$.

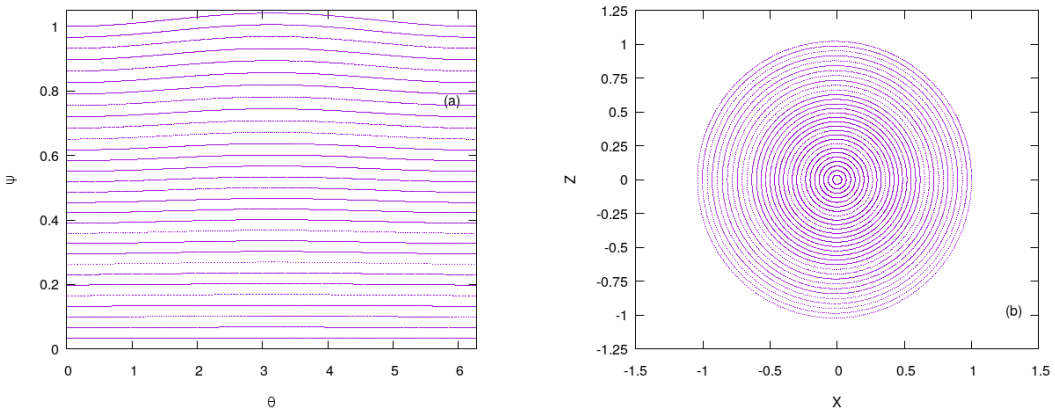

Figure 4.6: The PSS for a single time harmonic $s = 1$, with $\varepsilon = 0.01$,for 30 initial conditions: fixed $\theta = 0$, ψ is uniformly distributed in [0,1], using the first order explicit map (4.0.31).

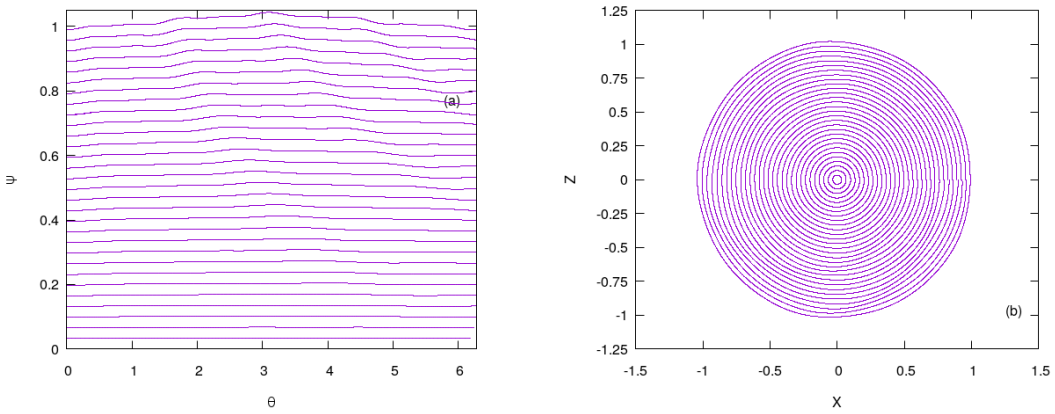

Figure 4.7: Same as Figure 4.6, but for multiple time harmonics $s = 0, 1, 2$.

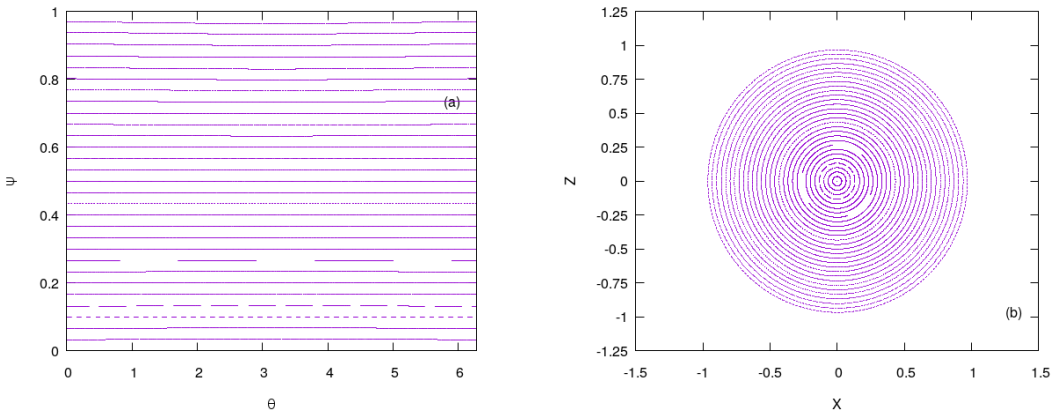

Figure 4.8: Same as Figure 4.6, but using the implicit symmetric tokamap.

In Figure 4.9(a))and 4.9(b)) the relative energy error $R.E. = \frac{|H^c(N)-H^c(0)|}{H^c(0)}$ against time of the numerical integrations of the orbit with initial conditions $\theta = 0$, $\psi = 0.5$ and $\theta = 1$, $\psi = 0.5$, respectively are computed. These results show that for $\tau = 2\pi$, the second order explicit map is a bit more accurate than the first order explicit map although the constant of motion is not conserved. This shows that for accurate computation, smaller values of τ should be used. Figure 4.10 shows the relative energy error $R.E.$ against time of the numerical integrations of the orbit with initial conditions $\theta = 0$, $\psi = 0.5$ when a time iteration step $\tau = 2\pi/100$ is used, for several values of ε, using the first order explicit map (4.0.31) (Figure 4.10(a)), the second order explicit map (4.0.36) (Figure 4.10(b)) and the first order implicit map (3.4.2) (Figure 4.10(c)). The figure shows that for small values of ε, the constant of motion H^c (4.0.16) is conserved and that the accuracy of the map increases by one order of magnitude when ε decreases by one order of magnitude. This implies that the aforementioned maps are near-symplectic and that their accuracies are influenced by the relative perturbation strength ε. The same behaviour is observed for multiple time harmonics, as can be seen in Figure 4.11. Also, we observe that in terms of accuracy, for small values of ϵ the three maps are equivalent irrespective of their orders as shown in Figure 4.12. This is because for a small time iteration step τ the effective perturbation ε' which is a function of a power of τ becomes very small, thus improving the symplecticity and accuracy of the first order explicit map. These results are valid for small values of ε for which the corresponding explicit maps are near-symplectic. Furthermore, Figure 4.13 shows the efficiency of all three maps for the orbit $\theta = 0$, $\psi = 0.5$, with $\varepsilon = 0.01$ and $\tau = 2\pi/100$, as the first order explicit map (purple curve) has the smallest computation time, with the second order explicit map (light blue curve) having the largest computation time. We can see that for the given iteration time step $\tau = 2\pi/100$, the first order explicit map is the most efficient one.

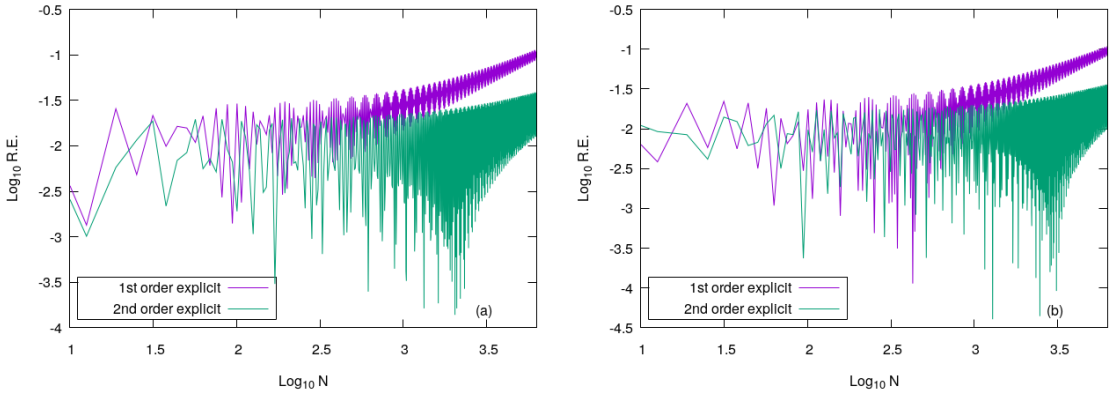

Figure 4.9: Plots of the relative energy error $R.E. = \frac{|H^c(N)-H^c(0)|}{H^c(0)}$ of the first and second order explicit maps (4.0.31) for the initial conditions (a) $\theta = 0$, $\psi = 0.5$ (b) $\theta = 1$, $\psi = 0.5$, with $\tau = 2\pi$. All axes are in logarithmic scale.

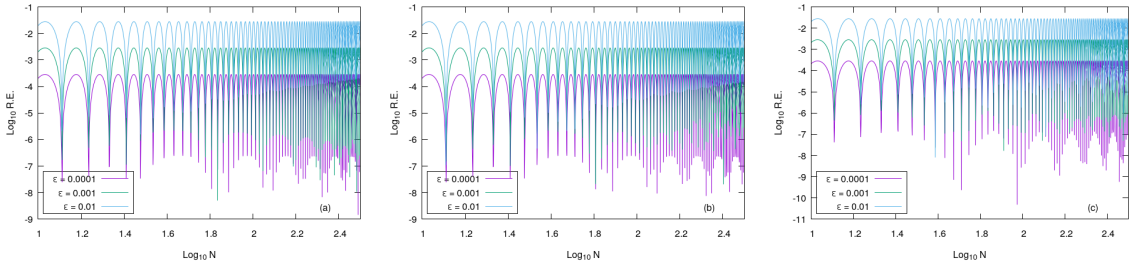

Figure 4.10: Plots of the relative energy error $R.E. = \frac{|H^c(N)-H^c(0)|}{H^c(0)}$ of (a) the first order explicit map (4.0.31), (b) the second order explicit map (4.0.36), (c) the first order implicit map (3.4.2) against time, for a single time harmonic $s = 1$, with $\theta = 0$, $\psi = 0.5$ and $\tau = 2\pi/100$. All axes are in logarithmic scale.

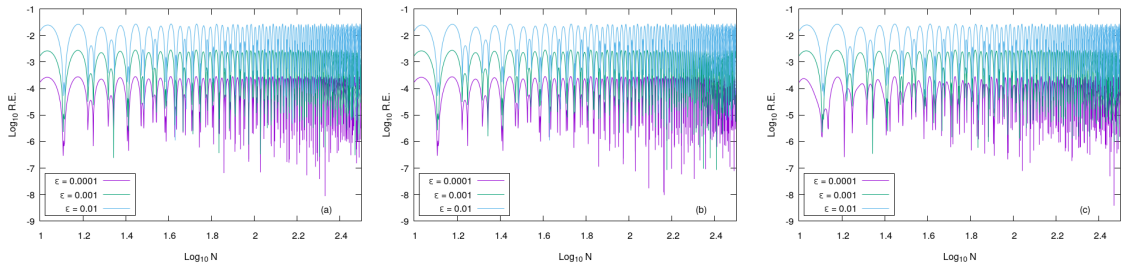

Figure 4.11: Same as Figure 4.10, but for multiple time harmonics $s = 0, 1, 2$.

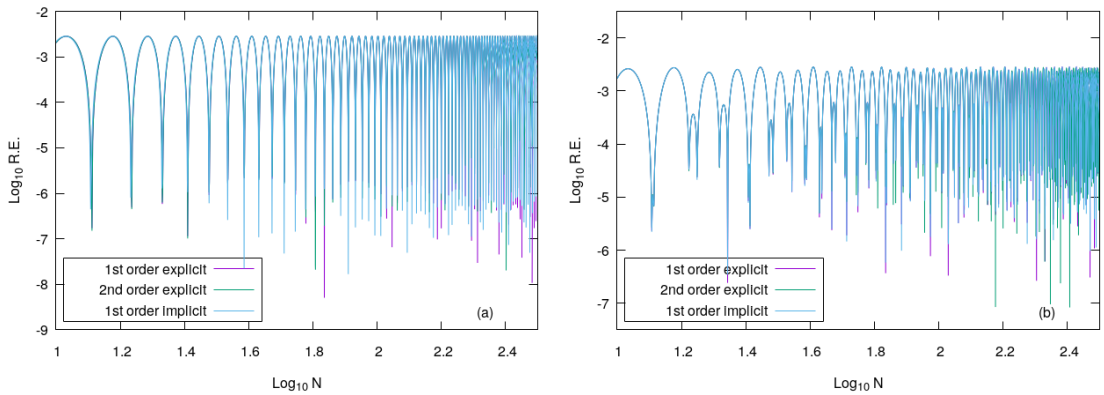

Figure 4.12: Plots of the relative energy error of the first order explicit map (4.0.31) (purple curve), the second order explicit map (4.0.36) (green curve) and the first order implicit map (3.4.2) (light blue curve) against time, for (a) a single time harmonic $s = 1$, (b) multiple time harmonics $s = 0, 1, 2$, with $\theta = 0$, $\psi = 0.5$, $\varepsilon = 0.001$ and $\tau = 2\pi/100$. All axes are in logarithmic scale.

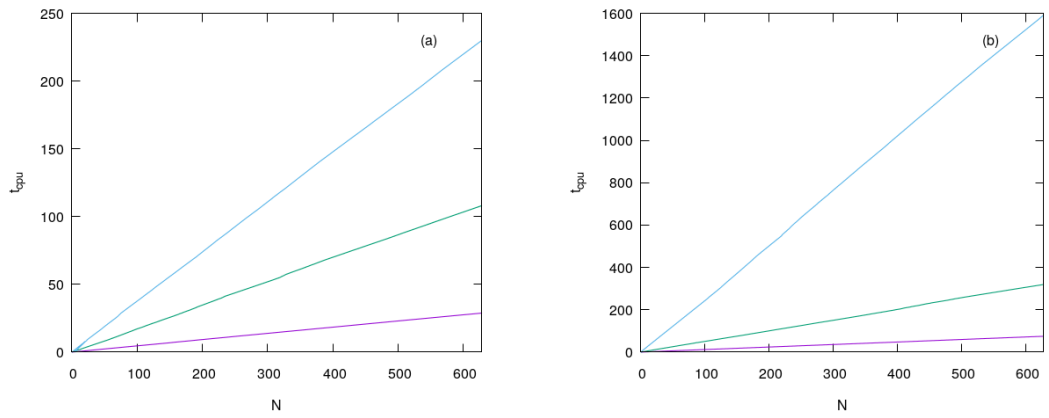

Figure 4.13: The CPU time t_{cpu}, i.e., the computational time as a function of the number of iterations N for (a) a single time harmonic s, (b) mutiple time harmonics $s = 0, 1, 2$, for the second order explicit map (light blue curve) (4.0.36), the first order implicit map (green curve) (3.4.2) and the first order explicit map (purple curve) (4.0.31), with $\varepsilon = 0.01$.

5. Summary and Conclusions

We presented several numerical techniques for investigating the chaotic dynamics of Hamiltonian systems and symplectic mappings. In particular, we considered the creation of the Poincaré surface of sections (PSSs), and the computation of the Lyapunov characteristic exponents (LCEs), the Smaller Alignment Index (SALI) and the Generalised Alignment Index (GALI). We also used as examples for their illustrations the Hénon-Heiles system, the 2D standard map and the 4D Froeschlé symplectic map. Moreover, we compared two numerical methods of computing quantitative chaos indicators, namely: the time evolution of nearby orbits and the integration/iteration of the variational equations/tangent map methods and we established the equivalence of the results obtained by these methods.

We also discussed the representation of magnetic fields in tokamak devices, as well as the destruction of magnetic surfaces in the presence of nonaxisymmetric perturbations. It was shown that magnetic field lines are Hamiltonian in nature. As a result, Hamiltonian formulation was used to illustrate the dynamics of magnetic field lines in tokamak devices by implementing the Poincaré surface of sections, the maximum Lyapunov characteristic exponent (mLCE) and the Smaller Alignment Index methods, for the investigation of the chaotic behaviour of the studied systems.

In addition, the chaoticity of the symmetric tokamap was critically analysed in order to understand its phase space dynamics. The PSS was used to visualise the system's phase space, while the mLCE and the SALI were used to quantitatively describe the chaotic behaviour of the system. Due to the implicit nature of the symmetric tokamap, the mLCE and SALI methods were implemented using the time evolution of nearby orbits, since its equivalence to the iteration of the tangent map method has been previously established. In particular, the mLCE method was used to accurately estimate the percentage of chaotic orbits as a function of the relative perturbation strength of the system. The mLCE was used to create Scan maps for the visualisation of very small regions of regular and chaotic motion that were not easily seen by the PSS technique. It is worth noting that, to the best of our knowledge, the use of the time evolution of three nearby orbits for the computation of SALI as well as the use of many nearby orbits for the computation of GALIs have not been presented before in the literature. Our results showed that the physical quantity that influences the system's chaoticity is the relative perturbation strength of the system.

Furthermore, the investigation of the diffusive properties of the symmetric tokamap using statistical measures such as the mean square displacement and the calculation of diffusion coefficients was presented. It was shown that a high degree of chaoticity is required for the diffusion of magnetic field lines to occur. These results are typical for the behaviour of magnetic field lines in chaotic plasmas and could help provide a better understanding of the fully developed turbulent plasma.

Finally, to overcome the complexity associated with the implicit nature of the symmetric tokamap, the construction of explicit near-symplectic mappings via Lie-generating functions was presented. The dynamics of the explicit mappings were studied using the PSS. It was shown that for small values of the perturbation strength and for very small iteration time steps, the explicit mappings are as accurate as the implicit maps, but are computationally more efficient. These explicit mappings could be useful in practical cases where efficiency and accuracy of computations are required. In addition, explicit maps could be used to overcome the challenge associated with implicit maps for the computation of chaos indicators using variational equations.

In the future, we shall attempt to understand the guiding centre motion of charged particles in chaotic magnetic fields, using the tools implemented in this work.

Acknowledgements

First, I would like to thank my supervisor Associate Professor Haris Skokos for guiding me through this study and believing in my ability to successfully carry out this research. I would also like to thank Dr. Yannis Kominis for useful discussions, especially on the construction of explicit near-symplectic mappings. Furthermore, I would like to thank my colleagues in the "Nonlinear Dynamics and Chaos" group for useful discussions and making my time in the group a memorable one. Finally, I would like to thank the University of Cape Town (UCT), the African Institute for Mathematical Sciences (AIMS) South Africa, and the National Research Foundation (NRF) of South Africa (Prof. Skokos' Incentive Funding for Rated Researchers, IFFR and Competitive Programme for Rated Researchers, CPRR projects) for funding this work.

References

S. Abdullaev. The hamilton-jacobi method and hamiltonian maps. *Journal of Physics A: Mathematical and General*, 35(12):2811, 2002.

S. Abdullaev. On mapping models of field lines in a stochastic magnetic field. *Nuclear Fusion*, 44(6): S12, 2004.

S. Abdullaev. Model of a magnetic field in poloidal divertor tokamaks affected by resonant magnetic perturbations. *Physics of plasmas*, 16(3):030701, 2009.

S. Abdullaev. Magnetic stochasticity in magnetically confined fusion plasmas. *Cham–Heidelberg: Springer-Verlag*, 2014.

S. Abdullaev, K. Finken, A. Kaleck, and K. Spatschek. Twist mapping for the dynamics of magnetic field lines in a tokamak ergodic divertor. *Physics of Plasmas*, 5(1):196–210, 1998.

S. Abdullaev, M. Jakubowski, M. Lehnen, O. Schmitz, and B. Unterberg. On description of magnetic stochasticity in poloidal divertor tokamaks. *Physics of plasmas*, 15(4):042508, 2008.

H. Ali, A. Punjabi, A. Boozer, and T. Evans. The low mn map for single-null divertor tokamaks. *Physics of Plasmas*, 11(5):1908–1919, 2004.

R. Balescu, M. Vlad, and F. Spineanu. Tokamap: A hamiltonian twist map for magnetic field lines in a toroidal geometry. *Physical Review E*, 58(1):951, 1998.

G. Benettin, L. Galgani, A. Giorgilli, and J.-M. Strelcyn. Lyapunov characteristic exponents for smooth dynamical systems and for hamiltonian systems; a method for computing all of them. part 1: Theory. *Meccanica*, 15(1):9–20, 1980a.

G. Benettin, L. Galgani, A. Giorgilli, and J.-M. Strelcyn. Lyapunov characteristic exponents for smooth dynamical systems and for hamiltonian systems; a method for computing all of them. part 1: Numerical application. *Meccanica*, 15(1):21–30, 1980b.

B. V. Chirikov. A universal instability of many-dimensional oscillator systems. *Physics reports*, 52(5): 263–379, 1979.

G. Contopoulos, L. Galgani, and A. Giorgilli. On the number of isolating integrals in hamiltonian systems. *Physical Review A*, 18(3):1183, 1978.

R. L. Devaney. *An introduction to chaotic dynamical systems*, volume 13046. Addison-Wesley Reading, 1989.

R. Freis, C. Hartman, F. Hamzeh, and A. Lichtenberg. Magnetic-island formation and destruction in a levitron. *Nuclear Fusion*, 13(4):533, 1973.

C. Froeschlé. Numerical study of a four-dimensional mapping. *Astronomy and Astrophysics*, 16:172, 1972.

G. H. Golub and C. Reinsch. Singular value decomposition and least squares solutions. *Numerische mathematik*, 14(5):403–420, 1970.

E. Hairer, S. Nørsett, and G. Wanner. Solving ordinary differential equations i: nonstiff problems, vol. 8. *Springer Ser. Comput. Math*, 1993.

E. Hairer, C. Lubich, and G. Wanner. *Geometric numerical integration: structure-preserving algorithms for ordinary differential equations*, volume 31. Springer Science & Business Media, 2006.

M. Henon. On the numerical computation of poincaré maps. *Physica D: Nonlinear Phenomena*, 5(2-3): 412–414, 1982.

M. Henon and C. Heiles. The applicability of the third integral of motion: some numerical experiments. *The Astronomical Journal*, 69:73, 1964.

ITER. ITER project. http://www.iter.org, Accessed January 2018.

JET. Jet. http://www.euro-fusion.org/jet, Accessed January 2018.

D. Kerst. The influence of errors on plasma-confining magnetic fields. *Journal of Nuclear Energy. Part C, Plasma Physics, Accelerators, Thermonuclear Research*, 4(4):253, 1962.

A. Kolmogorov. On the conservation of conditionally periodic motions under small perturbation of the hamiltonian. In *Dokl. Akad. Nauk. SSR*, volume 98, pages 2–3, 1954.

Y. Kominis, K. Hizanidis, D. Constantinescu, and O. Dumbrajs. Explicit near-symplectic mappings of hamiltonian systems with lie-generating functions. *Journal of Physics A: Mathematical and Theoretical*, 41(11):115202, 2008.

J. Laskar and P. Robutel. High order symplectic integrators for perturbed hamiltonian systems. *Celestial Mechanics and Dynamical Astronomy*, 80(1):39–62, 2001.

J. D. Lawson. Some criteria for a power producing thermonuclear reactor. *Proceedings of the Physical Society. Section B*, 70(1):6, 1957.

A. J. Lichtenberg and M. A. Lieberman. Regular and chaotic dynamics, vol. 38 of. *Applied Mathematical Sciences*, 1992.

A. M. Lyapunov. The general problem of the stability of motion. *International Journal of Control, London (English translation from the French: Liapounoff A (1907) Probléme général de la stabilité du mouvement. Annal. Fac. Sci. Toulouse 9, 203-474. The French text was reprinted in Annals Math. Studies Vol. 17 Princeton Univ. Press (1947). The original was published in Russian by the Mathematical Society of Kharkov in 1892.)*, 55(3):531–534, 1992.

D. MacKay. *Sustainable Energy-without the hot air*. UIT Cambridge, 2008.

S. Matsuda and M. Yoshikawa. Magnetic island formation due to error field in the jft-2 tokamak. *Japanese Journal of Applied Physics*, 14(1):87, 1975.

J. Misguich, J. Reuss, D. Constantinescu, G. Steinbrecher, M. Vlad, F. Spineanu, B. Weyssow, and R. Balescu. Noble cantor sets acting as partial internal transport barriers in fusion plasmas. *Plasma physics and controlled fusion*, 44(7):L29, 2002.

J. H. Misguich. Dynamics of chaotic magnetic lines: Intermittency and noble internal transport barriers in the tokamap. *Physics of Plasmas*, 8(5):2132–2138, 2001.

A. Morozov and L. Solov'Ev. Motion of charged particles in electromagnetic fields. *Reviews of Plasma Physics*, 2:201, 1966.

J. Ongena and G. V. Oost. Energy for future centuries: prospects for fusion power as a future energy source. *Fusion Science and Technology*, 61(2T):3–16, 2012.

H. Poincaré. Les méthodes nouvelles de la mécanique céleste vol 1 (paris: Gauthier-villars). 1892.

A. Punjabi, A. Verma, and A. Boozer. Tokamak divertor maps. *Journal of plasma physics*, 52(1): 91–111, 1994.

C. Skokos. Alignment indices: a new, simple method for determining the ordered or chaotic nature of orbits. *Journal of Physics A: Mathematical and General*, 34(47):10029, 2001.

C. Skokos. The Lyapunov characteristic exponents and their computation. In *Dynamics of Small Solar System Bodies and Exoplanets, Lect. Notes in Physics 790*, pages 63–135. Springer, 2010.

C. Skokos and T. Manos. The smaller (sali) and the generalized (gali) alignment indices: Efficient methods of chaos detection. In *Chaos Detection and Predictability, L.N.P. 915*, pages 129–181. Springer, 2016.

C. Skokos, C. Antonopoulos, T. Bountis, and M. Vrahatis. Detecting order and chaos in hamiltonian systems by the sali method. *Journal of Physics A: Mathematical and General*, 37(24):6269, 2004.

C. Skokos, T. Bountis, and C. Antonopoulos. Geometrical properties of local dynamics in hamiltonian systems: The generalized alignment index (gali) method. *Physica D: Nonlinear Phenomena*, 231(1): 30–54, 2007.

C. Skokos, T. Bountis, and C. Antonopoulos. Detecting chaos, determining the dimensions of tori and predicting slow diffusion in fermi–pasta–ulam lattices by the generalized alignment index method. *The European Physical Journal Special Topics*, 165(1):5–14, 2008.

The Economist. Tokamak and stellarator. http://www.economist.com/science-and-technology/2015/10/24/stellar-work, Accessed October 2018.

J. Wesson. Tokamaks, volume 118 of. *International Series of Monographs on Physics*, 2004.

R. B. White. *The theory of toroidally confined plasmas*. World Scientific Publishing Company, 2013.

Wikipedia. Poincaré map. Wikipedia, the Free Encyclopedia, http://en.wikipedia.org/wiki/Poincaré_map#/media/File:Poincare_map.svg, Accessed June 2018.

A. Wingen, K. Spatschek, and S. Abdullaev. Stochastic transport of magnetic field lines in the symmetric tokamap. *Contributions to plasma physics*, 45(7):500–513, 2005.